Investigation of the Fundamentals of Electrospray Ionization and the Separation of Small Molecules using Ion Mobility Mass Spectrometry

Kimberly L. Davidson

A dissertation
submitted in partial fulfillment of the
requirements for the degree of

Doctor of Philosophy

University of Washington
2017

Reading Committee:
Matthew F. Bush, Chair
Robert E. Synovec
Joshua C. Vaughan

Program Authorized to Offer Degree:
Chemistry

University of Washington

Abstract

Investigation of the Fundamentals of Electrospray Ionization and the Separation of Small Molecules using Ion Mobility Mass Spectrometry

Kimberly L. Davidson

Chair of Supervisory Committee:
Assistant Professor Matthew F. Bush
Department of Chemistry

Ion mobility mass spectrometry (IM-MS) is a gas-phase technique used to separate ions based on their mass-to-charge ratio and collision cross section (*i.e.* shape). Accurate MS analysis of analytes, such as proteins and protein complexes, relies on the preservation of solution-phase oligomeric distributions during ionization. Gas-phase ions in IM-MS are typically formed using electrospray ionization (ESI), which is a gentle ionization source that preserves noncovalent interactions. One challenge in ESI is that multiple analytes in a single droplet can aggregate during solvent evaporation, biasing the oligomeric states of proteins or protein complexes observed during gas-phase measurements. Initial droplet diameters using electrokinetic nano-ESI were measured and reported to be ~60 nm at an ionization current of 30 nA, which is a typical

current for native IM-MS experiments. Nonspecific aggregation of a monomeric protein, myoglobin, was measured as a function of concentration of the protein in solution as well as ionization current (*i.e.*, initial droplet size). Results from those measurements show that nonspecific aggregation increases with ionization current, initial droplet size, and concentration of the analyte in solution. The ionization mechanism of macromolecules from solution to the gas phase was also analyzed by measuring the average charge states of proteins, ranging in mass from 8 – 468 kDa, in four different buffers (ammonium acetate, methylammonium acetate, dimethylammonium acetate, and trimethylammonium acetate). Those results were analyzed according to both the charged residue model and the more recent charged residue-field emission model. In IM, ions are separated using a drift cell that is filled with a neutral gas (typically He or N_2) and has an applied electric field. The collision cross sections of 20 common amino acids were measured using a radio-frequency confining drift cell and five different drift gases (He, Ar, N_2, CO_2 and N_2O), which were chosen based on their range of masses and polarizabilities. Drift gas selectivity was quantified using peak capacity and peak-to-peak resolution. Those results show that the identities of the pairs of amino acids separated depends on the drift gas and the number of pairs separated depends on peak capacity. The collision cross sections of ten petroleum-like compounds (containing aromatic isomers and double-bond equivalents) were also measured in He, Ar, N_2 and CO_2. Those results demonstrate the potential to improve separations of compounds with the same elemental composition by using gases with greater mass and polarizability.

Dedication

To my parents, my sister, and Kevin.

Acknowledgements

Graduate school has been a challenging, at times frustrating, but also amazing, and wonderful experience. I've grown so much as a person and a scientist over the past five years and I have many people to thank for that. First, I would like to thank my advisor, Prof. Matthew F. Bush, for being an amazing mentor these past five years. I knew next to nothing about ion mobility mass spectrometry when I started my graduate career but Matt gave me the opportunity to pursue my research interests and thrive. I would also like to thank my committee members, including Prof. Robert Synovec, Frantisek Turecek, Joshua Vaughan, Daniel Raftery, Daniel Chiu, Charles Campbell, and Joel Thornton.

My first project and paper would not have been possible without the help of Derek Oberreit and Chris Hogan at the University of Minnesota. I would like to thank them for their expertise, help and hospitality during my stay in Minnesota.

I would also like to thank the wonderful people who have answered my many questions during my time at UW, including Elizabeth Lee (Fiscal Specialist), Ashley Zigler (previous Graduate Program Coordinator), Diana Knight (Assistant to the Chair), and Krista Holden (Graduate Program Coordinator).

Finally, I would like to thank my past and current lab mates. Samuel Marionni helped me immensely when I was learning how to code and without him, many of my analyses would have taken far longer to complete. Samuel Allen taught me everything I know about the radio-frequency confining drift cell that I used for most of my experiments. He was also extremely patient with me when I bombarded him with troubleshooting questions. Ken Laszlo has been a great sounding board for thoughts and ideas regarding new projects and life in general. And last

but not least, I am going to sorely miss coffee breaks and discussions with Rae Eaton, Meagan Gadzuk-Shea, and Cece Hong.

I have had many mentors but my first mentors were my parents. They worked hard, persevered, and never gave up. They are my inspiration for pursuing higher education and without them, I would never have achieved my goals.

Nomenclature

Ar	argon, in reference to IMS buffer gas
CRM	Charged-Residue Model
CO_2	carbon dioxide, in reference to IMS buffer gas
Da	Dalton, the unified atomic mass unit
DC	Direct Current
e	elementary charge, $1.6021766208(98) \times 10^{-19}$ C
E	Electric Field
Electrokinetic	the flow of electricity
$E \cdot P^{-1}$	drift field strength: electric field divided by pressure, $V \cdot cm^{-1} \cdot Torr^{-1}$
ESI	Electrospray Ionization
He	helium, in reference to IM buffer gas
IM	Ion Mobility
k_B	Boltzmann's constant, $1.38064852(79) \times 10^{-23}$ J·K^{-1}
μ	reduced mass, often between ion and neutral masses
MS	Mass Spectrometry
m/z	mass-to-charge ratio, the standard measurement unit in MS
N_2	nitrogen, in reference to IMS buffer gas
Ω	ion-neutral collision cross section
P_c	peak capacity
RF	Radio-Frequency, referring to the frequency of AC potentials
R_p	resolving power
$R_{p\text{-}p}$	peak-to-peak resolution
t_D	drift time
TOF	time-of-flight, an MS analyzer
z	ion charge state

Table of Contents

Chapter 1

Introduction

1.1 Native Mass Spectrometry (MS)

Mass spectrometry (MS) is a gas-phase technique that separates ions based on their mass to-charge ratio (*m*/*z*). Most mass spectrometers include an ion source, a mass analyser and a detector. Protein mass spectrometry typically involves dissolving an analyte in an acidic solution to promote denaturation. The denatured protein has a greater surface area compared to its native, folded form and is therefore highly charged and detected at low *m*/*z*, allowing for peptide identification and sequencing.[1,2] More recently, native MS has become an important tool in investigations of protein and protein complex stoichiometry and dynamics due to its speed and sensitivity.[3–6] In native MS studies, it is important to maintain protein and protein complex structures and any noncovalent interactions. Solution conditions, therefore, are nondenaturing and held at a biologically relevant pH (*e.g.*, aqueous ammonium acetate at pH = 7.0). Additionally, soft-ionization techniques such as electrospray ionization (ESI)[3,7] or nanoESI[8–10] are ideal for the transfer of proteins from solution phase to the gas phase because they generally retain native conformations of proteins and protein complexes.

1.2 Electrospray Ionization (ESI) and Nanoelectrospray Ionization (nanoESI)

ESI and nanoESI are both soft-ionization techniques used in analyses of biological molecules such as proteins and protein complexes.[5,6,11,12] In ESI, solution is delivered into a metallic capillary held at a high voltage. The solution then flows through the capillary and forms a Taylor cone[13,14] at the tip of the capillary; the Taylor cone eventually produces small, multiply charged droplets.[15] The capillary is typically surrounded by a tube that delivers an inert gas

enabling more efficient desolvation of the droplets. A portion of these droplets will contain the analyte of interest, which will enter the instrument as a multiply charged species.[16] If the charge on a droplet is sufficiently great, the electrostatic force will be strong enough to disrupt the surface tension holding the droplet together.[15] This Coulomb repulsion results in progeny droplets that have 2% of the mass and 15% of the charge of the parent droplet.[15–17] This process continues with further desolvation of the droplet until gas-phase ions are produced.

A disadvantage of ESI is the occurrence of nonspecific aggregation of analytes and salt adduction. For example, if a droplet is large enough, it can contain more than one copy of a protein. During the desolvation and fission events, protein copies within a droplet can cluster together to form a nonspecific aggregate that does not reflect the oligomeric distribution present in solution.[18,19] Excess salt adduction can also occur if a droplet is large enough to contain contaminants from solution (Na^+, K^+ etc.) that will then be inherited by the protein during desolvation.[18]

NanoESI follows the same process as ESI but the capillaries have much smaller tip diameters (1-10 μm) and applied voltages (~0.5 – 1.5 kV).[13] As a result, the flow rates are lower than those from ESI and the initial droplets produced by nanoESI are much smaller (~60 nm in diameter),[9] which reduces the adduction of small molecules and ions[10] and nonspecific aggregation of analytes.[10,18] Additionally, smaller initial droplets reduce the number of fission events that occur and the concentration of contaminants, therefore the analytes are present in relatively greater amounts.[13,14] NanoESI can be implemented by applying a voltage to either gold-coated capillaries or to a platinum wire that is inserted into the solution within the capillary.

1.3 Charged-Residue Model (CRM) and Ion Evaporation Model (IEM)

The most widely accepted model used to explain the formation of multiply charged macromolecular ions during the ionization process is the charged-residue model (CRM).[16,20,21] In this model, neutral solvent molecules evaporate from the initial charged droplet until the Coulombic repulsion exceeds the surface tension of the droplet (the Rayleigh limit):[22]

$$z \cdot e = \pi(8\varepsilon_0\gamma)^{1/2}D^{3/2} \quad (1.1)$$

where z is the number of charges, e is the elementary charge, ε_0 is the permittivity of free space, γ is the surface tension (72 mN/m for water at 25 °C), and D is the droplet diameter. At this limit, Coulomb fission will result in the ejection of a progeny droplet with a smaller radius and a fraction of the charges of the precursor droplet.[15] This process repeats until complete desolvation results in the formation of a multiply charged, gas-phase analyte ion.

While the CRM is a useful model for approximating charge states of macromolecules, there are significant differences between experimental results and predictions determined using Equation 1.1. The average charge states of native-like protein cations with masses ranging from 6 – 468 kDa are typically less than those estimated using the Rayleigh limit and a surface tension of water.[23,24] Additionally, the terms in the Rayleigh limit are independent of polarity but the charge states of macromolecules are dependent on polarity (positive or negative ion mode) where negative charge states are less than those of positive charge states.[4,16,24]

The Ion Evaporation Model (IEM), which mostly applies to small molecules, states that an ion will be emitted from a droplet when the repulsion between the ion and other charges in the droplet overcome solvation forces.[25] The ion will then be emitted from the droplet into the gas phase.

1.4 Combined Charged Residue Field Emission Model (CCRFEM)

Given the discrepancies between the average charge states of native-like ions measured experimentally and those predicted using the Rayleigh limit, Hogan *et al*. proposed the Combined Charged Residue Field Emission Model (CCRFEM).[23,26] The CCRFEM states that both Coulomb fission (similar to the CRM) and small charge carrier emission from electrosprayed droplets (analogous to the ion evaporation model (IEM)),[17,21] influences the charge states of macromolecules. Small charge carrier emission occurs when the surface of an electrosprayed droplet reaches a critical field strength, E*. Once a charge carrier is emitted, the electric field strength decreases, preventing further charge-carrier emission. After neutral-solvent evaporation, the surface of the droplet will reach yet another E* at which another charge carrier will be emitted. The emission of small ions is dependent on E* and the solvation energies of the charge carriers. The charges on a macromolecule for a given E* is given by:[23,26]

$$z = \frac{\pi \varepsilon_0 E^*}{e} D^2 \tag{1.2}$$

where *D* is the macromolecule diameter (typically determined using a protein density of 1.0 g cm^{-3}). Therefore, the charge state of a macromolecule can be predicted if E* and *D* are known.

1.5 Ion Mobility (IM)

Ion mobility (IM) is a useful technique for separating ions in the gas phase according to their shape and charge. In IM, ions are separated based on their mobility (K) through a weak electric field (E):

$$K = \frac{L}{t_D E} = \frac{L^2}{t_D V} \tag{1.3}$$

where L is the length of the drift cell, t_D is the observed drift time, and V is the voltage change across the drift cell. The collision cross section (Ω) of the ion is determined using K and the Mason-Schamp equation:[27]

$$\Omega = \frac{3ez}{16N}\sqrt{\frac{2\pi}{\mu k_B T}}\frac{1}{K} \tag{1.4}$$

where e is the elementary charge, z is the charge state of the ion, N is the number density of the drift gas, μ is the reduced mass of the ion and neutral, k_B is Boltzmann's constant, and T is the drift-gas temperature. Ω, to a first approximation, are orientationally averaged projection areas of ion-neutral pairs and provide information about the relative sizes of ions.[27,28]

1.5.1 Peak-to-Peak Resolution ($R_{p\text{-}p}$)

In IM, an arrival time distribution (ATD) of an ion is measured and its t_D is taken as the centroid of a Gaussian fit to the peak. In order to quantify the separation of two ATDs in IM, a peak-to-peak resolution ($R_{p\text{-}p}$) is calculated and is defined as:

$$R_{p-p} = \frac{t_{D2} - t_{D1}}{0.5(w_2 + w_1)} \tag{1.5}$$

where w is the width at base of each peak. For a single conformer, w can be estimated using:

$$w^2 = {w_g}^2 + {w_d}^2 = {w_g}^2 + \frac{32k_BT}{Vez}\left(\frac{L^2}{KV}\right)^2 \tag{1.6}$$

where w_g is the width attributable to the ion release time, or gating, from the trap cell (Figure 1.1) and w_d is the width attributable to diffusion of the ions.[29,30] One strategy to increase $R_{p\text{-}p}$ is to decrease w by decreasing w_g, which may also decrease sensitivity.[30,31] Additionally, V can be increased but this typically requires increasing L in order to decrease the relative contributions from gating and mitigate electrical breakdown.[32,33] Finally, T can be decreased in order to minimize contributions from molecular diffusion.[34,35]

1.5.2 Peak Capacity (P_c)

Peak capacity, P_c, is a quantitative measure of the information content available from a separation. P_c is proportional to the difference between maximum and minimum drift times and inversely proportional to the average peak width:[36,37]

$$P_c = \frac{t_{max} - t_{min}}{0.5(w_{max} + w_{min})} \quad (1.7)$$

where t_{max} and t_{min} are the drift times of the least and most mobile ions and w_{max} and w_{min} are the width at base of those peaks, respectively.

1.6 Ion Mobility Mass Spectrometry (IM-MS)

Ion mobility combined with mass spectrometry (IM-MS) provides a two-dimensional analysis of a broad array of compounds and molecules including proteins, phospholipids,[38] peptides,[36,39,40] metabolites[41] and petroleum molecules.[42–44] The advantage of IM-MS is its ability to measure not only a compound's mass but also to determine if there are multiple different compounds with the same mass. Many efforts have been made to improve IM separations over the years, including increasing the path length (L, Equation 1.3),[45,46] changing drift tube temperature,[34] and using different drift gases in the drift cell.[40,44,47]

1.6.1 Instrumentation

The Waters Corporation released the first commercially available instrument capable of performing ion mobility experiments in 2005, the Synapt HDMS.[48] This instrument contained a traveling-wave ion mobility (TWIM) cell combined with time-of-flight (TOF) mass analysis, which is a common analyzer for native MS.[49–51] Traveling-wave IM uses DC potentials to generate time-dependent "waves" across a series of stacked-ring electrodes and RF potentials to radially confine ions, which improves ion transmission.[52–54] While TWIMS has been extremely

valuable for characterizing proteins,[55] protein complexes,[56,57] and other analytes,[38,58] measured drift times require calibration using calibrants with known Ω due to the non-uniform DC electric field.[59,60]

In order to directly measure drift times, and therefore absolute Ω, Bush *et al.* developed an rf-confining drift cell, which was first implemented on a Waters Synapt G1 HDMS.[60] This drift cell consists of a series of stacked-ring electrodes that have a uniform DC gradient and alternating RF potentials to radially confine ions. The instrument used in the majority of the studies presented here is a Waters Synapt G2 HDMS that has an rf-confining drift cell in place of the commercial TWIMS cell (Figure 1.1).[61]

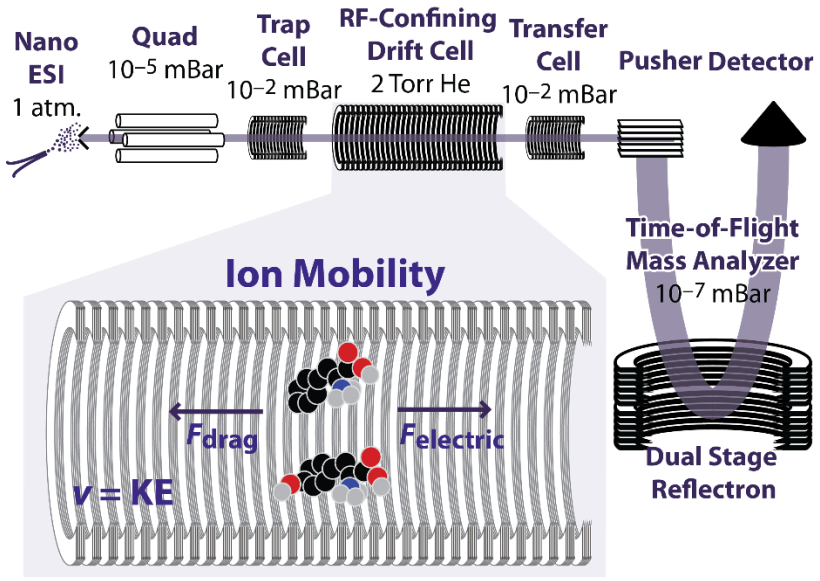

Figure 1.1. A Waters Synapt G2 HDMS modified with an rf-confining drift cell in place of the original travelling-wave ion mobility cell. Ions are produced using nanoESI and enter the instrument where they can be mass filtered prior to the trap cell using a quadrupole. The rf-confining drift cell can be used to separate ions according to their drift time through a weak electric field and/or the ions can pass through for mass analysis using the Time-of-Flight mass analyzer.

1.7 Outline of the Present Study

This thesis presents the investigation of two specific areas: 1) electrospray ionization fundamentals and mechanisms and 2) the analysis of separation of small molecules using different drift gases in an rf-confining drift cell. In IM-MS, analytes are first transferred into the gas phase using an ionization technique, which should be gentle enough to preserve noncovalent interactions. The mechanism by which these analytes are ionized has been studied extensively[15,21,22,24,26,62,63] but there are still limitations of our understanding of the ionization process. Once ionized, analytes are separated in a drift cell filled with a background gas based on their mobility in an electric field (Equation 1.3). The background gas is typically He, N_2 or air but other gases can be used to change or improve separations between ions.[44,47]

Chapter 2 discusses the ability of electrokinetic nanoESI to preserve solution-phase oligomeric states as analytes are transferred into the gas phase. This study reports on the measurements of initial droplet sizes from an electrokinetic nanoESI source as a function of electrospray current. Additionally, Poisson statistics are used to determine the extent of nonspecific aggregation over a range of electrospray currents using the same source. This study shows that at low currents and flow rates, electrokinetic nanoESI preserves ~98% of oligomeric distributions of myoglobin, which is a monomer in solution. Additionally, when ionization currents are low (30 nA), oligomeric distributions are better preserved when protein concentration is low (<40 μM).

Chapter 3 investigates the effects of different buffers on native protein charge states in positive and negative ion mode. Proteins ranging in mass from 8-468 kDa are dissolved in four different buffers that vary only in their cation, where each cation has a different solvation energy. The average charge states of the proteins are measured and analyzed using previous methods.[24,26]

The average charge states of the proteins generally decrease with decreasing solvation energy of the cation present in solution. However, the changes in average charge state are not discrete and therefore, do not appear to be correlated with the change in buffer cation. Attempts are made to identify the cations in solution that most influence protein charge state using computational methods.

Chapters 4 and 5 discuss the separation of small molecules using different drift gases in an rf-confining drift cell. Chapter 4 reports the Ω of protonated amino acids in five drift gases (He, Ar, N_2, CO_2 and N_2O) and also characterizes the selectivity of each drift gas using $R_{p\text{-}p}$ and P_c. This study demonstrates that the separation of small molecules can be improved by using larger, more-polarizable drift gases such as Ar, N_2 and CO_2. Chapter 5 reports the Ω of quinoline, isoquinoline and their double-bond equivalents (DBE) with four different drift gases (He, Ar, N_2 and CO_2). While many petroleomics studies have shown separation of DBE with different masses, the separation of DBE with the same mass has not been thoroughly explored or quantified. This chapter reports $R_{p\text{-}p}$ and P_c of DBE in each gas and analyzes the interactions between an ion and each gas using computational methods.

1.8 Collaborative Work

In addition to the work presented here, I have also had the opportunity to collaborate with Dr. Libin Xu's group at the University of Washington, Dr. Hugh Kim's group from Korea University, and Dr. Sunghwan Kim's group from Kyungpook National University. The work I did with Dr. Xu's group involved measuring absolute Ω values, using our rf-confining drift cell (Figure 1.1), of different chain lengths of polyalanine and a few antibiotics for calibration of TWIMS measurements of drugs and drug-like molecules. For Dr. Hugh Kim's group, I taught a

visiting student, Jong Wha, how to measure absolute Ω for a set of aromatic compounds for comparison with theoretical calculations. Finally, I measured Ω of a set of polyaromatic hydrocarbons (PAH) for Dr. Sunghwan Kim's group using an atmospheric solids analysis probe (to generate radical cations) and the rf-confining drift cell shown in Figure 1.1. Papers for these three studies have been submitted recently and are under review.

1.9 References

(1) Aebersold, R.; Mann, M. *Nature* **2003**, *422* (6928), 198–207.
(2) Mann, M.; Jensen, O. N. *Nat Biotech* **2003**, *21* (3), 255–261.
(3) Fenn, J. B.; Mann, M.; Meng, C. K.; Wong, S. F.; Whitehouse, C. M. *Science* **1989**, *246* (4926), 64–71.
(4) Heck, A. J. R.; van den Heuvel, R. H. H. *Mass Spectrom. Rev.* **2004**, *23* (5), 368–389.
(5) Uetrecht, C.; Barbu, I. M.; Shoemaker, G. K.; van Duijn, E.; Heck, A. J. R. *Nat Chem* **2011**, *3* (2), 126–132.
(6) Bleiholder, C.; Dupuis, N. F.; Wyttenbach, T.; Bowers, M. T. *Nat. Chem.* **2011**, *3* (2), 172–177.
(7) Tang, X.; Bruce, J. E.; Hill, H. H. *Anal. Chem.* **2006**, *78* (22), 7751–7760.
(8) Schmidt, A.; Karas, M.; Dülcks, T. *J. Am. Soc. Mass Spectrom.* **2003**, *14* (5), 492–500.
(9) Davidson, K. L.; Oberreit, D. R.; Hogan, C. J.; Bush, M. F. *Int. J. Mass Spectrom.* DOI: 10.1016/j.ijms.2016.09.013.
(10) Wilm, M.; Mann, M. *Anal. Chem.* **1996**, *68* (1), 1–8.
(11) Hilton, G. R.; Benesch, J. L. P. *J. Roy. Soc. Interface* **2012**, *9* (70), 801–816.
(12) Kitova, E.; El-Hawiet, A.; Schnier, P.; Klassen, J. *J. Am. Soc. Mass Spectrom.* **2012**, *23* (3), 431–441.
(13) Wilm, M. S.; Mann, M. *International Journal of Mass Spectrometry and Ion Processes* **1994**, *136* (2–3), 167–180.
(14) Fernandez de la Mora, J.; Loscertales, I. G. *Journal of Fluid Mechanics* **1994**, *260*, 155–184.
(15) Gomez, A.; Tang, K. *Phys. Fluids* **1994**, *6* (1), 404–414.
(16) Fernandez de la Mora, J. *Analytica Chimica Acta* **2000**, *406* (1), 93–104.
(17) Kebarle, P.; Peschke, M. *Analytica Chimica Acta* **2000**, *406* (1), 11–35.
(18) Benesch, J. L. P.; Ruotolo, B. T.; Simmons, D. A.; Robinson, C. V. *Chem. Rev.* **2007**, *107* (8), 3544–3567.
(19) Sun, J.; Kitova, E. N.; Sun, N.; Klassen, J. S. *Anal. Chem.* **2007**, *79* (21), 8301–8311.
(20) Dole, M.; Mack, L. L.; Hines, R. L.; Mobley, R. C.; Ferguson, L. D.; Alice, M. B. *J. Chem. Phys.* **1968**, *49* (5), 2240–2249.
(21) Konermann, L.; Ahadi, E.; Rodriguez, A. D.; Vahidi, S. *Anal. Chem.* **2013**, *85* (1), 2–9.
(22) Rayleigh, L. *Philosophical Magazine* **1882**, *14*, 184–186.
(23) Hogan, C. J.; Carroll, J. A.; Rohrs, H. W.; Biswas, P.; Gross, M. L. *J. Am. Chem. Soc.* **2008**, *130* (22), 6926–6927.
(24) Allen, S. J.; Schwartz, A. M.; Bush, M. F. *Anal. Chem.* **2013**, *85* (24), 12055–12061.
(25) Iribarne, J. V.; Thomson, B. A. *The Journal of Chemical Physics* **1976**, *64* (6), 2287–2294.
(26) Hogan, C. J.; Carroll, J. A.; Rohrs, H. W.; Biswas, P.; Gross, M. L. *Anal. Chem.* **2009**, *81* (1), 369–377.
(27) Mason, E. A.; McDaniel, E. W. *Transport Properties of Ions in Gases*; Wiley: New York, 1988.
(28) Wyttenbach, T.; Bleiholder, C.; Bowers, M. T. *Anal. Chem.* **2013**, *85* (4), 2191–2199.
(29) Revercomb, H. E.; Mason, E. A. *Anal. Chem.* **1975**, *47* (7), 970–983.
(30) Kanu, A. B.; Gribb, M. M.; Hill, H. H. *Anal. Chem.* **2008**, *80* (17), 6610–6619.

(31) Ibrahim, Y. M.; Garimella, S. V. B.; Tolmachev, A. V.; Baker, E. S.; Smith, R. D. *Anal. Chem.* **2014**, *86* (11), 5295–5299.
(32) Baker, E. S.; Clowers, B. H.; Li, F.; Tang, K.; Tolmachev, A. V.; Prior, D. C.; Belov, M. E.; Smith, R. D. *J. Am. Soc. Mass Spectrom.* **2007**, *18* (7), 1176–1187.
(33) Ibrahim, Y. M.; Baker, E. S.; Danielson, W. F.; Norheim, R. V.; Prior, D. C.; Anderson, G. A.; Belov, M. E.; Smith, R. D. *Int J Mass Spectrom* **2015**, *377*, 655–662.
(34) May, J. C.; Russell, D. H. *J. Am. Soc. Mass Spectrom.* **2011**, *22* (7), 1134–1145.
(35) Ujma, J.; Giles, K.; Morris, M.; Barran, P. E. *Anal. Chem.* **2016**, *88* (19), 9469–9478.
(36) Ruotolo, B. T.; Gillig, K. J.; Stone, E. G.; Russell, D. H. *J. Chromatogr. B Analyt. Technol. Biomed. Life Sci.* **2002**, *782* (1–2), 385–392.
(37) Ruotolo, B. T.; McLean, J. A.; Gillig, K. J.; Russell, D. H. *J Mass Spectrom* **2004**, *39* (4), 361–367.
(38) Ridenour, W. B.; Kliman, M.; McLean, J. A.; Caprioli, R. M. *Anal. Chem.* **2010**, *82* (5), 1881–1889.
(39) Bush, M. F.; Campuzano, I. D. G.; Robinson, C. V. *Anal. Chem.* **2012**, *84* (16), 7124–7130.
(40) Beegle, L. W.; Kanik, I.; Matz, L.; Hill, H. H., Jr. *International Journal of Mass Spectrometry* **2002**, *216*, 257–268.
(41) Paglia, G.; Williams, J. P.; Menikarachchi, L.; Thompson, J. W.; Tyldesley-Worster, R.; Halldórsson, S.; Rolfsson, O.; Moseley, A.; Grant, D.; Langridge, J.; Palsson, B. O.; Astarita, G. *Anal. Chem.* **2014**, *86* (8), 3985–3993.
(42) Fernandez-Lima, F. A.; Becker, C.; McKenna, A. M.; Rodgers, R. P.; Marshall, A. G.; Russell, D. H. *Anal. Chem.* **2009**, *81* (24), 9941–9947.
(43) Ponthus, J.; Riches, E. *Int. J. Ion Mobil. Spec.* **2013**, *16* (2), 95–103.
(44) Fasciotti, M.; Lalli, P. M.; Klitzke, C. F.; Corilo, Y. E.; Pudenzi, M. A.; Pereira, R. C. L.; Bastos, W.; Daroda, R. J.; Eberlin, M. N. *Energy Fuels* **2013**, *27* (12), 7277–7286.
(45) Deng, L.; Ibrahim, Y. M.; Hamid, A. M.; Garimella, S. V. B.; Webb, I. K.; Zheng, X.; Prost, S. A.; Sandoval, J. A.; Norheim, R. V.; Anderson, G. A.; Tolmachev, A. V.; Baker, E. S.; Smith, R. D. *Anal. Chem.* **2016**, *88* (18), 8957–8964.
(46) Merenbloom, S. I.; Koeniger, S. L.; Valentine, S. J.; Plasencia, M. D.; Clemmer, D. E. *Anal. Chem.* **2006**, *78* (8), 2802–2809.
(47) Asbury, G. R.; Hill, H. H. *Anal. Chem.* **2000**, *72* (3), 580–584.
(48) Pringle, S. D.; Giles, K.; Wildgoose, J. L.; Williams, J. P.; Slade, S. E.; Thalassinos, K.; Bateman, R. H.; Bowers, M. T.; Scrivens, J. H. *International Journal of Mass Spectrometry* **2007**, *261*, 1–12.
(49) Guilhaus, M.; Selby, D.; Mlynski, V. *Mass Spectrom. Rev.* **2000**, *19* (2), 65–107.
(50) van den Heuvel, R. H. H.; van Duijn, E.; Mazon, H.; Synowsky, S. A.; Lorenzen, K.; Versluis, C.; Brouns, S. J. J.; Langridge, D.; van der Oost, J.; Hoyes, J.; Heck, A. J. R. *Anal. Chem.* **2006**, *78* (21), 7473–7483.
(51) Kozlovski, V. I.; Donald, L. J.; Collado, V. M.; Spicer, V.; Loboda, A. V.; Chernushevich, I. V.; Ens, W.; Standing, K. G. *International Journal of Mass Spectrometry* **2011**, *308* (1), 118–125.
(52) Giles, K.; Pringle, S. D.; Worthington, K. R.; Little, D.; Wildgoose, J. L.; Bateman, R. H. *Rapid Commun. Mass Spectrom.* **2004**, *18* (20), 2401–2414.
(53) Giles, K.; Williams, J. P.; Campuzano, I. *Rapid Commun. Mass Spectrom.* **2011**, *25* (11), 1559–1566.

(54) Zhong, Y.; Hyung, S.-J.; Ruotolo, B. T. *The Analyst* **2011**, *136* (17), 3534.
(55) Scarff, C. A.; Thalassinos, K.; Hilton, G. R.; Scrivens, J. H. *Rapid Communications in Mass Spectrometry* **2008**, *22* (20), 3297–3304.
(56) Zhou, M.; Morgner, N.; Barrera, N. P.; Politis, A.; Isaacson, S. C.; Matak-Vinkovic, D.; Murata, T.; Bernal, R. A.; Stock, D.; Robinson, C. V. *Science* **2011**, *334* (6054), 380–385.
(57) Han, L.; Ruotolo, B. T. *Int. J. Ion Mobil. Spec.* **2013**, *16* (1), 41–50.
(58) Thalassinos, K.; Grabenauer, M.; Slade, S. E.; Hilton, G. R.; Bowers, M. T.; Scrivens, J. H. *Anal. Chem.* **2009**, *81* (1), 248–254.
(59) Ruotolo, B. T.; Benesch, J. L. P.; Sandercock, A. M.; Hyung, S.-J.; Robinson, C. V. *Nat. Protoc.* **2008**, *3* (7), 1139–1152.
(60) Bush, M. F.; Hall, Z.; Giles, K.; Hoyes, J.; Robinson, C. V.; Ruotolo, B. T. *Anal. Chem.* **2010**, *82* (22), 9557–9565.
(61) Allen, S. J.; Bush, M. F. *J. Am. Soc. Mass Spectrom.* **2016**, *27*, 2054–2063.
(62) Verkerk, U. H.; Kebarle, P. *J. Am. Soc. Mass Spectrom.* **2005**, *16* (8), 1325–1341.
(63) Iavarone, A. T.; Jurchen, J. C.; Williams, E. R. *J. Am. Soc. Mass Spectrom.* **2000**, *11* (11), 976–985.

Chapter 2

Nonspecific Aggregation in Native Electrokinetic Nanoelectrospray Ionization

This chapter is reproduced with permission from Davidson, Kimberly L.; Oberreit, Derek R.; Hogan Jr., Christopher J.; Bush, Matthew F. "Nonspecific Aggregation in Native Electrokinetic Nanoelectrospray Ionization" *International Journal of Mass Spectrometry* **2016**. DOI: 10.1016/j.ijms.2016.09.013.

2.1 Abstract

Native mass spectrometry is widely used to determine the stoichiometries and binding constants of noncovalent interactions in solution. One challenge is that multiple analytes in a single electrospray droplet can aggregate during solvent evaporation, which will bias the distribution of oligomeric states observed during gas-phase measurements. Here, measurements of solution flow rates, electrospray currents, droplet size distributions, and nonspecific aggregation are used in conjunction with Poisson statistics to characterize the factors that control nonspecific aggregation during typical native mass spectrometry experiments. Using electrokinetic nanoelectrospray ionization and a 30 nA current, low flow rates of less than 10 nL min^{-1} and initial droplets with mean diameters of ~60 nm were observed. For solutions containing 4 μM analyte under these conditions, Poisson statistics and charge-reduction drift tube ion mobility spectrometry both indicate that ~90% of the desolvated, occupied droplets contain a single analyte. Initial droplet sizes and contributions from nonspecific aggregates both increase with increasing current. Ion mobility mass spectrometry analysis of the ions produced using these conditions without charge reduction exhibit even less nonspecific aggregation (~2%).

All approaches indicate that increasing the ionization current increases the flow rate, droplet size distribution, and extent of nonspecific aggregation. These results provide detailed insights into the role of small initial droplets in the success of native mass spectrometry.

2.2 Introduction

In native mass spectrometry, intact protein and protein complex ions are formed using electrospray ionization (ESI) from aqueous buffered solutions that have a biologically relevant pH and ionic strength. Native mass spectrometry is now widely used to characterize the stoichiometry[1-7] and binding constants[8-10] of proteins, ligands, and metal ions in noncovalent complexes. For example, native mass spectrometry has been used to characterize intermediates in the assembly of disease-associated protein aggregates[1,3,7] and viral capsids.[2,6,11] Most studies implicitly or explicitly assume that the oligomeric distribution of the ions analyzed in these experiments resemble those of the corresponding noncovalent complexes in solution. However, if multiple analytes in a single droplet aggregate during the evaporation of the solvent, the distribution of oligomeric states observed in the gas-phase measurements will be biased by the presence of nonspecific aggregates.[12-14]

The charged-residue model is most-often used to explain the formation of multiply charged macromolecular ions. In this model, neutral solvent molecules evaporate from the initial charged droplet until the Coulombic repulsion exceeds the surface tension of the droplet (the Rayleigh limit).[15-17] At this limit, Coulomb fission will result in the ejection of a progeny droplet with a smaller radius and a fraction of the charges of the precursor droplet.[15] This process repeats until complete desolvation results in the formation of a multiply charged, gas-phase analyte ion. During solvent evaporation, the concentration of solutes will increase, which may result in the

formation of nonspecific aggregates when multiple solutes are present in a single droplet. The extent of nonspecific aggregates is therefore linked to both the original droplet size distribution and the size distributions of progeny droplets formed during fission events.

Most fundamental studies of the ESI have used externally controlled solution flows through capillaries with inner diameters of tens to hundreds of micrometers,[11,18-20] which will be referred to as constant-flow ESI. In contrast, most native mass spectrometry experiments use comparatively smaller inner diameter capillaries without an externally applied pressure. The flow rates in these experiments depend on the electroosmotic flow[21] of the solution that is induced by the applied electric field, which we refer to here as electrokinetic nanoESI. This implementation exhibits many advantages including reduced sample consumption,[22] adduction of small molecules and ions,[22,23] and nonspecific aggregation of analytes.[23] For example, electrokinetic nanoESI of the *E Coli.* chaperone GroEL yields well-resolved mass spectral peaks corresponding to different charge states of the biologically relevant tetradecamer.[23] Constant-flow ESI of the same sample using the same mass analyzer yields significantly broader peaks and relatively intense features corresponding to nonspecific dimers and trimers of tetradecamers.[23]

Many strategies have been used to characterize the extent of nonspecific aggregation during ESI.[24-27] Klassen and coworkers pioneered the use of the "reporter molecule method" for protein-protein[25] and protein-ligand[26] complexes, in which measurements of the extent of aggregation during ESI for species that do not interact in solution are used to quantify the contribution of nonspecific aggregation to observed gas-phase oligomer distributions. The reporter molecule method reduces the bias of nonspecific interactions to measurements of binding affinities in solution. However, from those measurements alone, it is challenging to determine the contributions from different aspects of the ESI process, *e.g.*, initial droplet sizes

versus droplet fission, to nonspecific aggregation. Statistical approaches have also been used to relate the extent of aggregation during ESI to the bulk concentration of the analyte and the number of copies of an analyte present in a droplet, using either a log-normal distribution of diameters[12,28,29] or discrete diameter[13,14,27] for the droplet. For example, Monte Carlo simulations suggest that the extent of nonspecific aggregation observed in native mass spectrometry of solutions containing different concentrations of a dimeric protein were consistent with the aggregation of analytes from a 24±3 nm radius droplet of the initial solution.[27] Using that effective droplet size, Monte Carlo simulations agreed well with the observed extent of aggregation during ESI for selected protein complexes that do not form higher-order complexes in solution.[27]

The objective of this study is to use Poisson statistics and measurements of droplet size distributions, flow rates, and the extent of protein aggregation during electrokinetic nanoESI as a function of the ionization current to elucidate the factors that mitigate nonspecific aggregation in electrokinetic nanoESI. Low flow rates (less than 10 nL min^{-1}) and small initial droplet diameters ~60 nm are observed at ionization currents near the threshold of ion formation (30 nA). Both the flow rate and initial droplet diameters increased monotonically with ionization current; at 400 nA we observed evidence for initial droplets that had diameters of ~500 nm, which are comparable to those produced from constant-flow ESI sources.[16,17,30] Based on measured droplet sizes, probability calculations show the extent of nonspecific aggregation depends on ionization current and analyte concentration. For example, the majority of the occupied droplets that are less than 100 nm from solutions with 4 μM analyte contain a single analyte. In contrast, the majority of occupied droplets that are greater than 100 nm from solutions with 4 μM analyte contain multiple analytes, which could lead to nonspecific aggregation during

desolvation. The predictions from these calculations are generally consistent with our measurements of nonspecific aggregation observed from ion mobility spectrometry of charge-reduced droplets containing myoglobin and standard native ion mobility mass spectrometry experiments. These results provide insights into the advantages of small initial droplet diameters for obtaining accurate oligomeric distributions of protein complexes in native mass spectrometry experiments.

2.3 Experimental Methods

2.3.1 Electrokinetic NanoESI. The ion source used for these experiments consists of a platinum wire electrode inserted into a borosilicate capillary emitter filled with ~3 μL of solution. The capillary has an inner diameter of 0.78 mm that was pulled to a tip with an inner diameter of 1 to 3 μm using a micropipette puller (Sutter Instruments Model P-97; Novato, CA). A Bertan Power Supply (Model 205B-10R or 205B-03R; Hauppauge, NY) controlled the potential of the platinum wire, which was in direct contact with the solution. Ionization currents were measured using a digital multimeter (Jameco Benchpro DT 830B; Belmont, CA) that was positioned between the power supply and the platinum wire electrode. In most experiments, the electrospray potential was adjusted to maintain constant current.

2.3.2 Flow Rate. Flow rates were determined using the difference in the weight of the capillary before and after spraying at a constant ionization current for a timed interval, then converting that difference to a volume using the density of aqueous 200 mM ammonium acetate (1.00 g cm^{-3}). The capillary and tip holder were weighed using an analytical balance (Mettler Toledo XS105; Columbus, OH). Errors were propagated from the manufacturer's specification for the accuracy of the balance (±0.01 mg) and are consistent with technical replicates. Mass

spectra were acquired simultaneously using a Waters Synapt G2 HDMS (Wilmslow, United Kingdom) to confirm ionization.

2.3.3 Apparent Droplet Size Distributions. The distributions of droplet diameters produced by the electrokinetic nanoESI source were measured using charge reduction ion mobility analysis with a differential mobility analyzer.[31-35] An ESI capillary containing 0.1% by volume sucrose in aqueous 200 mM ammonium acetate was positioned less than 5 mm from a 10 mCi ^{210}Po source (Nucleospot; Grand Island, NY). This source produces roughly equal concentrations of cations and anions from trace species in the air[36] surrounding the sampled droplets. Via droplet-ion collisions, droplets are charge reduced, which mitigates Coulomb fission. Droplets hence evaporate with minimal fissions, leaving non-volatile residue clusters whose sizes (diameters) are directly linked to the initial droplet size.[37] After exposure to the ^{210}Po generated ions, the residue clusters are additionally brought towards a known charge distribution[38] in which most have charges states of 0, –1, or +1, but multiply charged residue clusters can remain if clusters do not achieve this steady charge distribution, a common occurrence for droplets generated by ESI. The resulting sucrose clusters were mobility-filtered using a differential mobility analyzer[39] (TSI Model 3085; Shoreview, MN) and detected using a condensation particle counter[40] (TSI Model 3786), which were operated as a scanning mobility particle sizer.[41] Using data inversion,[42] the residue and droplet size distributions were inferred.

2.3.4 Drift Tube Ion Mobility. In conjunction with charge reduction via ^{210}Po generated ions, ion mobility measurements were also made on electrokinetic nanoESI generated ions using a drift-tube ion-mobility spectrometer (DT-IMS) operated at atmospheric pressure with a counterflow of gas.[43] The drift region of the DT-IMS employed is 224 mm long and consists of 20 stainless steel ring electrodes that have a 40 mm inner diameter, 10 mm width, and are

separated by 2 mm wide insulators. A 9 kV DC potential was applied to the first ring electrode; the potential decreases nearly linearly across the drift tube[43] and establishes a uniform axial electric field. After charge reduction (again using a ^{210}Po source) and subsequent desolvation, the ions entered the drift region and were separated based on their mobilities and quantified by their arrival times at a condensation particle counter placed downstream of the DT-IMS.

2.4 Results and Discussion

2.4.1 Native Electrokinetic NanoESI. Most ESI droplet size studies have used externally controlled flow rates and large inner diameter capillaries (10s to 100s μm, constant-flow ESI). These studies have shown that droplet sizes depend on the applied voltage (and therefore ionization current),[44] flow rate,[45] and capillary orifice diameter.[46] In contrast, few studies have focused on the droplet sizes generated from nanoESI using electrokinetic controlled solution flow through smaller inner diameter capillaries (less than 5 μm), *i.e.*, the conditions used most frequently for native mass spectrometry. To investigate the effects of applied voltage, and therefore current, on the flow rates in electrokinetic nanoESI, a solution containing 4 μM myoglobin from horse heart (selected arbitrarily) in 200 mM ammonium acetate at pH = 7.0 was electrosprayed using a range of currents and typical conditions for native mass spectrometry. Flow rates of 1.2 to 6.4 nL min^{-1} were measured using currents from 30 to 260 nA (Figure 2.1) and a different tip for each measurement. For comparison, currents of less than 100 nA are used for most applications of native mass spectrometry performed in our lab. When the same tip was used for each measurement, a sudden increase in the flow rate, to greater than 20 nL min^{-1}, was often observed using higher ionization currents (between 220 and 280 nA). After this sudden increase, subsequent flow rates measured using lower currents were greater than those measured

originally. The irreversible change in flow rate is attributed to physical deformation of the capillary tip.

The flow rates measured here are slower than those reported previously for similar electrokinetic nanoESI sources in which the potential was applied to a thin gold coating on the outside of the capillary. For example, using gold-coated capillaries and ionization currents of 10, 16, and 10 to 145 nA, flow rates of 20,[18] 20,[47] and 9 to 589[19] nL min^{-1}, respectively, have been reported. Those studies used different capillaries and solvents other than the 200 mM ammonium acetate used in this work, which may account for the differences in flow rate (*e.g.*, different surface tensions). In contrast, constant-flow ESI sources generally use flow rates in the µL min^{-1} range.[18,20]

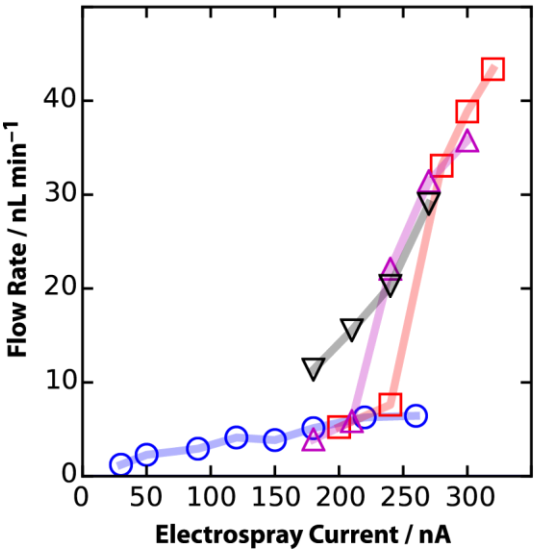

Figure 2.1. Representative flow rates measured as a function of ESI current. When using a new capillary at each current (*blue circles*), flow rates remained less than 10 nL min^{-1} over a broad range of currents. When using a single capillary and monotonically increasing the current (*red squares*), the flow rates exhibited a sharp increase in flow rate at currents greater than 200 nA. The results shown using *magenta triangles* are from a replicate of the preceding experiment and exhibited similar trends. Immediately after acquiring those results and using the same capillary, flow rates were measured using monotonically decreasing currents (*black triangles*). The latter flow rates are greater than those measured using monotonically increasing currents, suggesting that the capillary was compromised while using high currents. The uncertainties in flow rate are comparable to size of markers plotted.

2.4.2 Initial Droplet Size Distributions. To investigate the effects of flow rate from the electrokinetic nanoESI source on droplet size, charge reduction ion mobility measurements[31-35] of sucrose residue clusters were used to infer droplet size distributions. The residue measurement approach (as described in the *Experimental Methods*) has been used previously to characterize droplet size distributions from ESI and is considered a reliable, albeit indirect, means to estimate original ESI droplet size.[37] Figure 2.2A shows the distribution of apparent initial droplet diameters as a function of electrospray potential; the corresponding currents are also shown. Figure 2.3A shows the distribution of initial droplet diameters determined using an ionization current of 30 nA, which is near the threshold for ionization. This distribution has a mean diameter of ~60 nm. However, we consider this to be an upper limit for the mean; the condensation particle counter employed has a lower detection limit near 4.5 nm,[40] hence residue clusters corresponding to droplets smaller than 45 nm in diameter (4.5 nm and below) were not detected efficiently.

In most native mass spectrometry experiments, electrokinetic nanoESI sources are operated near the threshold for ionization. Our results indicate that this results in the formation of very small initial droplets. These droplet sizes are considerably smaller than those reported previously using constant-flow ESI sources (even those qualified as "nano-ESI" sources). Using similar implementations of the residue measurement approach and constant-flow ESI sources, Chen *et al*. reported 280 nm droplets using a current of 300 nA[37] and Hogan *et al*. reported 170.56 nm diameter droplets using currents of 200 to 300 nA.[11] Light scattering has also been used to characterize the droplets produced by constant-flow ESI sources, but typically for droplets that are significantly larger than those in the present study (e.g., ~25 μm).[17]

Increasing the ionization current results in the formation of larger droplets (Figure 2.2A, subpopulation III). Interestingly, additional features are also present at currents greater than 50 nA. For example, the distribution of apparent droplet diameters determined using an ionization current of 75 nA is shown in Figure 2.4A and exhibits features for subpopulations with mean apparent diameters near 220, 140, and 75 nm. With increasing ionization current, features for three subpopulations (labeled I, II, and III, respectively) persist with monotonically increasing diameters.

We propose two possible assignments for subpopulations I and II. The first candidate assignment is that subpopulations I and II correspond to the progeny droplets resulting from Coulomb fission from subpopulations II and III, respectively. Though satellite features have been detected in prior examinations of ESI generated droplets (leading to bimodal distributions),[15,37,48] the appearance of such monomodal progeny distributions has not been reported in other studies using the residue measurement approach. This result would be consistent with droplet fission occurring faster than charge reduction. The rate of droplet evaporation (in terms of diameter) increases with decreasing droplet size,[49] therefore smaller droplets can more readily access the Rayleigh limit before they are fully charged reduced relative to larger droplets produced using constant-flow electrospray sources. For comparison, modelling of collisions between charged particles and a charged aerosol that is 200 nm in diameter suggests that charge reduction will occur on a millisecond timescale,[50] whereas droplet fission from submicron droplets above the Rayleigh limit can occur on the microsecond time scale.[48]

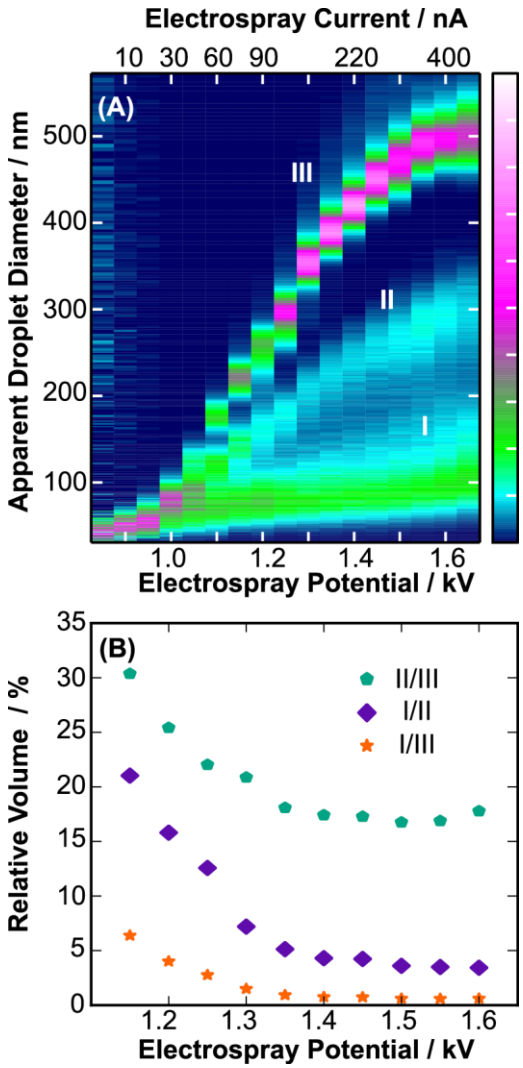

Figure 2.2. (A) A heat map of apparent droplet diameters as a function of increasing potential/current. As the ionization current increases, the initial droplet diameters increase (subpopulation III) and additional features appear (subpopulations I and II). (B) The masses of the progeny droplets relative to the parent droplets based on the apparent diameters for subpopulation II from subpopulation III (*turquoise pentagons*), subpopulation I from subpopulation II (*purple diamonds*), and subpopulation I from subpopulation III (*orange stars*).

Figure 2.2B shows that, using the first candidate assignment, the volumes of the droplets in subpopulation II are 20% to 30% of those in subpopulation III. These values are similar to those reported in early measurements of mass loss during droplet fission of micron-scale droplets,[51] but considerably greater than values reported based on more contemporary measurements (1% to 5%).[17,52-54] Although those studies[17,51-54] all probed droplets that were considerably larger (4 to 200 μm), the significant differences in mass loss strongly disfavor the assignment of subpopulation II as the progeny of subpopulation III. Furthermore, the formation of such large progeny droplets (20% to 30% relative mass) would significantly broaden subpopulation III due to the loss of mass from the parent droplets.

The second candidate assignment is that subpopulation II is composed of doubly charged analogues of subpopulation III, which would have greater mobility and appear to have smaller diameters in this analysis that assumes that all ions are singly charged. Subpopulation I is then assigned to the progeny droplets formed via Rayleigh fission of droplets that appear as subpopulations II and III. Figure 2.2B shows that, using these assignments, the droplets in subpopulation I have comparable relative volumes to those reported previously.[17,52-54] Furthermore, the actual diameters of doubly charged forms of subpopulation II would be twice their apparent diameters, which would be similar to, albeit slightly larger than, the apparent diameters observed for subpopulation III. Therefore, these results are most consistent with the second candidate assignment and the presence of a non-negligible number of multiply charged residues remaining in the aerosol phase after exposure to the charge reduction source.

2.4.3 Theoretical Nonspecific Aggregate Distributions. The frequency of nonspecific aggregates, assuming analyte concentrations of 0.4, 4.0, and 40 μM was predicted from the

experimental droplet size distributions using the Poisson distribution. First, the mean aggregate size (number of monomers per aggregate), $\bar{n}$, is:

$$\bar{n}(D, C) = C \times \frac{4\pi}{3}\left(\frac{D}{2}\right)^3 \times N_A \quad (2.1)$$

where D is the droplet diameter, C is the analyte concentration, and N_A is Avogadro's number. Assuming Poisson statistics, the probability of each aggregate size, n, is:

$$P(n, D, C) = \frac{\bar{n}(D,C)^n e^{-\bar{n}(D,C)}}{n!} \quad (2.2)$$

Prior studies using Equation 2.2 to examine ESI-induced aggregation used either a log-normal distribution[12,28,29] or a discrete diameter[13,14] for the droplet. Here, we consider the total aggregate distribution expected from these experiments, which depends on the experimental droplet size distribution $I(D)$ and Equation 2.2:

$$P_{total}(n, C) = \sum_D [I(D)P(n, D, C)] \quad (2.3)$$

Note that this approach does not account for the volume of the analyte. This effect is expected to be negligible for small proteins and aggregate sizes, but it will be increasingly significant with increasing droplet occupancy and analyte size. Furthermore, this analysis does not consider any protein-specific effects that may affect nonspecific aggregation.

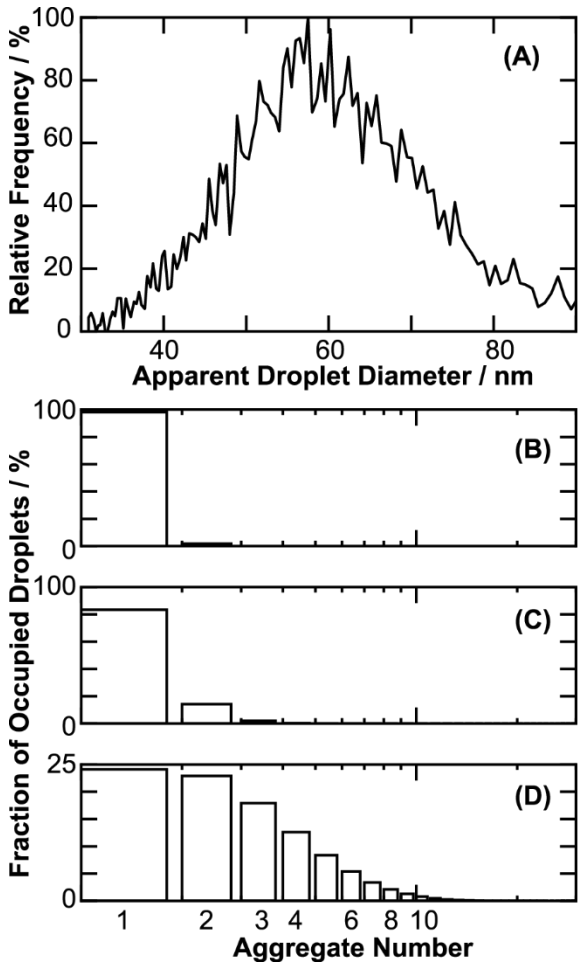

Figure 2.3. (A) Droplet size distribution measured using an electrospray current of 30 nA. The total probability for each aggregate number was calculated using Equation 2.3, the experimental droplet size distribution in (A), and analyte concentrations of 0.4 (B), 4 (C), and 40 (D) μM.

The total aggregate distribution expected for the apparent droplet size distribution shown in Figure 2.3A was calculated using concentrations of 0.4, 4.0, and 40 μM and are shown in Figures 2.3B, 2.3C, and 2.3D, respectively. This analysis suggests that the fraction of occupied droplets containing a single analyte is 98%, 83%, and 24% for 0.4, 4, and 40 μM analyte concentrations, respectively. Thus when using the lowest concentrations and an ionization current of 30 nA, which is similar to that used in many structural biology applications, excellent fidelity between the aqueous and gas-phase oligomeric states will be achieved.

The distribution of apparent droplet diameters determined using an ionization current of 75 nA is shown in Figure 2.4A and exhibits features for subpopulations with mean apparent diameters near 220, 140, and 75 nm (III, II, and I, respectively). The total aggregate distribution expected for each subpopulation assuming that the apparent droplet diameters accurately reflect the actual droplet diameters and a concentration of 4 μM are shown in Figures 2.4B, 2.4C, and 2.4D, respectively. This analysis suggests that 67% of the occupied droplets within subpopulation I contain a single analyte, which will yield ions with the correct stoichiometry after desolvation, whereas 33% contain multiple analytes, which may yield nonspecific aggregates (Figure 2.4B). Occupied droplets within subpopulation II are large enough to contain a wider range of aggregate sizes with a 19% probability of containing three analytes (trimer, Figure 2.4C). Greater than 99% of droplets that are within subpopulation III contain multiple analytes (Figure 2.4D). Therefore, oligomeric state distributions determined using droplets that are ~200 nm or larger will deviate radically from the corresponding solution-phase distributions.

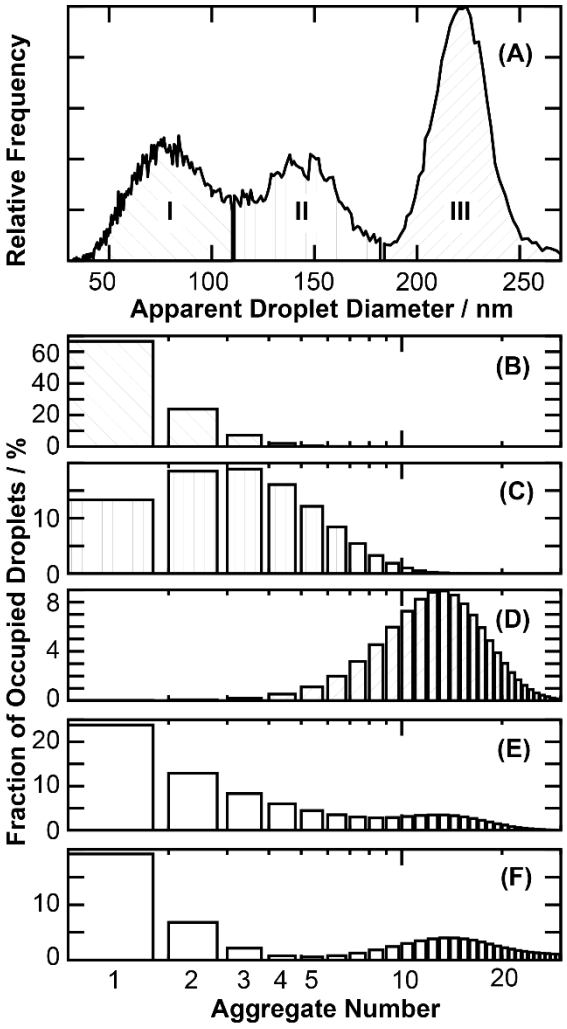

Figure 2.4. (A) Droplet size distribution measured using an electrospray current of 75 nA, which includes contributions from subpopulations I, II, and III. The probability for each aggregate number was calculated using Equation 2.3, an analyte concentration of 4 μM, and assuming that the distribution of apparent droplet diameter accurately reflects the actual distribution of droplet diameters. (B), (C), and (D) show results for subpopulations I, II, and III, respectively. (E) shows the probability for each aggregate number calculated for the entire distribution using the same assumption. (F) shows the probability for each aggregate number calculated assuming that subpopulation II is for doubly charged ions; thus the actual diameters are twice the apparent diameters. Analogous plots determined using concentrations of 0.4 and 40 μM are shown in Figures S2.1 and S2.2, respectively.

The total aggregate distribution for the entire apparent droplet size distribution using a concentration of 4 μM is shown in Figure 2.4E. This analysis suggests that 24% of the occupied droplets contain a single analyte, whereas 76% contain multiple analytes and may lead to nonspecific aggregates. As discussed earlier, it is likely that subpopulation II is attributable to doubly charged ions. In that case, the actual diameters of these droplets are likely twice that of the apparent diameters due to their increased mobilities. The actual volumes of those droplets are eight-fold greater than that suggested by their apparent diameters. Figure 2.4F shows the total aggregate distribution expected using those assignments. This analysis suggests that only 19% of the droplets contain a single analyte, whereas 81% contain multiple analytes. Analogous distributions determined using the 75 nA droplet-size distribution and analyte concentrations of 0.4 and 40 μM are shown in Supporting Information Figures S2.1 and S2.2, respectively, which further illustrate the advantage of using lower analyte concentration to mitigate nonspecific aggregation.

2.4.4 Nonspecific Aggregation During Native Charge-Reduction ESI. The effects of current and concentration on nonspecific aggregation were measured experimentally using varying concentrations of myoglobin in aqueous 200 mM ammonium acetate solutions. Myoglobin is a 17.6 kDa protein that exists as a monomer in solution, thus, the presence of higher-order oligomers can be attributed to nonspecific aggregation. ESI droplets were charge reduced using ^{210}Po and the resulting ions were analyzed using an atmospheric pressure aspirating drift tube ion mobility spectrometer (DT-IMS).[43] Separation in drift time depends on analyte size and shape, therefore, drift times increase with increasing oligomeric size.

The drift times measured using 4 μM myoglobin solutions and ionization currents ranging from 30 to 200 nA are shown in Figure 2.5A. The intense feature centered near 2.50 s

corresponds to monomeric myoglobin. Features at longer drift times correspond to higher-order oligomers of myoglobin. At the lowest stable current measured from the electrokinetic nanoESI source (30 nA), monomeric myoglobin was observed predominately (at least 90% relative abundance). This result is consistent with that from Poisson statistics that estimated 83% monomeric abundance for the apparent droplet size distribution measured at 30 nA. As the ionization current was increased, a feature corresponding to a relatively low abundance of nonspecific dimers appeared near 3.25 s. At 200 nA, features that are assigned to trimers (4.00 s) and tetramers (4.75 s) also appeared. These results are generally consistent with the analysis based on apparent droplet size measurements and the Poisson distribution, which indicate a significant increase in the extent of nonspecific aggregation with increasing ionization current and the concomitant increase in droplet sizes.

To test the dependence of nonspecific aggregation on concentration, increasing concentrations of myoglobin (0.4, 4.0, and 40 μM) in 200 mM ammonium acetate (Figure 2.5B) were analyzed using DT-IMS. A 30 nA current was used to minimize the formation of larger droplets. Consistent with the analysis above, increasing concentrations of myoglobin result in the formation of higher-order nonspecific aggregates due to increased droplet occupancy.

The percent of detected myoglobin monomer was calculated as functions of current (Figure 2.5E) and concentration (Figure 2.5F). When droplets were charge-reduced, there was a significant decrease in the relative abundance of monomer, from 91% to 59%, with increasing current. Therefore, there was a concomitant increase in nonspecific aggregate formation with increasing current. This trend also occurred with increasing concentration of myoglobin at a constant ionization current of 30 nA; the presence of monomer decreased from 91% to 65% with increasing concentration. These results are greater than the predicted % monomer as a function

of concentration determined using the apparent droplet size distribution in Figure 2.3A and Poisson distribution (Figure 2.5F), which shows a decrease from 99% to 24% over the same range of concentrations. These differences suggest that the DT-IMS instrument may have a detection bias or that not all proteins in a single, charge-reduced droplet go on to form nonspecific aggregates.

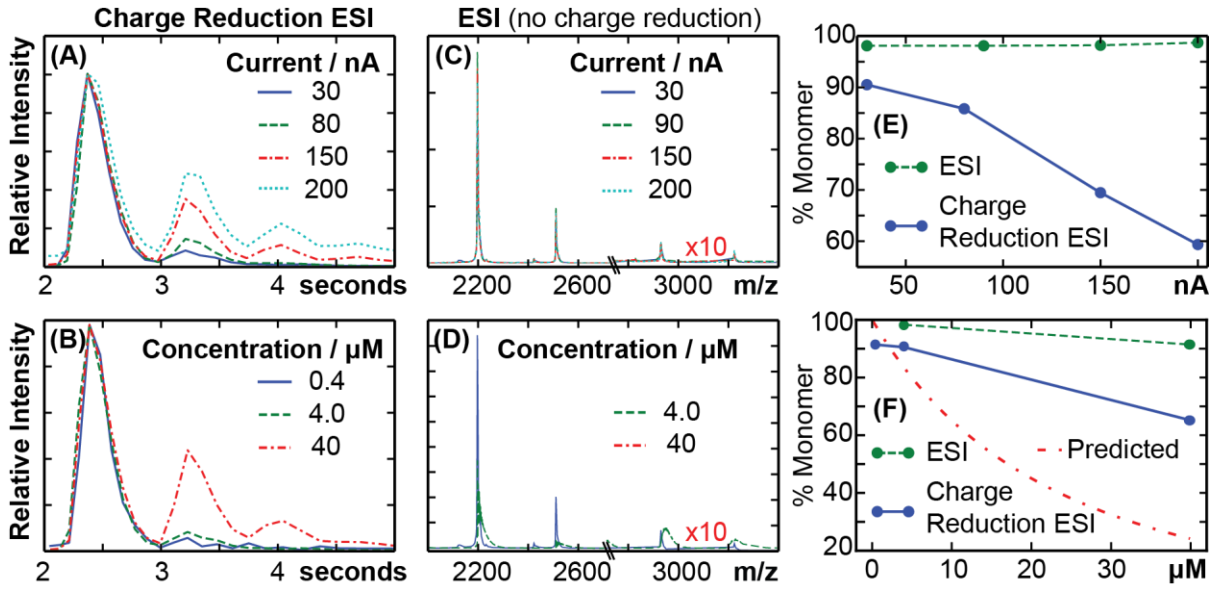

Figure 2.5. (A) DT-IMS arrival-time distributions for 4.0 µM myoglobin in 200 mM ammonium acetate measured using currents of 30, 80, 150, and 200 nA with charge reduction. Increasing current increases the abundance of higher-order aggregates. (B) DT-IMS arrival-time distributions for 0.4, 4.0, and 40 µM myoglobin measured using a current of 30 nA with charge reduction. Nonspecific dimers increase greatly in intensity with increasing concentration. (C) Mass spectra for 4.0 µM myoglobin measured using currents of 30, 90, 150, and 200 nA. (D) Mass spectra of 4.0, and 40 µM myoglobin measured using a current of 30 nA. (E) summarizes the results in (A) and (C). (F) summarizes the results in (B), (D), and that obtained using the apparent droplet size distribution shown in Figure 2.3A and Poisson statistics.

2.4.5 Nonspecific Aggregation During Native ESI. The preceding experiments all used charge-reduction ESI, in which ESI is performed in the presence of ^{210}Po that reduces the number of charges on the droplets and inhibits Rayleigh fission.[37] In contrast, most native mass spectrometry experiments do not use charge reduction during ESI and the resulting droplets are more likely to exceed the Rayleigh limit and undergo Coulomb fission. In order to investigate these effects, nonspecific aggregation of myoglobin was characterized as a function of analyte concentration and ionization current using native electrokinetic nanoESI.

Ion mobility mass spectra from solutions containing 4.0 and 40 μM myoglobin were measured using a range of ionization currents (mass spectra shown in Figure 2.5C). The spectrum of 4.0 μM myoglobin ions at an ionization current of 30 nA was additionally compared to a spectrum of 40 μM myoglobin ions at the same ionization current (Figure 2.5D). With an increase in concentration, there was a shift to higher *m*/*z* due to adduction of small ions. The arrival time distributions confirmed that the peaks for the monomers and dimers appear at unique *m*/*z* values in these experiments.

For multiply charged droplets, the relative abundance of nonspecific aggregates (~2%) depended weakly on current and concentration over the ranges investigated. This result is consistent with the increased formation of smaller droplets resulting from fission events (Figures 2.5E and 2.5F). Furthermore, this result suggests that monomeric ions resulting from these smaller droplets are detected with greater efficiency in the IM-MS experiments than the corresponding ions of aggregates from larger droplets. This result is in contrast to experiments using charge-reduced droplets that preserved monomeric oligomers at low currents (less than 50 nA) and concentrations (0.4 μM), but produced increasing abundances of higher-order aggregates with both increasing current and concentration. However, the relative abundance of

monomers in the DT-IMS experiments is still less than expected based on the analysis of droplet size distributions measured using the same charge-reduction ESI source.

2.5 Conclusions

Over the last two decades, native mass spectrometry has established itself as a powerful tool for determining the stoichiometry and binding constants of noncovalent interactions in solution. This approach leverages the fidelity between the distributions of noncovalent complexes in solution and in the gas phase, although any nonspecific aggregation that occurrs during the ionization process will bias these results. In this work, we evaluated the factors that contribute to nonspecific aggregation in native electrokinetic nanoESI using measurements of flow rate, current, droplet size distributions, and nonspecific aggregation in conjunction with Poisson statistics. These results show that using a typical ionization current (30 nA) and concentration (4 μM) for native mass spectrometry, electrokinetic nanoESI yields low flow rates (less than 10 nL min^{-1}) and small initial droplets (~60 nm diameters) that predominately contain up to 1 analyte. Increasing the ionization current results in the formation of larger initial droplets that are more likely to contain multiple analytes, which may aggregate during solvent evaporation and result in the formation of nonspecific aggregates that would bias the gas-phase measurement.

Most of the experiments reported here used charge reduction during ionization, which reduces the number of Coulomb fission events that occur during desolvation. The formation of progeny droplets decreases the fraction of occupied droplets that contain multiple analytes, consistent with decreased nonspecific aggregation observed in experiments without charge reduction relative to experiments with charge reduction. The combination of very small initial

droplet sizes (~60 nm) and increased droplet fission in electrokinetic nanoESI without charge reduction has enabled the success of native mass spectrometry in quantifying the stoichiometries and affinities of noncovalent interactions in solution, even at μM concentrations.

2.6 Supporting Information. Figures S2.1 to S2.2.

2.7 Acknowledgements. M.F.B. and K.L.D. acknowledge support from the University of Washington. Support from US National Science Foundation Grant CBET- 1133285 was used to the purchase of consumables for operation of the charge reduction ESI experiments. D.R.O. acknowledges support from a National Science Foundation Graduate Research Fellowship.

2.8 References

(1) Ekeowa, U. I.; Freeke, J.; Miranda, E.; Gooptu, B.; Bush, M. F.; Perez, J.; Teckman, J.; Robinson, C. V.; Lomas, D. A. *Proc. Natl. Acad. Sci. U. S. A.* **2010**, *107* (40), 17146–17151.

(2) Uetrecht, C.; Barbu, I. M.; Shoemaker, G. K.; van Duijn, E.; Heck, A. J. R. *Nat. Chem.* **2011**, *3* (2), 126–132.

(3) Bleiholder, C.; Dupuis, N. F.; Wyttenbach, T.; Bowers, M. T. *Nat. Chem.* **2011**, *3* (2), 172–177.

(4) Zhou, M.; Morgner, N.; Barrera, N. P.; Politis, A.; Isaacson, S. C.; Matak-Vinkovic, D.; Murata, T.; Bernal, R. A.; Stock, D.; Robinson, C. V. *Science* **2011**, *334* (6054), 380–385.

(5) Hilton, G. R.; Benesch, J. L. P. *J. Roy. Soc. Interface* **2012**, *9* (70), 801–816.

(6) Pierson, E. E.; Keifer, D. Z.; Selzer, L.; Lee, L. S.; Contino, N. C.; Wang, J. C.-Y.; Zlotnick, A.; Jarrold, M. F. *J. Am. Chem. Soc.* **2014**, *136* (9), 3536–3541.

(7) Leney, A. C.; Pashley, C. L.; Scarff, C. A.; Radford, S. E.; Ashcroft, A. E. *Mol. BioSyst.* **2014**, *10* (3), 412–420.

(8) Hofstadler, S. A.; Sannes-Lowery, K. A. *Nat. Rev. Drug Discov.* **2006**, *5* (7), 585–595.

(9) Kitova, E. N.; El-Hawiet, A.; Schnier, P. D.; Klassen, J. S. *J. Am. Soc. Mass Spectrom.* **2012**, *23* (3), 431–441.

(10) Cubrilovic, D.; Barylyuk, K.; Hofmann, D.; Walczak, M. J.; Gräber, M.; Berg, T.; Wider, G.; Zenobi, *R. Chem. Sci.* **2014**, *5* (7), 2794.

(11) Hogan, C. J.; Kettleson, E. M.; Ramaswami, B.; Chen, D.-R.; Biswas, P. *Anal. Chem.* **2006**, *78* (3), 844–852.

(12) Hogan Jr., C. J.; Biswas, P. *J. Am. Soc. Mass Spectrom.* **2008**, *19* (8), 1098–1107.

(13) Li, M.; Guha, S.; Zangmeister, R.; Tarlov, M. J.; Zachariah, M. R. *Aerosol Sci. Technol.* **2011**, *45* (7), 849–860.

(14) Li, M.; Guha, S.; Zangmeister, R.; Tarlov, M. J.; Zachariah, M. R. *Langmuir* **2011**, *27* (24), 14732–14739.

(15) Gomez, A.; Tang, K. *Phys. Fluids* **1994**, *6* (1), 404–414.

(16) Olumee, Z.; Callahan, J. H.; Vertes, A. *J. Phys. Chem. A* **1998**, *102* (46), 9154–9160.

(17) Smith, J. N.; Flagan, R. C.; Beauchamp, J. L. *J. Phys. Chem. A* **2002**, *106* (42), 9957–9967.

(18) Juraschek, R.; Dülcks, T.; Karas, M. *J. Am. Soc. Mass Spectrom.* **1999**, *10* (4), 300–308.

(19) Schmidt, A.; Karas, M.; Dülcks, T. *J. Am. Soc. Mass Spectrom.* **2003**, *14* (5), 492–500.

(20) Tang, X.; Bruce, J. E.; Hill, H. H. *Anal. Chem.* **2006**, *78* (22), 7751–7760.

(21) Ghosal, S. *In Microfluidics and Microfabrication*; Chakraborty, S., Ed.; Springer US, **2010**; pp 87–112.

(22) Wilm, M.; Mann, M. *Anal. Chem.* **1996**, *68* (1), 1–8.

(23) Benesch, J. L. P.; Ruotolo, B. T.; Simmons, D. A.; Robinson, C. V. *Chem. Rev.* **2007**, *107* (8), 3544–3567.

(24) Hossain, B. M.; Simmons, D. A.; Konermann, L. Can. *J. Chem.* **2005**, *83* (11), 1953–1960.

(25) Sun, J.; Kitova, E. N.; Sun, N.; Klassen, J. S. *Anal. Chem.* **2007**, *79* (21), 8301–8311.

(26) Sun, N.; Sun, J.; Kitova, E. N.; Klassen, J. S. *J. Am. Soc. Mass Spectrom.* **2009**, *20* (7), 1242–1250.

(27) Lane, L. A.; Ruotolo, B. T.; Robinson, C. V.; Favrin, G.; Benesch, J. L. P. *Int. J. Mass Spectrom*. **2009**, *283* (1–3), 169–177.
(28) Lewis, K. C.; Dohmeier, D. M.; Jorgenson, J. W.; Kaufman, S. L.; Zarrin, F.; Dorman, F. D. *Anal. Chem*. **1994**, *66* (14), 2285–2292.
(29) Hogan, C. J.; Biswas, P. *Aerosol. Sci. Technol*. **2008**, *42*, 75–85.
(30) Wortmann, A.; Kistler-Momotova, A.; Zenobi, R.; Heine, M. C.; Wilhelm, O.; Pratsinis, S. E. *J. Am. Soc. Mass Spectrom*. **2007**, *18* (3), 385–393.
(31) Kaufman, S. L.; Skogen, J. W.; Dorman, F. D.; Zarrin, F.; Lewis, K. C. *Anal. Chem*. **1996**, *68* (11), 1895–1904.
(32) Bacher, G.; Szymanski, W. W.; Kaufman, S. L.; Zöllner, P.; Blaas, D.; Allmaier, G. *J. Mass Spectrom*. **2001**, *36* (9), 1038–1052.
(33) de la Mora, J. F.; Ude, S.; Thomson, B. A. *Biotechnol. J*. **2006**, *1* (9), 988–997.
(34) Pease, L. F.; Elliott, J. T.; Tsai, D.-H.; Zachariah, M. R.; Tarlov, M. J. *Biotechnol. Bioeng*. **2008**, *101* (6), 1214–1222.
(35) Bereszczak, J. Z.; Havlik, M.; Weiss, V. U.; Marchetti-Deschmann, M.; Duijn, E. van; Watts, N. R.; Wingfield, P. T.; Allmaier, G.; Steven, A. C.; Heck, A. J. R. *Anal. Bioanal. Chem*. **2014**, *406* (5), 1437–1446.
(36) Maißer, A.; Thomas, J. M.; Larriba-Andaluz, C.; He, S.; Hogan Jr., C. J. *J. Aerosol Sci*. **2015**, *90*, 36–50.
(37) Chen, D.-R.; Pui, D. Y. H.; Kaufman, S. L. *J. Aerosol Sci*. **1995**, *26* (6), 963–977.
(38) Gopalakrishnan, R.; Meredith, M. J.; Larriba-Andaluz, C.; Hogan Jr., C. J. *J. Aerosol Sci*. **2013**, *63*, 126–145.
(39) Chen, D.-R.; Pui, D. Y. H.; Hummes, D.; Fissan, H.; Quant, F. R.; Sem, G. J. *J. Aerosol Sci*. **1998**, *29* (5–6), 497–509.
(40) Liu, W.; Kaufman, S. L.; Osmondson, B. L.; Sem, G. J.; Quant, F. R.; Oberreit, D. R. *J. Air Waste Manag. Assoc*. **2006**, *56* (4), 444–455.
(41) Wang, S. C.; Flagan, R. C. *Aerosol Sci. Technol*. **1990**, *13* (2), 230–240.
(42) Wiedensohler, A.; Birmili, W.; Nowak, A.; Sonntag, A.; Weinhold, K.; Merkel, M.; Wehner, B.; Tuch, T.; Pfeifer, S.; Fiebig, M.; Fjäraa, A. M.; Asmi, E.; Sellegri, K.; Depuy, R.; Venzac, H.; Villani, P.; Laj, P.; Aalto, P.; Ogren, J. A.; Swietlicki, E.; Williams, P.; Roldin, P.; Quincey, P.; Hüglin, C.; Fierz-Schmidhauser, R.; Gysel, M.; Weingartner, E.; Riccobono, F.; Santos, S.; Grüning, C.; Faloon, K.; Beddows, D.; Harrison, R.; Monahan, C.; Jennings, S. G.; O'Dowd, C. D.; Marinoni, A.; Horn, H.-G.; Keck, L.; Jiang, J.; Scheckman, J.; McMurry, P. H.; Deng, Z.; Zhao, C. S.; Moerman, M.; Henzing, B.; de Leeuw, G.; Löschau, G.; Bastian, S. *Atmos. Meas. Tech*. **2012**, *5* (3), 657–685.
(43) Oberreit, D. R.; McMurry, P. H.; Hogan, C. J. *Aerosol Sci. Technol*. **2014**, *48* (1), 108–118.
(44) Gañán-Calvo, A. M.; Dávila, J.; Barrero, A. *J. Aerosol Sci*. **1997**, *28* (2), 249–275.
(45) Srikanth, A.; Karnawat, J.; Kushari, A. *Open Appl. Phys. J*. **2009**, *2*, 53–57.
(46) Alexander, M. S.; Paine, M. D.; Stark, J. P. W. *Anal. Chem*. **2006**, *78* (8), 2658–2664.
(47) El-Faramawy, A.; Siu, K. W. M.; Thomson, B. A. *J. Am. Soc. Mass Spectrom*. **2005**, *16* (10), 1702–1707.
(48) Peschke, M.; Verkerk, U. H.; Kebarle, P. *J. Am. Soc. Mass Spectrom*. **2004**, *15* (10), 1424–1434.

(49) *Handbook of Atomization and Sprays: Theory and Applications*, **2011** edition; Springer: New York, **2011**.
(50) Gopalakrishnan, R.; Hogan, C. J. *Phys. Rev. E Stat. Nonlin. Soft Matter Phys.* **2012**, *85* (2 Pt 2), 026410.
(51) Abbas, M. A.; Latham, J. *J. of Fluid Mech.* **1967**, *30* (04), 663–670.
(52) Richardson, C. B.; Pigg, A. L.; Hightower, R. L. *Proc. R. Soc. Lond. A* **1989**, *422* (1863), 319–328.
(53) Taflin, D. C.; Ward, T. L.; Davis, E. J. *Langmuir* **1989**, *5* (2), 376–384.
(54) Davis, E. J.; Bridges, M. A. *J. Aerosol Sci.* **1994**, *25* (6), 1179–1199.

Chapter 3

Investigating Ionization Mechanisms in the Gas Phase using Native Ion Mobility Mass Spectrometry

3.1 Abstract

Many mechanisms for the charging of macromolecules in electrospray ionization (ESI) have been debated and proposed. Here, native mass spectrometry and ion mobility spectrometry were used to investigate the charged-residue model, which is most often used to explain the ionization of macromolecules using the Rayleigh limit, and the more recently proposed combined charged residue field emission model. The average charge states of proteins ranging in mass from 8 – 468 kDa were measured in four different buffers (ammonium acetate, methylammonium acetate, dimethylammonium acetate, and trimethylammonium acetate) at a biologically relevant pH (~7.0). The average charge states of native proteins in each of the four buffers are less than what the Rayleigh limit estimates. Additionally, the average charge states do not correlate with what the combined charged residue field emission model suggests; the charge state of a macromolecule depends on the charge carriers emitted at specific critical field strengths on the surface of the droplet. These results indicate that there is still more work ahead to fully understand the ionization of macromolecules using ESI.

3.2 Introduction

Native ion mobility mass spectrometry (IMMS) is an important tool in investigations of protein and protein complex stoichiometry and dynamics due to its speed and sensitivity.[1–4] In these investigations, it is important to maintain protein and protein complex structures and any noncovalent interactions. Native-like ions are produced from a solution containing protein dissolved in ~200 mM ammonium acetate at a biologically relevant pH using nanoelectrospray ionization (nanoESI), which is a soft-ionization technique.[5] The resulting native mass spectra, using nanoESI, show narrower charge state distributions at lower *m*/*z* than those produced from conventional ESI methods.

The most widely accepted model used to explain the formation of multiply charged macromolecular ions is the charged-residue model (CRM).[6–8] In this model, neutral solvent molecules evaporate from the initial charged droplet until the Coulombic repulsion exceeds the surface tension of the droplet (the Rayleigh limit):[9]

$$z \cdot e = \pi(8\varepsilon_0\gamma)^{1/2}\mathrm{D}^{3/2} \tag{3.1}$$

where z is the number of charges, e is the elementary charge, ε_0 is the permittivity of free space, γ is the surface tension (72 mN/m for water at 25 °C), and D is the droplet diameter. At this limit, Coulomb fission will result in the ejection of a progeny droplet with a smaller radius and a fraction of the charges of the precursor droplet.[10] This process repeats until complete desolvation results in the formation of a multiply charged, gas-phase ion.

The CRM is a useful model for approximating charge states of macromolecules, however, there are discrepancies between experimental results and predictions determined using Equation 3.1. The average charge states of native-like protein cations with masses ranging from 6 – 80 kDa were found to be less than those estimated using the Rayleigh limit and a surface

tension of water.[11] Given the differences between the average charge states of native-like ions measured experimentally and those predicted using the Rayleigh limit, Hogan *et al*. proposed the Combined Charged Residue Field Emission Model (CCRFEM).[11,12]

The CCRFEM states that both Coulomb fission (similar to the CRM) and small charge carrier emission from electrosprayed droplets (analogous to the ion evaporation model)[8,13] affect the average charge states of native-like ions. Small charge carrier emission occurs when the surface of an electrosprayed droplet reaches a critical field strength, E*. Once a charge carrier is emitted, the electric field strength decreases, preventing further charge-carrier emission. After neutral-solvent evaporation, the surface of the droplet will reach yet another E* at which another charge carrier will be emitted. The emission of charge carriers from a droplet is dependent on E* and their solvation energies. The charges on a macromolecule for a given E* is given by:[11,12]

$$z = \frac{\pi \varepsilon_0 E^*}{e} D^2 \tag{3.2}$$

where *D* is the macromolecule diameter (typically determined using a protein density of 1.0 g cm^{-3}). The observed average charge states measured by Hogan *et al.* were consistent with E* values of 3.53 and 2.95 V nm^{-1}.[12]

Allen *et al.* expanded on this work by measuring the average charge states of a broader range of proteins from 6 - 468 kDa in both positive and negative ion mode.[14] The terms in the Rayleigh limit are independent of polarity but the charge states of macromolecules are not; negative charge states are less than those of positive charge states.[2,6,14] In positive ion mode, the observed average charge states corresponded with E* values of 3.52, 2.95 and 2.3 V nm^{-1}. In negative ion mode, the measured average charge states were less than in positive mode resulting in lower E* values of 2.8, 2.3 and 1.9 V nm^{-1}. It was found that ions in both polarities had similar

structures despite differences in charge state. The results could not be verified using the Rayleigh limit and instead were explained using the CCRFEM.[14]

The CCRFEM states that the average charge state of a protein is dependent in part on the solvation energies of charge carriers present in droplets containing the protein.[12] For example, using a denaturing solution and adding 0.4% diethylamine decreases the average charge state of cytochrome *c* by 11%, even when the pH of the solution is held constant.[15] The solvation energy of diethylamine is lower than that of the denaturing solution alone, therefore, diethylamine will emit and take charges with it before complete desolvation of the droplet can occur.

Here we examine the effects that different charge carriers have on the average charge states of native-like proteins in positive and negative ion mode. Native mass spectra were measured for proteins ranging from 8 – 468 kDa in four different buffers: ammonium acetate, methylammonium acetate, dimethylammonium acetate and trimethylammonium acetate. The four buffers differ in cationic charge carrier and solvation energies. We find that the average charge states of native proteins decreases with decreasing solvation energies of the cation, also resulting in differences in E* compared to those determined using ammonium acetate. Finally, using the polarizable continuum model, solvation energies of possible charge carriers in solution were calculated and compared with E* results.

3.3 Experimental Section

All chemicals were purchased from Sigma-Aldrich. Solutions of 10 μM protein were initially diluted in 200 mM ammonium acetate at a biologically relevant pH to retain their native forms. The proteins were subsequently buffer-exchanged into 200 mM methyl ammonium acetate, dimethyl ammonium acetate, and trimethyl ammonium acetate. Each buffer was at a biologically relevant pH.

3.3.1 Ion Mobility Mass Spectrometry. Ions were produced using an electrokinetic nanoESI source[16] consisting of a platinum wire electrode inserted into a borosilicate capillary emitter that contained ~3 μL of solution. The capillaries have an inner diameter of 0.78 mm and were pulled to a tip with an inner diameter of ~1-3 μm using a micropipette puller (Sutter Instruments Model P-87, Novato, CA). Ion mobility mass spectrometry data were measured on a modified Waters Synapt G2 HDMS instrument in which the traveling-wave ion mobility cell was replaced with a radio-frequency confining drift cell.[17,18] Ω values were determined from plots of drift time versus reciprocal drift voltages, which ranged from 100 to 350 V.

3.3.2 Software. Average charge states were determined by fitting Gaussian functions to the distribution of charge states and the peak for each charge state. The mass of the protein and the average charge-state are first estimated and then optimized using functions implemented in SciPy.

3.4 Results and Discussion

3.4.1 Effects of methylated buffers on protein charge state. Figure 3.1A shows the positive average charge states measured for native-like proteins, ranging in mass from 8 - 468 kDa (Table 3.1). The proteins were sprayed from four buffer salts: ammonium acetate (AA),

methylammonium acetate (MA), dimethylammonium acetate (DA) and trimethylammonium acetate (TA). The average charge states measured here with AA buffer are within 2.4% of those determined previously using the same buffer salt, with the exception of ubiquitin (8%) and cytochrome *c* (13%) (Table 3.1).[14] Figure 3.1B shows the negative average charge states measured for the same native-like proteins in Table 3.1 sprayed from AA. The negative average charge states measured here are within 5% of those measured previously[14] with the exception of ubiquitin (8.7%) and are reported in Table 3.2.

In the charged residue model (CRM), the charge state of a macromolecule follows the Rayleigh limit (Equation 3.1). The average charge states of the native-like proteins from AA buffer are 69 to 90% of that predicted by the Rayleigh limit assuming a surface tension of water (72.8 mN/m) as shown in Figure 3.1A. The average charge states of these proteins continue to decrease from AA>MA>DA>TA. The relative differences in average charge state for proteins sprayed from these four buffers relative to those estimated using Equation 3.1 and a surface tension of water range from -0.9 to -15 (Figure 3.1C). Glutamate dehydrogenase (337 kDa) exhibits the greatest difference in average charge state, from AA to TA buffers, of 23%.

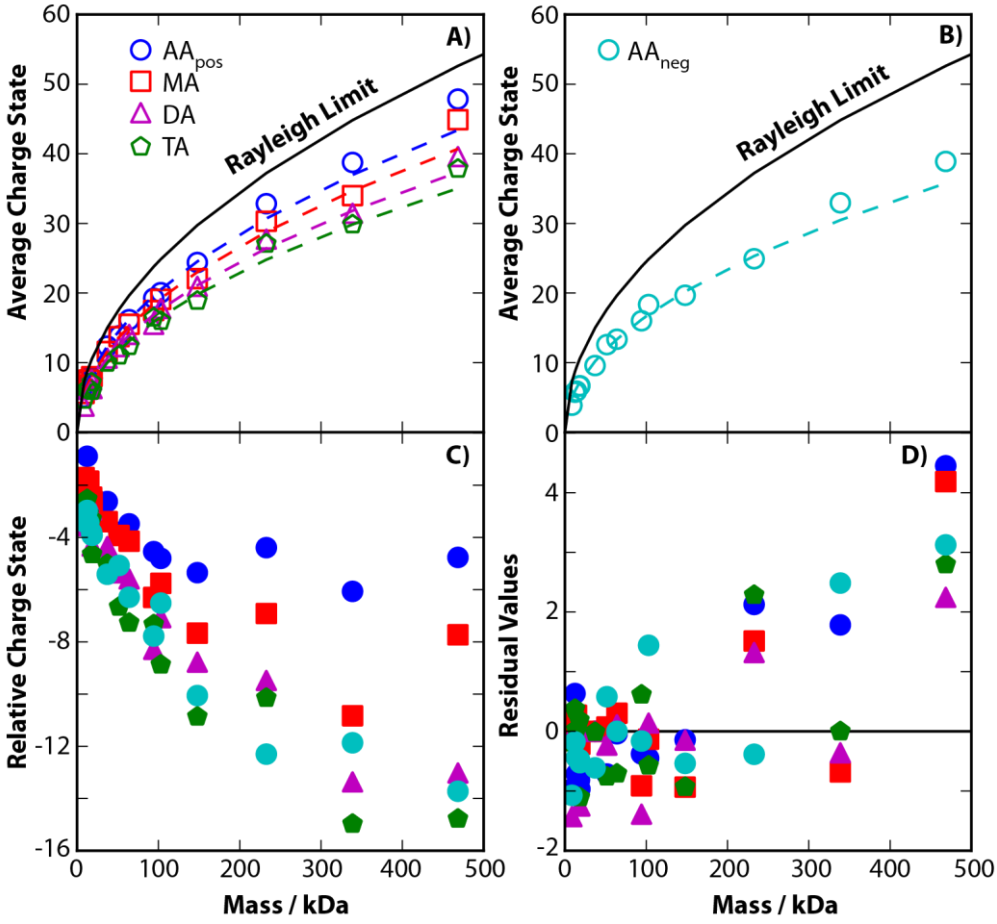

Figure 3.1. (A) Positive average charge states (<*z*>) of proteins i-xiv in ammonium acetate (AA_{pos}, *blue circles*), methylammonium acetate (MA, *red squares*), dimethylammonium acetate (DA, *purple triangles*) and trimethylammonium acetate (TA, *green pentagons*) are less than charge states determined using the Rayleigh limit (*solid line,* Equation 1) and a surface tension of water. (B) Negative <*z*> of proteins i-xiv in ammonium acetate (AA_{neg}, *cyan circles*) are also less than the Rayleigh limit. Best-fit lines for each solvent were determined by optimizing the surface tension using a least-squares minimization. (C) The change in <*z*> for each protein in buffers AA, MA, DA, and TA relative to their predicted charge state using Equation 1. (D) Residual values between measured <*z*> and those of the best-fit line.

Table 3.1. Masses and charge states of selected cations

	Protein	*n*	Mass (kDa)	z_{RL}	$\langle z \rangle_{AA, Allen}$[14]	$\langle z \rangle_{AA}$	$\langle z \rangle_{MA}$	$\langle z \rangle_{DA}$	$\langle z \rangle_{TA}$
i	ubiquitin	1	8.57	7.28	5.46	5.03	5.57	3.73	4.66
ii	cytochrome *c*	1	12.4	8.71	6.80	7.82	6.74	6.16	6.18
iii	α-lactalbumin	1	14.2	9.33	--	6.99	7.49	6.72	6.25
iv	myoglobin	1	17.9	10.4	--	7.80	7.99	7.49	7.14
v	β-lactoglobulin	1	18.4	10.6	7.96	7.77	7.98	6.27	5.95
vi	β-lactoglobulin	2	36.8	15.0	12.4	12.4	11.6	10.6	9.97*
vii	concanavalin A	2	51.6	17.7	--	13.8	13.7	12.3	11.0
viii	avidin	4	64.3	19.6	16.4	16.2	15.5	14.1	12.4
ix	enolase	2	94.2	23.8	--	19.2	17.5	15.5	16.5
x	concanavalin A	4	103	24.9	20.3	20.1	19.1	17.8	16.0
xi	alcohol dehydrogenase	4	148	29.7	24.8	24.4	22.1	21.0	18.9
xii	pyruvate kinase	4	233	37.2	33.6	32.8	30.3	27.7	27.1
xiii	glutamate dehydrogenase	6	337	44.8	39.3	38.8	34.0	31.5	29.8
xiv	β-galactosidase	4	468	52.6	48.8	47.9	44.9	39.6	37.8

AA = ammonium acetate, MA = methylammonium acetate, DA = dimethylammonium acetate, TA = trimethylammonium acetate

*= two measurements

Table 3.2. Masses and charge states of selected anions

	Protein	*n*	Mass (kDa)	z_{RL}	$\langle z \rangle_{AA, Allen}$[14]	$\langle z \rangle_{AA}$	$\langle z \rangle_{MA}$	$\langle z \rangle_{DA}$	$\langle z \rangle_{TA}$
i	ubiquitin	1	8.57	7.28	3.56	3.87	5.47*	5.01*	6.31*
iii	α-lactalbumin	1	14.2	9.33	--	5.90	6.47*	6.51*	6.49*
iv	myoglobin	1	17.9	10.4	--	6.63	6.51*	6.79*	6.92*
vii	concanavalin A	2	51.6	17.7	--	12.6	11.9*	11.4*	12.3*
viii	avidin	4	64.3	19.6	13.4	13.4	12.9*	13.0*	13.2*
x	concanavalin A	4	103	24.9	17.6	18.3	16.9*	16.1*	17.3*
xi	alcohol dehydrogenase	4	148	29.7	19.9	19.7	19.8*	20.1*	19.2*
xii	pyruvate kinase	4	233	37.2	25.6	24.9	24.3*	22.8*	24.8*

* = single measurement

According to the Rayleigh limit, the charge state of a protein is dependent on the surface tension of the droplet surrounding the protein. The surface tensions of all four buffers used in this study (AA, MA, DA and TA) in positive mode, as well as AA in negative mode, were estimated using a linear least squares regression between the Rayleigh limit and experimental average charge states (Figures 3.1A and 3.1B). The estimated surface tensions decreased from AA (0.050 N/m), MA (0.044 N/m), DA (0.037 N/m), to TA (0.032 N/m) in positive mode and the estimated surface tension of AA was 0.034 N/m in negative mode. While these values have not been verified via experiment, the decreasing surface tensions for each buffer could explain the decreasing charge states of the proteins. However, the surface tension of AA should not change based on polarity and therefore, the Rayleigh limit still does not account for lower charge states in negative ion mode relative to positive ion mode.

3.4.2 Combined charged residue field emission model. E* values (Table 3.3) were calculated using Equation 3.2[11,12] and the average charge states of 14 proteins sprayed from aqueous buffers AA, MA, DA and TA (Table 3.1). The diameters, *D*, of the proteins were determined using a density (ρ) of 1.00 g cm^{-3}.[12,14,19] E* values were then optimized using a linear least squares regression. Using the Q-test, it was determined that cytochrome *c* in AA buffer and ubiquitin in DA buffer are outliers and were not included in the optimization of E* values.

Table 3.3. Critical field strengths for each buffer

Buffer	$\mathbf{E^*_{1,+}}$ (V/nm)	$\mathbf{E^*_{2,+}}$ (V/nm)	$\mathbf{E^*_{3,+}}$ (V/nm)	$\mathbf{E^*_{1,-}}$ (V/nm)	$\mathbf{E^*_{2,-}}$ (V/nm)	$\mathbf{E^*_{3,-}}$ (V/nm)
AA	3.23 ± 0.12	2.74 ± 0.18	2.21 ± 0.28	2.65 ± 0.19	2.29 ± 0.18	1.89 ± 0.14
MA	3.40 ± 0.26	2.65 ± 0.30	2.06 ± 0.29	2.67 ± 2.68	2.14 ± 1.01	1.76 ± 0.54
DA	3.11 ± 0.29	2.40 ± 0.13	1.83 ± 0.61	2.73 ±	2.19 ± 0.80	1.68 ±
TA	2.89 ± 0.26	2.18 ± 0.10	1.74 ± 0.27	2.79 ±	2.21 ± 0.32	1.77 ± 0.20

Figure 3.2A shows the positive average charge states of 14 proteins in AA buffer plotted against their diameter. The Rayleigh limit is shown for comparison. According to the CCRFEM, a desolvating droplet contains multiple charge carriers or electrolytes that will emit from the droplet based on their solvation energies and the critical field strength, E*, at the surface of the droplet. Once the least solvated electrolyte is depleted from the droplet, the droplet continues to evaporate until it reaches another E*, at which another electrolyte will be emitted, carrying charge with it. The E* values for AA buffer in positive ion mode are 3.23, 2.74, and 2.21 V nm^{-1} and are within 4 to 8% of those measured previously.[14] The negative average charge states of the same proteins are shown in Figure S3.1 and are less than those in positive ion mode. The corresponding E* values for AA buffer in negative ion mode are 2.65, 2.29 and 1.89 V nm^{-1}.

The best-fit lines in Figure 3.2 correspond to each critical field strength and a specific electrolyte that is limiting the charge for a range of proteins. For instance, E_1* (the top-most dotted line in Figure 3.2A) corresponds to a value of 3.23 V/nm and is associated with an electrolyte that is limiting the charge of proteins ≤ 3.80 nm in diameter. E_2* (2.74 V/nm) is associated with a different electrolyte in solution that limits the charge of proteins that are within 3.84 to 6.60 nm in diameter.

Figures 3.2B, 3.2C, and 3.2D show the positive average charge states of the same 14 proteins and the best-fit critical field strengths for MA, DA and TA buffers, respectively. E* differs depending on the buffer composition, for example, E_1* for MA buffer (3.40 V/nm) is greater than that for AA buffer (3.23 V/nm) but E_2* for MA buffer (2.65 V/nm) is less than that for AA buffer (2.74 V/nm). This indicates that changing only the cationic species in the buffer does not result in a simple change in one E* value. In fact, all three E* values are changing with

buffer composition. Therefore, there are limits to the CCRFEM and its ability to predict charge states a priori.

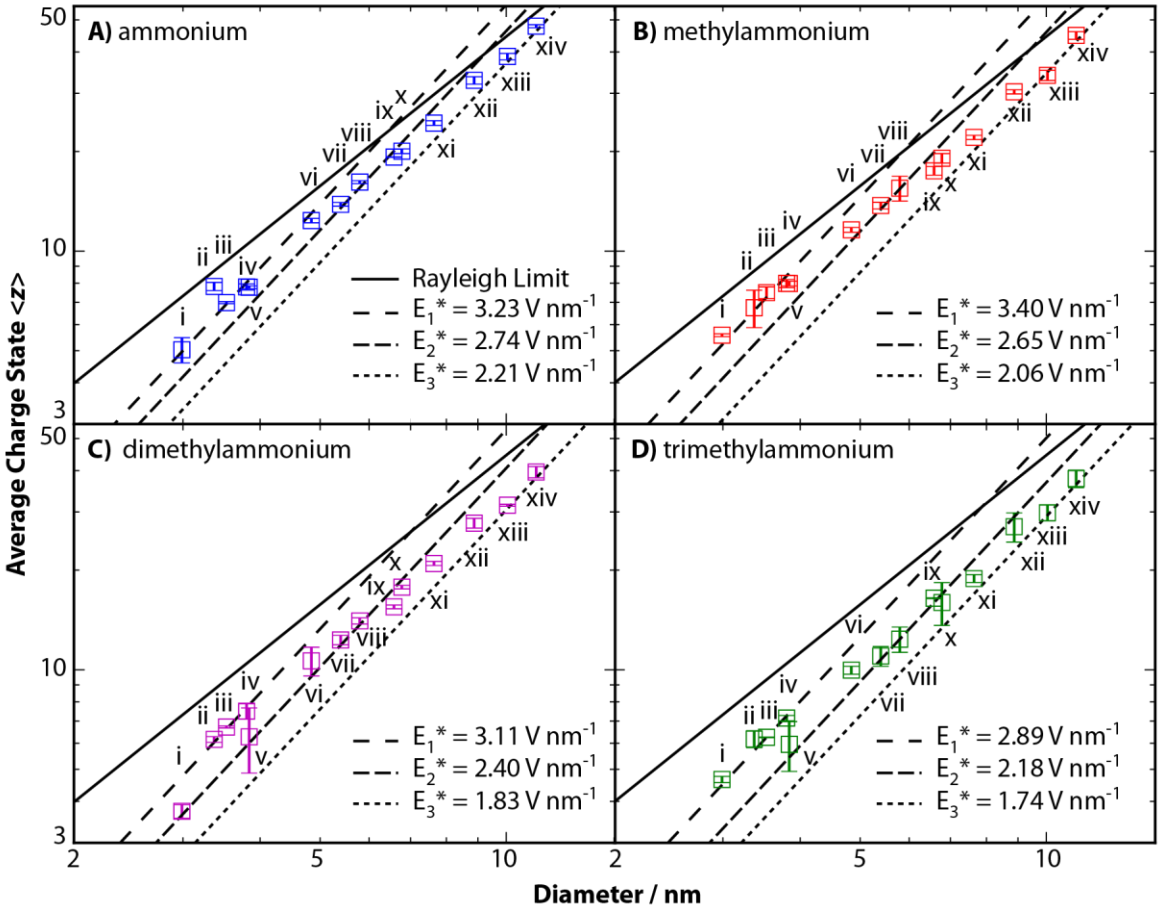

Figure 3.2. The average charge states, within 95% confidence, of 14 proteins ranging from 8.5 – 468 kDa were measured in four different buffers: (A) ammonium acetate, (B) methylammonium acetate, (C) dimethylammonium acetate and (D) trimethylammonium acetate. The best-fit critical field strengths (E*) for each buffer (dashed lines, Table 3.3) were determined using Equation 3.2 and a linear least-squares optimization. The Rayleigh limit (solid line, Equation 3.1) is shown for comparison.

3.4.3 Collision cross sections (Ω) of proteins. One possibility for the differences in charge states (and therefore E*) is a difference in protein conformation. For example, a protein in a more acidic environment will unfold and the measured Ω will be larger than that of the protein in its native conformation. In order to determine if the change in charge state is due to differences in conformation, the collision cross sections (Ω) of four proteins spanning a range of masses and stoichiometries (ubiquitin, α-lactalbumin, pyruvate kinase and β-galactosidase) were measured in each buffer.

In IMMS, gas-phase ions are separated by their mobility (K) as they travel through a weak electric field (E):

$$K = \frac{L}{t_D E} = \frac{L^2}{t_D V} \tag{3.3}$$

where L is the length of the drift cell, t_D is the observed drift time, and V is the voltage change across the drift cell. The gas-phase ions in each drift gas will be compared based on their collision cross sections (Ω), a measure of the relative size of an ion with a neutral background gas, which are calculated using the Mason-Schamp equation:[20]

$$\Omega = \frac{3ez}{16N}\sqrt{\frac{2\pi}{\mu k_B T}}\frac{1}{K} \tag{3.4}$$

where N is the drift-gas number density, μ is the reduced mass of the ion and drift gas, k_B is the Boltzmann constant and T is the drift-gas temperature.

Table 3.4. Average collision cross sections (in nm^2) for each buffer

Protein	**$\langle\Omega\rangle_{AA}$**	**$\langle\Omega\rangle_{MA}$**	**$\langle\Omega\rangle_{DA}$**	**$\langle\Omega\rangle_{TA}$**	**$\langle\Omega\rangle_{AA,\ Allen}$**[14]
ubiquitin	10.4 ± 0.96	10.5 ± 1.1	10.8 ± 1.3	10.4 ± 0.94	9.66
α-lactalbumin	13.8 ± 0.54	14.0 ± 1.4	13.8 ± 0.39	13.7 ± 0.42	N/A
pyruvate kinase	99.1 ± 0.17	101 ± 0.29	99.7 ± 0.68	N/A	103
β-galactosidase	167 ± 0.27	166 ± 0.13	166 ± 0.69	168 ± 0.61	166

Figure 3.3A shows the Ω for each charge state of ubiquitin in AA, MA, DA and TA buffers. The relative standard deviation of the average of each Ω in each buffer for ubiquitin is 1.82%, indicating that the Ω for each charge state in each buffer is not changing significantly. Similarly, the relative standard deviations of average Ω of α-lactalbumin, pyruvate kinase and β-galactosidase are 0.73%, 0.98% and 0.72%, respectively. Therefore, the change in average charge state for each protein as a result of changing buffer conditions is not due to a difference in protein conformation.

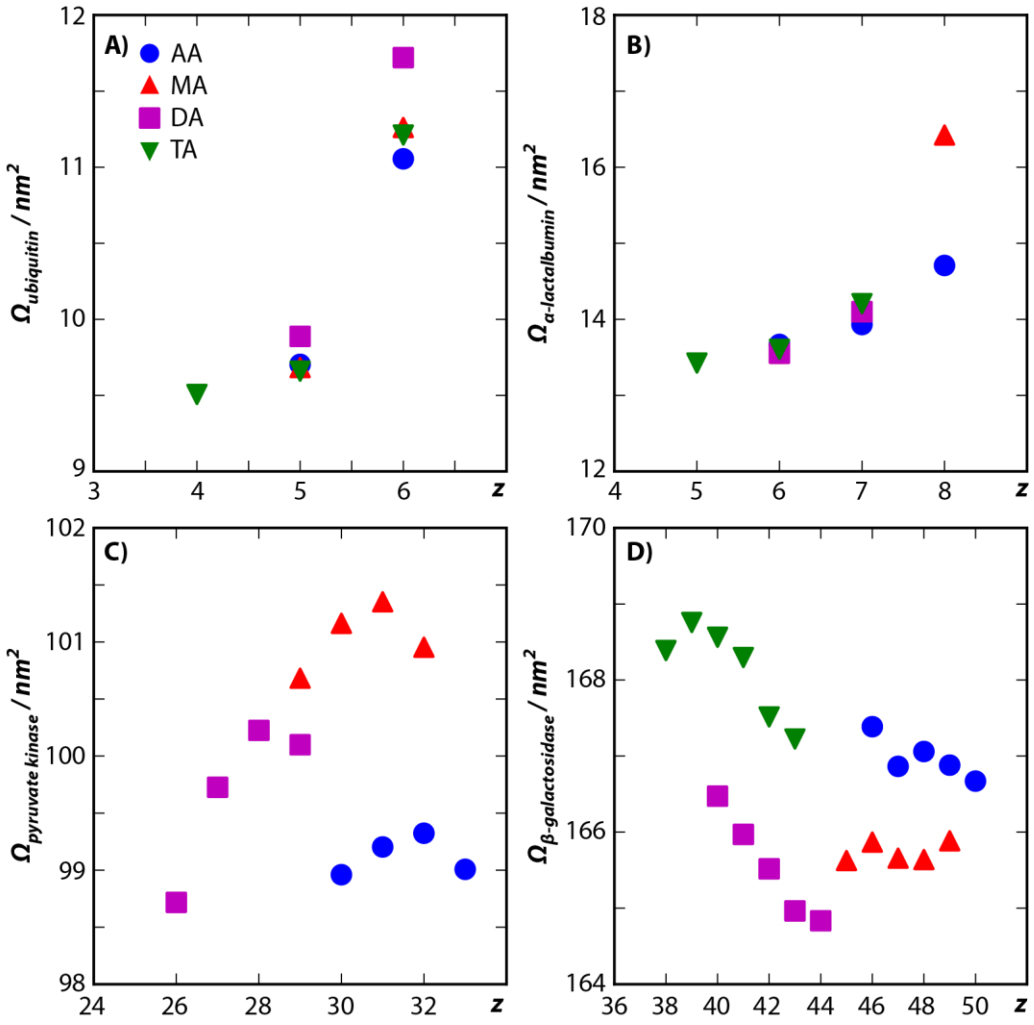

Figure 3.3. The Ω of each charge state of four different proteins in four buffers: ammonium acetate (AA, *blue circles*), methylammonium acetate (MA, *red triangles*), dimethylammonium acetate (DA, *magenta squares*), and trimethylammonium acetate (TA, *green triangles*). The relative standard deviations of the average Ω of (A) ubiquitin (B) α-lactalbumin (C) pyruvate kinase and (D) β-galactosidase are 1.82%, 0.73%, 0.98%, and 0.72%, respectively. Pyruvate kinase in TA data is not included due to low signal-to-noise.

3.4.4 Identification of charge carriers. According to the CCRFEM, charge states are limited by charge carriers in solution and one charge carrier is associated with each E*. Here, the identities of charge carriers present in solution were assumed and their calculated solvation energies were compared to E* values. Free energies for a range of possible charge carriers were calculated using the polarizable continuum model in Gaussian, appropriate basis sets, and dielectric constants for a vacuum ($\varepsilon = 1.0$) or a protein ($\varepsilon = 2.0 – 9.0$). The dielectric constant of a protein is not an exact number and can vary depending on the protein. The solvation energy is the difference between the free energy of the charge carrier in an environment with a greater dielectric constant (*i.e.*, in the presence of a protein) and the free energy of the charge carrier in a vacuum.

Figure 3.4 shows the solvation energies of possible charge carriers for AA buffer in positive ion mode as a function of dielectric constant. E* values determined for AA buffer are also plotted (in kJ/mol) for reference. In positive ion mode, Na^+ is typically present in mass spectra as adducts, and Figure 3.4 shows that the solvation energies of Na^+ as a function of dielectric constant correspond with all three E*. The solvation energies of the other possible charge carriers (NH_4^+, $NH_3NH_4^+$, Na^+H_2O and H_3O^+) also span all three E* with the exception of the solvation energies of diammonium, which only correspond to E_3*. Analyses of the solvation energies of charge carriers potentially present in the other three buffers used in this study (MA, DA, TA) are shown in the Supplemental Information (Figures S3.2 to S3.4) with similar results. This analysis indicates that the identity of the charge carriers is arbitrary and each E* is not necessarily associated with only one charge carrier.

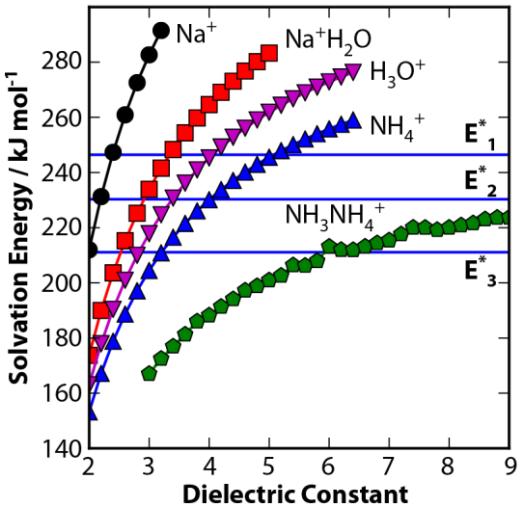

Figure 3.4. The solvation energies of possible charge carriers in ammonium acetate buffer as a function of dielectric constant. Critical field strengths (E*, *horizontal lines*) are shown for reference.

3.5 Conclusions

This work investigates the effects different buffers have on the average charge states of native proteins using nanoelectrospray ionization and native mass spectrometry. The buffers used were ammonium acetate, methylammonium acetate, dimethylammonium acetate, and trimethylammonium acetate; the buffers differ only in their cation, which have decreasing solvation energies. The average charge states of proteins ranging in mass from 8 – 468 kDa decrease with decreasing solvation energy of the buffer cation in positive ion mode (Table 3.1). In negative ion mode, average charge states of the same proteins sprayed from ammonium acetate are less than those in positive ion mode (Table 3.2). A common mechanism used to describe the ionization process is the Charged Residue Model (CRM, Equation 3.1).[9] However, the measured average charge states, in general, are less than those estimated using Equation 3.1

and a surface tension of water (Figure 3.1). These results demonstrate the polarity dependence of protein charge states, which cannot be determined a priori using Equation 3.1.

As an alternative to the CRM, Hogan *et al*. proposed the combined charged residue field emission model (CCRFEM), which states that the charge state of a macromolecule depends on the electric field on the surface of a droplet (E*, Equation 3.2) and the solvation energies of charge carriers present in solution.[12] However, the E* determined here based on measured average charge states of native proteins in ammonium acetate do not match previously measured values using the same method.[12,14] Also, according to the CCRFEM, each E* is associated with one charge carrier but changing only one charge carrier (the cation) does not result in a discrete change of only one E* value (Figure 3.2, Table 3.3). Finally, attempts were made to identify the charge carriers present in solution using computational methods to determine solvation energies and compare those results to E* values (Figure 3.4). The results show that more than one charge carrier could be affecting the average charge states of native proteins. Therefore, neither the CRM nor the CCRFEM fully explains the process of ionization of macromolecules from nanoelectrospray ionization using different buffers.

3.6 Supporting Information. Figures S3.1 to S3.4.

3.7 References

(1) Fenn, J. B.; Mann, M.; Meng, C. K.; Wong, S. F.; Whitehouse, C. M. *Science* **1989**, *246* (4926), 64–71.
(2) Heck, A. J. R.; van den Heuvel, R. H. H. *Mass Spectrom. Rev.* **2004**, *23* (5), 368–389.
(3) Uetrecht, C.; Barbu, I. M.; Shoemaker, G. K.; van Duijn, E.; Heck, A. J. R. *Nat. Chem.* **2011**, *3* (2), 126–132.
(4) Bleiholder, C.; Dupuis, N. F.; Wyttenbach, T.; Bowers, M. T. *Nat. Chem.* **2011**, *3* (2), 172–177.
(5) Smith, R. D.; Loo, J. A.; Edmonds, C. G.; Barinaga, C. J.; Udseth, H. R. *Anal. Chem.* **1990**, *62* (9), 882–899.
(6) Fernandez de la Mora, *J. Anal. Chim. Acta* **2000**, *406* (1), 93–104.
(7) Dole, M.; Mack, L. L.; Hines, R. L.; Mobley, R. C.; Ferguson, L. D.; Alice, M. B. *J. Chem. Phys.* **1968**, *49* (5), 2240–2249.
(8) Konermann, L.; Ahadi, E.; Rodriguez, A. D.; Vahidi, S. *Anal. Chem.* **2013**, *85* (1), 2–9.
(9) Rayleigh, L. *Philos. Mag.* **1882**, *14*, 184–186.
(10) Gomez, A.; Tang, K. *Phys. Fluids* **1994**, *6* (1), 404–414.
(11) Hogan, C. J.; Carroll, J. A.; Rohrs, H. W.; Biswas, P.; Gross, M. L. *J. Am. Chem. Soc.* **2008**, *130* (22), 6926–6927.
(12) Hogan, C. J.; Carroll, J. A.; Rohrs, H. W.; Biswas, P.; Gross, M. L. *Anal. Chem.* **2009**, *81* (1), 369–377.
(13) Kebarle, P.; Peschke, M. *Anal. Chim. Acta* **2000**, *406* (1), 11–35.
(14) Allen, S. J.; Schwartz, A. M.; Bush, M. F. *Anal. Chem.* **2013**, *85* (24), 12055–12061.
(15) Iavarone, A. T.; Jurchen, J. C.; Williams, E. R. *J. Am. Soc. Mass Spectrom.* **2000**, *11* (11), 976–985.
(16) Davidson, K. L.; Oberreit, D. R.; Hogan, C. J.; Bush, M. F. *Int. J. Mass Spectrom.* DOI: 10.1016/j.ijms.2016.09.013.
(17) Allen, S. J.; Bush, M. F. *J. Am. Soc. Mass Spectrom.* **2016**, *27*, 2054–2063.
(18) Allen, S. J.; Giles, K.; Gilbert, T.; Bush, M. F. *Analyst* **2016**, *141* (3), 884–891.
(19) Kaddis, C. S.; Lomeli, S. H.; Yin, S.; Berhane, B.; Apostol, M. I.; Kickhoefer, V. A.; Rome, L. H.; Loo, J. A. *J. Am. Soc. Mass Spectrom.* **2007**, *18* (7), 1206–1216.
(20) Mason, E. A.; McDaniel, E. W. *Transport Properties of Ions in Gases*; Wiley: New York, **1988**.

Chapter 4

Effects of drift gas selection on the ambient-temperature, ion mobility mass spectrometry analysis of amino acids

4.1 Abstract

Ion mobility (IM) separates ions based on their response to an electric field in the presence of a drift gas. Due to its speed and sensitivity, the integration of IM and mass spectrometry (MS) offers many potential advantages for the analysis of small molecules. To determine the effects that drift gas selection has on the information content of IM separations, absolute collision cross sections (Ω) with He, N_2, Ar, CO_2, and N_2O were measured for the 20 common amino acids using low-pressure, ambient-temperature ion mobility experiments performed in a radio-frequency-confining drift cell. The drift gases were selected to span a range of masses, geometries, and polarizabilities. The information content of each separation was quantified using its peak capacity, which depended on factors contributing to widths of peaks as well as the range of Ω relative to the average Ω for the analytes. The selectivity of each separation was quantified by calculating the peak-to-peak resolution for each pair-wise combination of amino acid ions. The number of pairs that were resolved depended strongly on the peak capacity, but the identities of the pairs resolved also depended on the drift gas.

Therefore, results using different drift gases are partially orthogonal and provide complementary chemical information. The temperatures and pressures used for these experiments are similar to those used in many IM-MS instruments, therefore, the outcomes of this research are applicable to optimizing the information content of a wide range of contemporary and future IM-MS experiments.

4.2 Introduction

Ion mobility (IM) mass spectrometry (MS) is a useful technique for the analysis of small molecules due to its speed, sensitivity and selectivity.[1-11] Applications of IM-MS include the separation and characterization of pesticides,[9] petroleum molecules,[3,6] metabolites,[8] phospholipids,[12] peptides,[5,13,14] carbohydrates,[15-17] and therapeutics.[4] Additionally, IM can be used to encode the identity of ions prior to fragmentation (data-independent analysis, DIA),[18-20] which reduces the need to actively isolate specific precursor ions prior to fragmentation (data-dependent analysis). For example, analysis of a cancer-cell lysate analyzed using an IM-DIA workflow identified nearly 50% more proteins than a DIA workflow without IM.[19]

In conventional IM in the low-field limit, ions are separated in a drift gas based on their mobility (K) in a weak electric field (E):

$$K = \frac{L}{t_D E} = \frac{L^2}{t_D V} \tag{4.1}$$

where L is the length of the drift cell, t_D is the observed drift time, and V is the voltage change across the drift cell (the drift voltage). K is inversely proportional to the collision cross section (Ω) of the ion and neutral, according to the Mason-Schamp equation:[21]

$$\Omega = \frac{3ez}{16N}\sqrt{\frac{2\pi}{\mu k_B T}}\frac{1}{K} \tag{4.2}$$

where e is the elementary charge, z is the charge state of the ion, N is the number density of the drift gas, μ is the reduced mass of the ion and neutral, k_B is the Boltzmann constant, and T is the drift-gas temperature.

Peak-to-peak resolution ($R_{p\text{-}p}$) is a quantitative measure of the separation of two peaks in IM and is defined as:

$$R_{p-p} = \frac{t_{D2} - t_{D1}}{0.5(w_2 + w_1)} \tag{4.3}$$

where t_D is the drift time and w is the width at base of each peak. One strategy to increase $R_{p\text{-}p}$ is to decrease w. For a single conformer, w can be estimated using:

$$w^2 = {w_g}^2 + {w_d}^2 = {w_g}^2 + \frac{32 k_B T}{Vez}\left(\frac{L^2}{KV}\right)^2 \tag{4.4}$$

where w_g is the width attributable to gating and w_d is the width attributable to diffusion, as discussed in the Supporting Information.[22,23] Therefore, w can be decreased by decreasing w_g, which may also decrease sensitivity,[23,24] increasing V, which typically requires increasing L in order to decrease the relative contributions from gating and mitigate electrical breakdown,[25,26] or decreasing T in order to minimize contributions from molecular diffusion.[27,28]

An alternative strategy to increase $R_{p\text{-}p}$ is to increase the relative difference in K for the two analytes by using alternative drift gases[1,7,13] or adding chemical modifiers to the buffer gas.[29-31] Hill and coworkers have investigated the effects of drift gas selection on the IM of selected ions using experiments at ambient pressure and elevated temperatures (typically 523 K).[2] Under those conditions, $PheH^+$ and $ArgH^+$ are unresolved in N_2, but are separated in CO_2.[1,2] Remarkably, different gases can even yield different elution orders. For example, chloroaniline is more mobile than iodoaniline in He, whereas iodoaniline is more mobile than chloroaniline in CO_2.[1] Those examples are based on experiments at 523 K, which greatly increases the kinetic energy of ion-neutral collisions and can mask contributions from long-range, ion-neutral

interactions. For instance, the Ω_{N_2} of protonated tetraglycine decreases ~25% when the temperature is increased from 300 to 550 K.[32] Therefore, it is likely that gas-specific effects will be even greater at ambient temperatures than at 523 K.

The objectives of this research are to determine the effects of drift gas selection on the information content and selectivity of ambient-temperature, low-pressure IM-MS measurements of the 20 common amino acids. Five drift gases (He, Ar, N_2, CO_2, and N_2O) were selected for this work based on their range of masses, geometries and polarizabilities. The information content of each separation was quantified by calculating the peak capacity. The selectivity of each separation was quantified by calculating the distribution of $R_{p\text{-}p}$ for each pair-wise combination of amino acid ions. The experiments were performed at low pressure and ambient temperature. Therefore, the outcomes of this research are applicable to optimizing the information content of a wide range of contemporary and future IM-MS experiments using commercial[11,33,34] and laboratory-built[26,28,35-37] IM-MS instruments.

4.3 Methods

All amino acids and chemicals were purchased from Sigma-Aldrich (St. Louis, MO). Amino acids were dissolved in a 47.5/47.5/5% solution of methanol/water/acetic acid to a concentration of 10 to 100 ppm. Protonated ions were generated using electrokinetic nanoelectrospray ionization.[38] IM-MS data were acquired using a modified Waters Synapt G2 HDMS (Wilmslow, United Kingdom) containing an rf-confining drift cell[39] in place of the original traveling-wave ion mobility cell. He, Ar, N_2, CO_2, and N_2O were purchased from Praxair (Table S4.1) and used at the pressures reported in Table 4.1. The cell was operated using potentials reported previously,[39] except some potentials were adjusted when using Ar, CO_2 and

N_2O to improve transmission (Table S4.2). The arrival-time distribution for each protonated amino acid was extracted and analyzed using software developed in the lab.[5] The drift time and width at base (4 standard deviations) were determined from the Gaussian function that has the smallest residual sum of squares with the experimental arrival-time distribution. Ω values were determined from the slopes of plots of drift time versus reciprocal drift voltage.[39]

4.4 Results and Discussion

4.4.1 Determination of collision cross sections (Ω). Arrival-time distributions (ATDs) for the protonated forms of the 20 common amino acids were measured using an rf-confining drift cell,[39] which was operated at ambient temperature (300 K) and while containing low pressures (0.7 to 2.0 Torr) of He, Ar, N_2, CO_2, or N_2O gas. Lower pressures were used for the heaviest drift gases in order to minimize fragmentation during ion injection. The gases were selected to span a wide range of masses, geometries, and polarizabilities[40] (Table 4.1).

Table 4.1. Properties[40] and Pressures of Gases Used in Experiments

Gas	**Mass** Da	**Polarizability** x 10^{-24} cm^3	**Dipole** Debye	***P*** Torr
He	4	0.205	0	2.00
Ar	40	1.641	0	1.20
N_2	28	1.740	0	1.40
CO_2	44	2.911	0	0.70
N_2O	44	3.030	0.166	0.70

ATDs for the protonated forms of 6 selected amino acids (Arg, Leu, Phe, Pro, Thr, and Tyr) in He and N_2O gases are shown in Figures 4.1a and 4.1b, respectively. Measurements were made as a function of the time-averaged electric field of the drift cell, *E*.[39] Under these conditions, drift times measured using an rf-confining drift cell are indistinguishable from those measured using electrostatic drift tubes.[39,41,42] The drift times of each of those 6 selected amino acid ions are

plotted as a function of the ratio of the pressure to the electric field in Figure 4.1c. The mobility, *K*, depends on the slope of the best-fit line (Equation 4.1). *Ω* values were then determined using *K* and Equation 4.2.

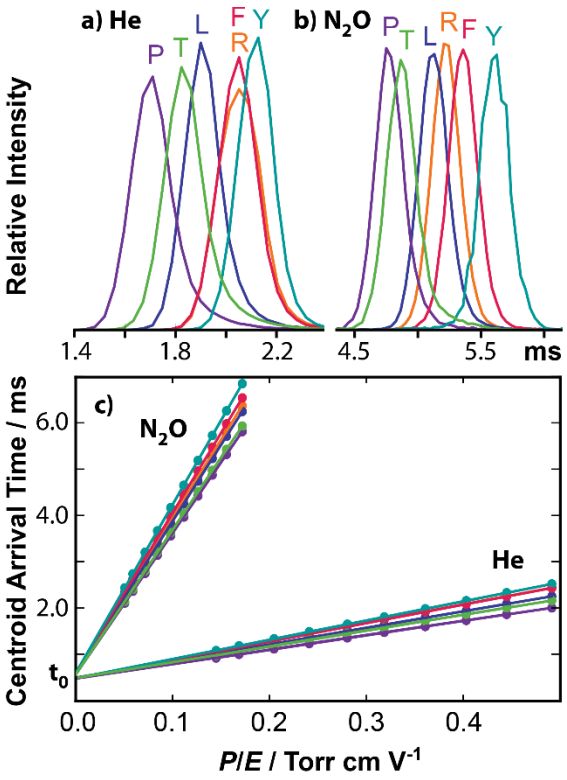

Figure 4.1. Arrival-time distributions of protonated Arg (R), Leu (L), Phe (F), Pro (P), Thr (T), and Tyr (Y) measured using He (a) and N_2O (b) drift gases and a drift voltage of 127 V. (c) The centroid of the arrival-time distributions are plotted as a function of pressure and inverse electric field. R (*orange*) and F (*pink*) have indistinguishable drift times in He, but are separated in N_2O.

The Ω of the protonated forms of each of the 20 common amino acid ions with each gas are reported in Table 4.2 and the average standard deviation for triplicate measurements is 0.40 Å^2. $\Omega_{He,}$ Ω_{Ar}, Ω_{N_2}, Ω_{CO_2}, and Ω_{N_2O} determined using the rf-confining drift cell are plotted in Figure 4.2a. Ω increases with increasing polarizability of the drift gas. Ω_{He} of $GlyH^+$ and $ArgH^+$ of ~42 Å^2 and ~73 Å^2 were determined previously using an electrostatic drift tube operated at ambient temperature.[43] These values differ from those determined here by ~2% and ~3%, respectively, which validates the absolute Ω determined here and are consistent with the absolute accuracy of 3% estimated previously for rf-confining drift cells.[39,41]

Table 4.2. Experimental Ω in Å^2 of protonated amino acids with 5 drift gases.

Amino Acid		**Mass / Da**	Ω_{He}	Ω_{N_2}	Ω_{Ar}	Ω_{CO_2}	Ω_{N_2O}
Glycine	Gly; G	75	43.40	117.4	107.1	190.0	192.1
Alanine	Ala; A	89	48.32	117.1	109.1	189.0	190.6
Serine	Ser; S	105	50.86	121.1	109.9	191.0	192.7
Proline	Pro; P	115	55.56	121.8	113.7	187.5	190.3
Valine	Val; V	117	57.53	124.8	116.1	192.1	194.8
Threonine	Thr; T	119	55.54	123.5	113.6	192.3	194.4
Cysteine	Cys; C	121	54.97	124.6	114.3	193.3	195.5
Isoleucine	Ile; I	131	62.50	129.5	120.5	197.0	199.8
Leucine	Leu; L	131	63.80	130.9	122.1	198.7	201.5
Asparagine	Asn; N	132	58.12	124.7	115.1	194.2	195.9
Aspartic Acid	Asp; D	133	57.15	128.0	115.7	196.8	198.7
Glutamine	Gln; Q	146	62.71	127.0	118.6	195.1	196.5
Lysine	Lys; K	146	64.22	127.6	121.0	190.1	193.4
Glutamic Acid	Glu; E	147	61.67	128.2	118.9	196.9	198.6
Methionine	Met; M	149	64.47	129.4	121.5	196.1	199.1
Histidine	His; H	155	64.55	128.5	120.0	195.1	197.3
Phenylalanine	Phe; F	165	70.43	137.2	127.8	203.3	206.5
Arginine	Arg; R	174	70.27	132.8	125.6	197.0	199.7
Tyrosine	Tyr; Y	181	72.96	141.9	132.5	212.0	214.7
Tryptophan	Trp; W	204	78.97	146.5	138.0	211.8	215.1

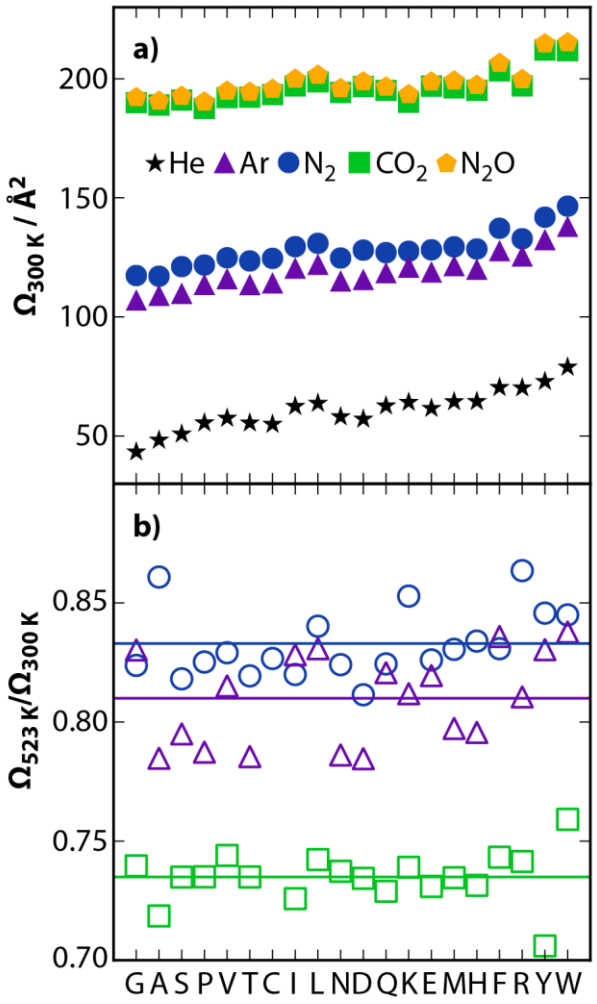

Figure 4.2. a) $\Omega_{300\,K}$ of the protonated forms of the 20 common amino acids (Table 2.2) with He (*black stars*), Ar (*purple triangles*), N_2 (*blue circles*), CO_2 (*green squares*) and N_2O (*yellow pentagons*) in order of increasing amino acid mass. Gases are listed in order of increasing polarizability. b) Ratio of $\Omega_{523\,K}$,[2] which were measured using drift-tube ion mobility at ambient pressure and 523 K, to $\Omega_{300\,K}$ in this work. Horizontal lines represent the average relative Ω for the protonated forms of the common amino acids with each gas.

Ω_{N_2} of the protonated forms of 16 amino acid ions (excluding Gly, Ala, Ser, and Val) were determined previously using traveling-wave ion mobility (TWIM) experiments.[8] Figure S4.1 shows that Ω_{N_2} of higher-mass amino acids (149 to 205 Da) measured using TWIM agree well with Ω_{N_2} measured here using the rf-confining drift cell. However, for the lower-mass species (115 to 147 Da), Ω_{N_2} measured using TWIM are systematically smaller (up to 10%) than those determined here using an rf-confining drift cell. Mobilities in the TWIM experiments were calibrated using poly-DL-alanine peptide ions ($Ala_{3–14}H^+$, which have *m*/*z* values ranging from 232.1 to 1013.5 Da for the monoisotope) whose Ω_{N_2} were determined using an rf-confining drift cell.[41] The differences between the Ω_{N_2} values determined here and those determined by calibrating TWIM drift times are consistent with bias of the latter values caused by extrapolation in the calibration. Despite many validated successes of determining Ω via calibration of TWIM drift times,[4,5] errors resulting from extrapolation have also been reported.[41,44]

The cross sectional areas by Fourier transform ion cyclotron resonance (CRAFTI)[45] method was used recently to determine Ω_{Ar} for the 20 protonated amino acids.[46] Ions in CRAFTI are excited to a large cyclotron radius prior to analysis; therefore, CRAFTI experiments probe ion-neutral collisions with extremely high relative ion-neutral speeds. The linewidth of the Fourier-transformed data is determined as a function of pressure of the gas, and the slope of the linear response is used to determine Ω.[45] Ω determined using CRAFTI are qualitatively correlated with those from high-temperature[46] and these ambient-temperature IM measurements (Figure S4.2), but are quantitatively biased relative to those values. For example, Ω_{Ar} determined using CRAFTI range from 52 to 256 $Å^2$,[46] whereas those in this work range from 107 to 138 $Å^2$ (Table 4.2). The origin of the systematic differences between Ω determined using CRAFTI and those determined using conventional IM is not clear.[46]

4.4.2 Comparison with high-temperature, atmospheric-pressure drift tube measurements. *K* values for the protonated forms of the 20 common amino acid ions with N_2, Ar, and CO_2 were determined using an electrostatic drift tube operated at 523 K.[2] Using Equation 4.2, the reported *K* and *T* values[2] were used to determine Ω values. Those values are systematically smaller than these Ω based on ambient-temperature measurements (Figure S4.3), which is consistent with temperature-dependent IM experiments and the increased relative speeds of ion-neutral collisions at higher temperatures.[32] The ratios of the high-temperature[2] ($\Omega_{523\ K}$) and ambient-temperature ($\Omega_{300\ K}$) Ω with Ar, N_2, and CO_2 gases (Table 4.2) are shown in Figure 4.2b. The average ratios ($\Omega_{523\ K}/\Omega_{300\ K}$) for each of those gases are 0.81, 0.83, and 0.74, respectively. The larger relative difference between $\Omega_{523\ K}$ and $\Omega_{300\ K}$ for CO_2, compared with those differences for Ar and N_2, may be the consequence of stronger long-range, ion-neutral interactions[47] or ion-neutral clustering with CO_2,[48] both of which will preferentially reduce the mobilities of ions at ambient temperature relative to those at elevated temperatures. The differences between $\Omega_{523\ K}$ and $\Omega_{300\ K}$ highlight the effects of temperature on IM measurements, which should be considered when standardizing and interpreting results from those experiments.

4.4.3 Peak capacities. Peak capacity, P_c, is a quantitative measure of the information content available from a separation and is proportional to the range of drift times and inversely proportional to the average peak width:[14,49]

$$P_c = \frac{t_{max} - t_{min}}{0.5(w_{max} + w_{min})} \tag{4.5}$$

where t_{max} and t_{min} are the drift times of the least (protonated tryptophan) and most mobile (protonated glycine) ions and w_{max} and w_{min} are the width at base of those ions, respectively. P_c values determined from the experiments in this study, using a drift voltage of 127 V, are 3.0 (He), 3.8 (Ar), 3.1 (N_2), 2.4 (CO_2), and 2.4 (N_2O).

In order to assess the P_c possible on higher-performance instruments and assess the factors that contribute to P_c, values were estimated for a high-performance drift tube developed at PNNL (Table 4.3).[26] Equations 4.1, 4.2, and 4.4 were substituted into Equation 4.5, first assuming that $w_g = 0$ (see Supporting Information):

$$P_c = \frac{2}{\delta}\frac{(\sqrt{\mu_2}\Omega_2 - \sqrt{\mu_1}\Omega_1)}{(\sqrt{\mu_2}\Omega_2 + \sqrt{\mu_1}\Omega_1)} \tag{4.6}$$

$$\delta = \sqrt{\frac{32k_BT}{Vez}} \tag{4.7}$$

This analysis assumes that each ion adopts a single conformation or an ensemble of conformations that rapidly interconvert, which is consistent with the widths of peaks exhibited in the rf-confining drift cell experiments (see Supporting Information Figure S4.4).

Table 4.3. Instrument Parameters.

	L cm	w_g µs	***V*** V	***E*** V cm^{-1}	***P*** Torr
rf-confining drift cell[39]	25.2	170	127	6.79	Table 1
high-performance drift tube[26]	94	286	1600	17.0	4.0

Based on the Ω in Table 4.2 and the parameters for the high-performance drift tube in Table 4.3 (except assuming that $w_g = 0$), Equation 4.6 yields P_c values of 26.3 (He), 16.4 (Ar), 13.9 (N_2), 11.1 (CO_2), and 11.1 (N_2O), as shown in Figure 4.3a. This analysis shows that for diffusion-limited IM separations, the peak capacity depends most strongly on the range of Ω (Figure 4.3b) relative to the average Ω for the analytes. Therefore, the decrease in peak capacity across this range of gases under these conditions results from the decrease in the range of Ω (Figure 4.3b) and the increase in magnitude of Ω (Figure 4.2a) with increasing polarizability of the neutral.

Interestingly, μ_2 is significantly larger than μ_1 for each gas for these relatively light ions, which increases the P_c of these analyses. For comparison, assuming that $\mu_2 = \mu_1$ = neutral mass (which occurs in the limit of increasing ion mass) would reduce the resulting P_c values to 25.6 (He), 11.1 (Ar), 9.8 (N_2), 5.4 (CO_2), and 5.4 (N_2O).

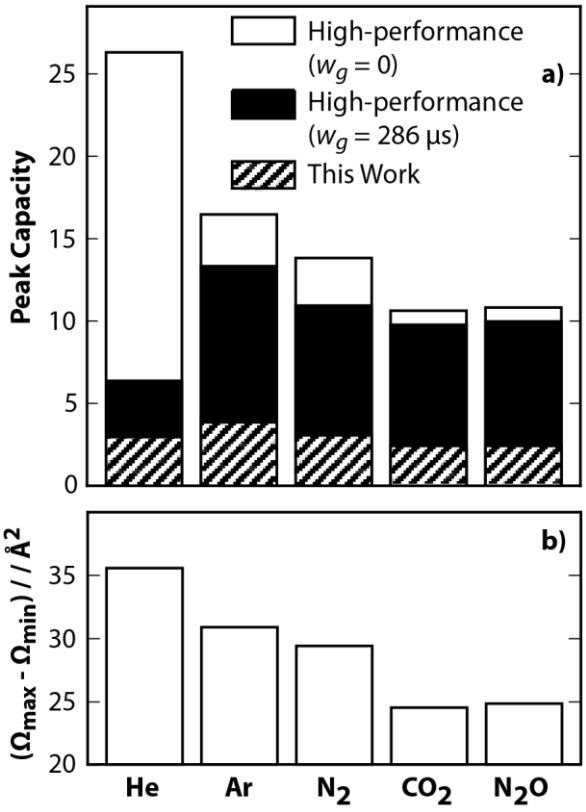

Figure 4.3. a) Peak capacities from these experiments (Equation 4.5) are compared with estimates using parameters for a high-performance drift tube (Table 4.3) without contributions from gating (Equation 4.6) and with contributions from gating (Equation 4.8). b) The range of Ω for the protonated amino acids with each gas.

When $w_g > 0$, substituting Equations 4.1, 4.2, and 4.4 into Equation 4.5 yields (see Supporting Information):

$$P_c = \frac{2\tau(\sqrt{\mu_2}\Omega_2 - \sqrt{\mu_1}\Omega_1)}{\sqrt{w_g{}^2 + \delta^2\tau^2\mu_2{\Omega_2}^2} + \sqrt{w_g{}^2 + \delta^2\tau^2\mu_1{\Omega_1}^2}} \tag{4.8}$$

$$\tau = \frac{16N}{3ez}\sqrt{\frac{k_B T}{2\pi}}\frac{L^2}{V} \tag{4.9}$$

Based on the Ω in Table 4.2 and the parameters for the high-performance drift tube in Table 4.3, Equation 4.8 yields P_c values of 6.2 (He), 13.1 (Ar), 10.8 (N_2), 10.2 (CO_2), and 10.2 (N_2O), as shown in Figure 4.3a. These values are significantly smaller than those estimated without considering contributions from gating (Equation 4.6). Notably, the differences between the values calculated using Equations 4.6 and 4.8 is greatest for He. This is consistent with the relative contributions of gating decreasing with increasing μ (and the concomitant increase in t_D), which is consistent with Equation 4.8.

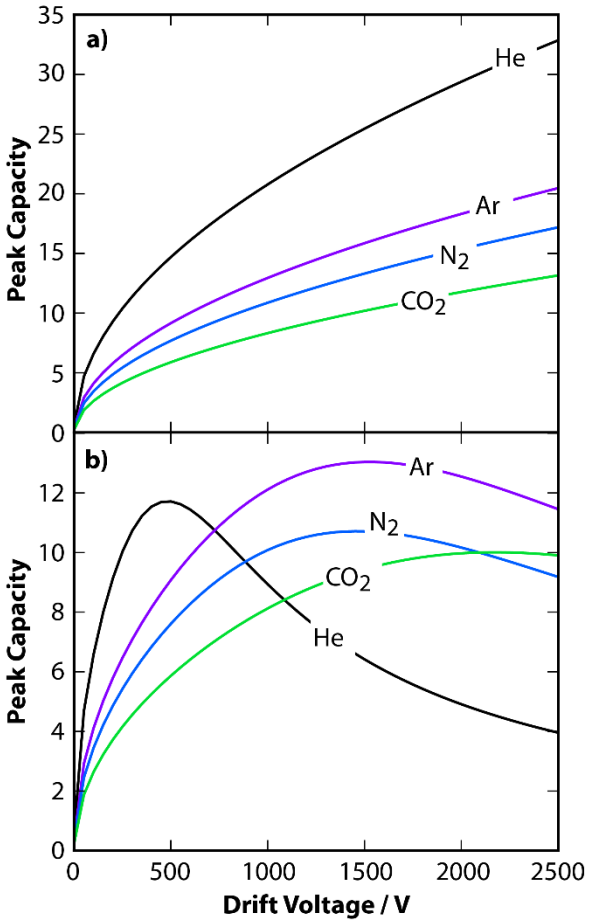

Figure 4.4. (a) P_c values as a function of drift gas and voltage calculated using Equation 4.6, which excludes contributions from gating, and parameters for a high-performance drift tube (Table 4.3). (b) P_c values as a function of drift gas and voltage calculated using Equation 4.8, which includes contributions from gating, and parameters for a high-performance drift tube (Table 4.3). All calculations used the Ω of the least (Trp) and most (Gly) mobile ions in these experiments (Table 4.2). P_c values were also calculated for N_2O, which were very similar to those for CO_2 and not plotted for clarity.

4.4.4 Optimizing P_c. Increasing the drift voltage will decrease the contributions of molecular diffusion to the widths of peaks, but will also increase the relative contributions of ion gating to those widths (Equation 4.4). In order to evaluate the contributions of drift voltage and gas selection to P_c, parameters for the high-performance drift tube (Table 4.3) were used with Equations 4.6 and 4.8 to estimate the P_c of amino acid separations. For separations that are limited only by molecular diffusion (Equation 4.6), P_c increases monotonically with increasing drift voltage (Figure 4.4a). Over all drift voltages, the P_c functions exhibit the order of He > Ar > N_2 > CO_2; this order is correlated with the range of Ω in each gas (Figure 4.3b). For separations that are limited by molecular diffusion and gating (Equation 4.8), the P_c functions exhibit maxima that balance the contributions from the magnitude of the drift times and the two sources of broadening (Figure 4.4b). The voltage that maximizes each P_c function depends on the identity of the gas and the gating time used (Table 4.3): 482 V for He, 1528 V for Ar, 1426 V for N_2, and 2172 V for CO_2. This approach can be used more generally to optimize multiple instrumental parameters, e.g., V, w_g and pressure (N), in order to maximize P_c. However, decreasing w_g will ultimately decrease sensitivity and possible values of V and N will be limited by the performance of the vacuum system and electrical breakdown.

4.4.5 Selectivity. Figures 4.1a and 4.1b show that the separation of $ArgH^+$ and $PheH^+$ improve with increasing polarizability of the drift gas. To quantify this effect for all 190 pair-wise combinations of protonated amino acids in each gas, $R_{p\text{-}p}$ values were calculated using Equation 4.3 as well as the t_D and w determined from each experimental ATD. A histogram of $R_{p\text{-}p}$ values for each pair-wise combination of amino acid drift times in N_2 and cumulative distribution functions (CDF) for each gas are shown in Figure 4.5a. Using a threshold of $R_{p\text{-}p}$ = 1.0, the CDFs show that ~40% of the pair-wise combinations of amino acids were resolved when

He, Ar, or N_2 were used, whereas only ~25% of the pair-wise combinations of amino acids were resolved when CO_2 or N_2O were used (Figure 4.5b). The low fraction determined for the experiments using CO_2 or N_2O are attributed to the lower P_c of those separations, which were exacerbated by the low pressures used for the heaviest drift gases in order to minimize fragmentation during ion injection.

The most pairs of amino acids were resolved in Ar and N_2. However, there are additional differences in the identities of the pairs of amino acids resolved as a function of gas. For example, the shaded regions in Figure 4.5b represent pairs of amino acids that were resolved in that gas that were not resolved in N_2, *i.e.*, complementary chemical information resulting from the partial orthogonality of the measurements. Analogous plots, relative to the pairs resolved in other gases, are shown in Figure S4.5.

In order to assess the selectivity afforded by higher-performance, ion mobility instruments, $R_{p\text{-}p}$ values for each pair-wise combination of amino acids were estimated using the experimental Ω in Table 4.2, the parameters for the high-performance drift tube in Table 4.3, and Equations 4.1 to 4.4. A histogram of $R_{p\text{-}p}$ values for each pair-wise combination of amino acid drift times in N_2 and CDFs for all gases are shown in Supporting Information Figure S4.6. Using a threshold for $R_{p\text{-}p}$ of at least 1.0, the CDFs show that the fraction of resolved amino acids is greatest for Ar (81%) followed by N_2 (78%), N_2O (76%), CO_2 (75%), and then He (72%) (Figure S4.6c). For the high-performance system, eliminating contributions from gating ($w_g = 0$) results in a modest increase in the fraction of resolved pairs of amino acids (Figure S4.7). The greatest increase was for He, which is consistent with the greatest relative contributions from w_g to w for that drift gas (Equation 4.4).

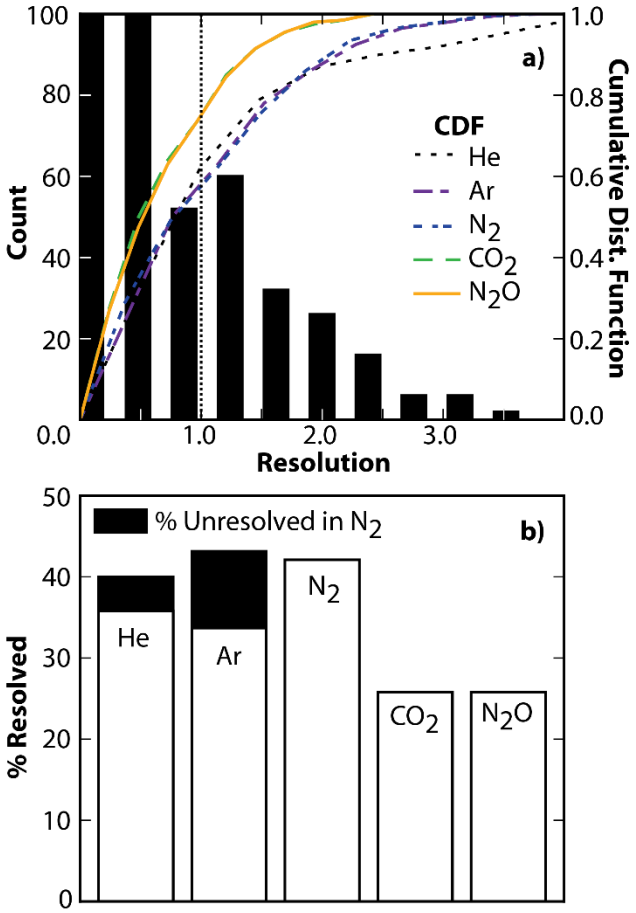

Figure 4.5. (a) A histogram of the peak-to-peak resolution ($R_{p\text{-}p}$, Equation 4.3) calculated for every pair-wise combination of protonated amino acids with N_2 based on these experiments. The vertical dashed line indicates the threshold for resolved amino acids ($\geq$ 1.0). Cumulative distribution functions of the $R_{p\text{-}p}$ calculated for experiments with each drift gas show the relative fraction of resolved amino acids. (b) The fraction of resolved amino acids for each gas listed in order of increasing polarizability. Shaded regions indicate the fraction of complementary pairs identified relative to N_2. Analogous plots based on estimates for a high-performance drift tube (Table 4.3) are shown in Figures S4.6 and S4.7.

The results in this section quantify the selectivity afforded by each drift gas for this analysis. The unique pairs of analytes resolved using a given drift gas illustrate the potential of selecting a drift gas to resolve a set of target analytes, relative to only maximizing the peak capacity. The degree of orthogonality between each analysis can be used to guide the selection of drift gases during the development of future ion mobility methods.

4.5 Conclusions

An rf-confining drift cell was used to measure the Ω of the protonated forms of the 20 common amino acids with He, Ar, N_2, CO_2, and N_2O under low-pressure, ambient-temperature conditions (Figure 4.2), similar to those used in most commercial IM-MS instruments.[11,33,34] The Ω increase with the increasing polarizability of the drift gas, and are systematically larger than those reported previously by Hill and coworkers based on measurements at 523 K.[2] The differences in Ω_{CO_2} and Ω_{N_2O} are extremely small. This result is surprising because ions should have stronger long-range interactions with N_2O (given its permanent dipole moment) than CO_2, which would be expected to result in smaller K and larger Ω. Given that N_2O is more expensive and hazardous than CO_2, these results suggest that there is no advantage to using N_2O instead of CO_2 in ion mobility spectrometry other than the higher electrical breakdown voltage for N_2O.[50]

Based on the ambient-temperature Ω (Table 4.2) and Equation 4.8, the effect of drift-gas selection on peak capacity (P_c, Figure 4.3) was evaluated for this rf-confining drift cell and a high-performance drift tube (Table 4.3). P_c depends on factors contributing to the widths of peaks (Equation 4.4) and the range of Ω relative to the average Ω for the analytes, which decreases with the increasing polarizability of the gas (Figures 4.2a and 4.3b). The selectivity of each separation was quantified by calculating the peak-to-peak resolution for each pair-wise

combination of amino acid ions (Figure 4.5a). The number of pairs that were resolved depended strongly on P_c, but the identities of the pairs resolved also depended on the drift gas (Figure 4.5b). The unique pairs of protonated amino acids resolved in a given drift gas illustrate the potential of selecting a drift gas to separate specific analytes, relative to only maximizing the peak capacity of the separation.

More generally, the outcomes of this research can be used to increase the information content of a wide range of contemporary and future IM-MS experiments. The experimentally determined Ω will be useful for calibration and benchmarking the accuracy of theoretical methods for calculating Ω. This is particularly critical for Ω with Ar, CO_2, N_2O, for which there are relatively few direct measurements of Ω under low-pressure, ambient-temperature conditions.[9,51] Equation 4.8 can be used to estimate P_c, which can in turn be used to optimize parameters for experiments, such as drift-gas identity, drift-gas pressure, and drift voltage. For example, Figure 4.4b shows that for a specific high-performance instrument, the drift voltage that maximizes P_c depends strongly on the drift-gas selected. This equation will also be useful in the design of new instruments: rapid estimates of P_c will help quantify the relative benefits of specific design decisions, such as the gating time, the length of the drift region, and the temperature of the separation.

4.6 Acknowledgements. The authors thank Prof. Robert E. Synovec and Mr. Samuel J. Allen for useful discussion. Acknowledgment is made to the Donors of the American Chemical Society Petroleum Research Fund, the Alfred P. Sloan Foundation (Fellowship to M. F. B.), and Eli Lilly and Company (Young Investigator Award in Analytical Chemistry to M. F. B.) for support of this research.

4.7 Supporting Information: Derivation and discussion of selected equations, Tables S4.1 to S4.2, and Figures S4.1 to S4.7.

4.8 References

(1) Asbury, G. R.; Hill, H. H. *Anal. Chem*. **2000**, *72*, 580–584.
(2) Beegle, L. W.; Kanik, I.; Matz, L.; Hill, H. H. *Anal. Chem*. **2001**, *73*, 3028–3034.
(3) Ahmed, A.; Cho, Y. J.; No, M.; Koh, J.; Tomczyk, N.; Giles, K.; Yoo, J. S.; Kim, S. *Anal. Chem.* **2011**, *83*, 77–83.
(4) Campuzano, I.; Bush, M. F.; Robinson, C. V.; Beaumont, C.; Richardson, K.; Kim, H.; Kim, H. I. *Anal. Chem*. **2012**, *84*, 1026–1033.
(5) Bush, M. F.; Campuzano, I. D. G.; Robinson, C. V. *Anal. Chem*. **2012**, *84*, 7124–7130.
(6) Ponthus, J.; Riches, E. Int. *J. Ion Mobil. Spectrom*. **2013**, *16*, 95–103.
(7) Lalli, P. M.; Corilo, Y. E.; Fasciotti, M.; Riccio, M. F.; de Sa, G. F.; Daroda, R. J.; Souza, G. H. M. F.; McCullagh, M.; Bartberger, M. D.; Eberlin, M. N.; Campuzano, I. D. G. *J. Mass Spectrom*. **2013**, *48*, 989–997.
(8) Paglia, G.; Williams, J. P.; Menikarachchi, L.; Thompson, J. W.; Tyldesley-Worster, R.; Halldórsson, S.; Rolfsson, O.; Moseley, A.; Grant, D.; Langridge, J.; Palsson, B. O.; Astarita, G. *Anal. Chem*. **2014**, *86*, 3985–3993.
(9) Kurulugama, R. T.; Darland, E.; Kuhlmann, F.; Stafford, G.; Fjeldsted, J. *Analyst* **2015**, *140*, 6834–6844.
(10) Larriba-Andaluz, C.; Fernández-García, J.; Ewing, M. A.; Hogan, C. J.; Clemmer, D. E. *Phys. Chem. Chem. Phys*. **2015**, *17*, 15019–15029.
(11) May, J. C.; Dodds, J. N.; Kurulugama, R. T.; Stafford, G. C.; Fjeldsted, J. C.; McLean, J. A. *Analyst* **2015**, *140*, 6824–6833.
(12) Hines, K. M.; May, J. C.; McLean, J. A.; Xu, L. *Anal. Chem*. **2016**, *88*, 7329–7336.
(13) Beegle, L. W.; Kanik, I.; Matz, L.; Hill, H. H., Jr. *Int. J. Mass Spectrom*. **2002**, *216*, 257–268.
(14) Ruotolo, B. T.; McLean, J. A.; Gillig, K. J.; Russell, D. H. *J. Mass Spectrom*. **2004**, *39*, 361–367.
(15) Dwivedi, P.; Bendiak, B.; Clowers, B. H.; Hill, H. H. *J. Am. Soc. Mass Spectrom*. **2007**, *18*, 1163–1175.
(16) Hofmann, J.; Hahm, H. S.; Seeberger, P. H.; Pagel, K. *Nature* **2015**, *526*, 241–244.
(17) Huang, Y.; Dodds, E. D. *Anal. Chem*. **2015**, *87*, 5664–5668.
(18) Lee, S.; Li, Z.; Valentine, S. J.; Zucker, S. M.; Webber, N.; Reilly, J. P.; Clemmer, D. E. *Int. J. Mass Spectrom*. **2012**, *309*, 154–160.
(19) Geromanos, S. J.; Hughes, C.; Ciavarini, S.; Vissers, J. P. C.; Langridge, J. I. *Anal. Bioanal. Chem*. **2012**, *404*, 1127–1139.
(20) Distler, U.; Kuharev, J.; Navarro, P.; Levin, Y.; Schild, H.; Tenzer, S. *Nat. Methods* **2014**, *11*, 167–170.
(21) Mason, E. A.; McDaniel, E. W. *Transport Properties of Ions in Gases*; Wiley: New York, **1988**.
(22) Revercomb, H. E.; Mason, E. A. *Anal. Chem*. **1975**, *47*, 970–983.
(23) Kanu, A. B.; Gribb, M. M.; Hill, H. H. *Anal. Chem*. **2008**, *80*, 6610–6619.
(24) Ibrahim, Y. M.; Garimella, S. V. B.; Tolmachev, A. V.; Baker, E. S.; Smith, R. D. *Anal. Chem*. **2014**, *86*, 5295–5299.
(25) Baker, E. S.; Clowers, B. H.; Li, F.; Tang, K.; Tolmachev, A. V.; Prior, D. C.; Belov, M. E.; Smith, R. D. *J. Am. Soc. Mass Spectrom*. **2007**, *18*, 1176–1187.

(26) Ibrahim, Y. M.; Baker, E. S.; Danielson, W. F.; Norheim, R. V.; Prior, D. C.; Anderson, G. A.; Belov, M. E.; Smith, R. D. *Int. J. Mass Spectrom*. **2015**, *377*, 655–662.
(27) May, J. C.; Russell, D. H. *J. Am. Soc. Mass Spectrom*. **2011**, *22*, 1134–1145.
(28) Ujma, J.; Giles, K.; Morris, M.; Barran, P. E. *Anal. Chem*. **2016**, *88*, 9469–9478.
(29) Fernandez-Maestre, R.; Meza-Morelos, D.; Hill, H. H. *Int. J. Mass Spectrom*. **2015**, *380*, 21–25.
(30) Rawat, V. K.; Vidal-de-Miguel, G.; Hogan, C. J. *Analyst* **2015**, *140*, 6945–6954.
(31) Meyer, N. A.; Root, K.; Zenobi, R.; Vidal-de-Miguel, G. *Anal. Chem*. **2016**, *88*, 2033–2040.
(32) Bleiholder, C.; Johnson, N. R.; Contreras, S.; Wyttenbach, T.; Bowers, M. T. *Anal. Chem*. **2015**, *87*, 7196–7203.
(33) Giles, K.; Williams, J. P.; Campuzano, I. *Rapid Commun. Mass Spectrom*. **2011**, *25*, 1559–1566.
(34) Silveira, J. A.; Ridgeway, M. E.; Park, M. A. *Anal. Chem*. **2014**, *86*, 5624–5627.
(35) Merenbloom, S. I.; Koeniger, S. L.; Valentine, S. J.; Plasencia, M. D.; Clemmer, D. E. *Anal. Chem*. **2006**, *78*, 2802–2809.
(36) Kemper, P. R.; Dupuis, N. F.; Bowers, M. T. *Int. J. Mass Spectrom*. **2009**, *287*, 46–57.
(37) Allen, S. J.; Eaton, R. M.; Bush, M. F. *Anal. Chem*. **2016**, *88*, 9118–9126.
(38) Davidson, K. L.; Oberreit, D. R.; Hogan, C. J.; Bush, M. F. *Int. J. Mass Spectrom*. DOI: 10.1016/j.ijms.2016.09.013.
(39) Allen, S. J.; Giles, K.; Gilbert, T.; Bush, M. F. *Analyst* **2016**, *141*, 884–891.
(40) Lide, D. R., Ed. *CRC Handbook of Chemistry and Physics, 96th ed*.; CRC Press: Boca Raton, FL, **2015**.
(41) Bush, M. F.; Hall, Z.; Giles, K.; Hoyes, J.; Robinson, C. V.; Ruotolo, B. T. *Anal. Chem*. **2010**, *82*, 9557–9565.
(42) Allen, S. J.; Bush, M. F. *J. Am. Soc. Mass Spectrom*. **2016**, *27*, 2054–2063.
(43) Wyttenbach, T.; Witt, M.; Bowers, M. T. *Int. J. Mass Spectrom*. **1999**, *182–183*, 243–252.
(44) Salbo, R.; Bush, M. F.; Naver, H.; Campuzano, I.; Robinson, C. V.; Pettersson, I.; Jørgensen, T. J. D.; Haselmann, K. F. *Rapid Commun. Mass Spectrom*. **2012**, *26*, 1181–1193.
(45) Yang, F.; Voelkel, J. E.; Dearden, D. V. *Anal. Chem*. **2012**, *84*, 4851–4857.
(46) Anupriya; Jones, C. A.; Dearden, D. V. *J. Am. Soc. Mass Spectrom*. **2016**, *27*, 1366–1375.
(47) Johnson, P. V.; Kim, H. I.; Beegle, L. W.; Kanik, I. *J. Phys. Chem. A* **2004**, *108*, 5785–5792.
(48) Berant, Z.; Karpas, Z.; Shahal, O. *J. Phys. Chem*. **1989**, *93*, 7529–7532.
(49) Ruotolo, B. T.; Gillig, K. J.; Stone, E. G.; Russell, D. H. *J. Chromatogr. B Analyt. Technol. Biomed. Life. Sci*. **2002**, *782*, 385–392.
(50) Akbar, M.; Malik, N. H. IEEE *Trans. Electr. Insul*. **1985**, *EI-20*, 581–585.
(51) Jurneczko, E.; Kalapothakis, J.; Campuzano, I. D. G.; Morris, M.; Barran, P. E. *Anal. Chem*. **2012**, *84*, 8524–8531.

Chapter 5

Effects of Drift Gas Selection on the Ion Mobility of Protonated Quinoline and Its Analogues

5.1 Abstract

Ion mobility spectrometry has recently become an important tool in the field of petroleomics to separate and identify a wider range of molecules in petroleum crude oil. One challenge in petroleomics is the similarity in the size and shape of molecules that have the same mass-to-charge (*m*/*z*) ratio. Here we use four different drift gases (He, Ar, N_2, and CO_2) in combination with ion mobility spectrometry to characterize the separation of a series of double-bond equivalents, which are representative of compounds typically found in petroleum. We find that separation of compounds with the same *m*/*z* improves when larger, more polarizable drift gases are used. We also explore the origin of the orthogonality between ion mobility and *m*/*z* by using different methods to calculate the collision cross section of each compound.

5.2 Introduction

Petroleomics[1–4] is the study and characterization of the compounds present in crude oil. Separation and identification of petroleum compounds is challenging because they often have similar molecular compositions containing primarily carbon, hydrogen, nitrogen, oxygen, and sulfur ($C_cH_hN_nO_oS_s$). Petroleum samples have grown even more complex in recent years with the increased use of unconventional crude oils[5] that contain heavier components, higher sulfur content, and greater acidity. Distinguishing different types of oil samples is important for determining their origin or their uses. For example, samples of shale oil, which could serve as a

replacement for conventional oil in future, exhibited differences in the most abundant double bond equivalent species compared with conventional oil and was found to be a less biodegraded oil.[6]

Fourier transform ion cyclotron resonance mass spectrometry (FT-ICR MS), which is a high-resolution and high-mass accuracy analyzer, is capable of resolving thousands of petroleum compounds on the basis of their elemental composition.[7–13] For example, negative-ion electrospray ionization (ESI) FT-ICR MS resolved ~10,000 compositionally distinct compounds in an acidic asphaltene fraction of Illinois No. 6 coal.[7] Positive-ion ESI FT-ICR MS analysis of a European crude oil resolved and identified ~8,000 compounds.[1] Additionally, 16,858 mass spectral peaks of a heavy vacuum gas oil were resolved using positive-ion atmospheric pressure photoionization (APPI) FT-ICR MS.[14] However, FT-ICR MS alone is not capable of differentiating molecules with the same elemental composition but different structures. Gas chromatography (GC) is often used to separate petroleum molecules prior to mass analysis, but GC is limited to lighter distillates and requires additional preparation to reduce complexity of the sample.[14]

In drift tube ion mobility (IM), ions are separated based on their mobility (K) in a weak electric field (E):

$$K = \frac{L}{t_D E} = \frac{L^2}{t_D V} \tag{5.1}$$

where t_D is the drift time of the ion, V is the voltage change across the drift cell (the drift voltage), and L is the length of the drift cell. In the limit of low E,[15] K is inversely proportional to the collision cross section (Ω) of the ion and gas molecule:[16]

$$\Omega = \frac{3ez}{16N}\sqrt{\frac{2\pi}{\mu k_B T}}\frac{1}{K} \tag{5.2}$$

where e is the elementary charge, z is the charge state of the ion, N is the drift-gas number density, μ is the reduced mass of the ion and drift gas, k_B is the Boltzmann constant and T is the drift-gas temperature. Ion mobility mass spectrometry (IMMS)[2–4,10] can be used to separate and characterize isomeric compounds, which is an advantage in petroleomics. For example, leucine, isoleucine, and their isomers all have the chemical formula $C_6H_{13}NO_2$, and therefore, the singly protonated ions of these biomolecules cannot be separated on the basis of m/z alone. McLean and coworkers found that pair-wise combinations of constitutional isomers (*e.g.* L-leucine and L-isoleucine) had Ω with N_2 that differed by 0.3 to 6.9%.[17] They then determined the resolving power required to separate a pair of ions, based on the percent difference in Ω and a selected peak-to-peak resolution ($R_{p\text{-}p}$):

$$R_{p-p} = \frac{t_{D2} - t_{D2}}{0.5(w_2 + w_1)} \tag{5.3}$$

where w is the width at base of each peak.

One strategy to increase $R_{p\text{-}p}$ is to minimize the w, which can be estimated from:

$$w^2 = {w_g}^2 + {w_d}^2 = {w_g}^2 + \frac{32 k_B T}{Vez}\left(\frac{L^2}{KV}\right)^2 \tag{5.4}$$

where w_g is the width attributable to gating and w_d is the width attributable to diffusion.[18,19] $R_{p\text{-}p}$ can be maximized by decreasing w in the following ways: decreasing w_g, which may also decrease sensitivity,[19,20] increasing V, which can cause electrical breakdown and therefore typically requires increasing L,[21,22] or decreasing T in order to mitigate contributions from diffusion of ions.[23,24] Recently, efforts have been made to increase L using a 13-meter path length Structures for Lossless Ion Manipulations (SLIM) module, which demonstrated 5-fold higher resolution separations than commercially available instruments.[25] Alternatively, $R_{p\text{-}p}$ can be increased by increasing the relative difference in t_D (*i.e.*, K) between two analytes by using alternative drift gases[26–28] or adding chemical modifiers to the buffer gas.[29–31] For example, a

crude oil sample was analyzed without any pretreatment using traveling-wave ion mobility mass spectrometry (TWIM-MS) with N_2 and CO_2 drift gases.[4] Two classes of compounds were uncovered; one class containing O_2 and the other containing N. The two classes were better resolved from each other using CO_2 gas, which is more massive and polarizable than N_2.[4]

The objectives of this research are to determine the effects of different drift gases on the separation of aromatic compounds quinoline, isoquinoline, and selected double-bond equivalents (DBE). Four drift gases (He, Ar, N_2, and CO_2) were selected for this work based on their range of masses, geometries and polarizabilities. The selectivity of each separation was quantified by calculating $R_{p\text{-}p}$ for each pair of a given DBE. The information content of each separation was quantified by calculating the peak capacity. Finally, the origin of drift gas orthogonality was investigated using the projection approximation,[32] exact hard spheres scattering method,[33,34] and trajectory method as implemented in MOBCAL.[35]

5.3 Methods

5.3.1 Ion Mobility Mass Spectrometry Experiments. All chemicals used in this study were purchased from Sigma-Aldrich (St. Louis, MO), except 5,6,7,8-tetrahydroquinoline was purchased from Acros Organics (Geel, Belgium), and dissolved in a 47.5/47.5/5% solution of methanol/water/acetic acid to concentrations of 10 to 100 ppm. Protonated ions were generated using electrokinetic nanoelectrospray ionization.[36] Ion mobility mass spectrometry data were acquired using a modified Waters Synapt G2 HDMS (Wilmslow, United Kingdom) containing a radio-frequency confining drift cell[37] in place of the original traveling-wave ion mobility cell. He, Ar, N_2, and CO_2 were used as drift gases as purchased from Praxair (Table S5.1) and at pressures reported in Table 5.1. Arrival-time distributions were measured for drift voltages ranging from 100 to 350 V. Some voltages were changed when using Ar and CO_2 to mitigate

fragmentation, but the drift voltages were the same for all gases used (Table S5.2). The arrival-time distribution for each amino acid was extracted and analyzed using software developed in the lab to determine t_D values.[38] *K* values were determined from the slopes of plots of drift time versus reciprocal drift voltages[37] and used to determine Ω values using Equation 5.2.

Table 5.1. Mass, dipole moments, polarizabilities, and pressures of gases used.[44]

Gas	**Mass** Da	**Polarizability** x 10^{-24} cm^3	**Dipole Moment** Debye	**Pressure** Torr
He	4	0.205	0	2.00
Ar	40	1.641	0	1.20
N_2	28	1.740	0	1.40
CO_2	44	2.911	0	0.70

5.3.2 Theoretical Calculations. The lowest-energy configuration and dipole moment of each protonated ion was determined using Gaussian (Wallingford, CT),[39] B3LYP density functional theory, and the 6-311+G(d,p) basis set. The optimized geometries were used in MOBCAL[35] to calculate the collision cross section of each ion with He and N_2. Optimized atomic radii of H, C, N and O were determined using a basin hopping algorithm and the projection approximation[32] and exact hard spheres scattering methods.[33,34]

5.4 Results and Discussion

5.4.1 Collision Cross Section Measurements. Structures and abbreviations for the protonated ions of quinoline (Q7), isoquinoline (iQ7), and eight analogues with fewer double bond equivalents selected for this research are shown in Figure 5.1. Arrival-time distributions were measured using an rf-confining drift cell[37] while containing low pressures of either He, Ar, N_2, or CO_2 gas. These four drift gases span a range of masses and polarizabilities (Table 5.1). Figures 5.2a and 5.2b show arrival-time distribuitons of Q5a, iQ5a, Q5b, and iQ5b with He and

CO_2, respectively. The distributions for the four protonated ions are indistinguishable with He, but are different with CO_2. Drift times (t_D), which were determined from the Gaussian distribution that has the smallest residual sum of squares with the experimental distribution, were measured as a function of the drift field, E. Measured t_D are plotted as a function of reciprocal drift voltage in Figure 5.2c. The slope of the best-fit line is inversely proportional to the mobility, K, according to Equation 5.1. The Ω value for each ion with each gas was then determined using K and Equation 5.2.

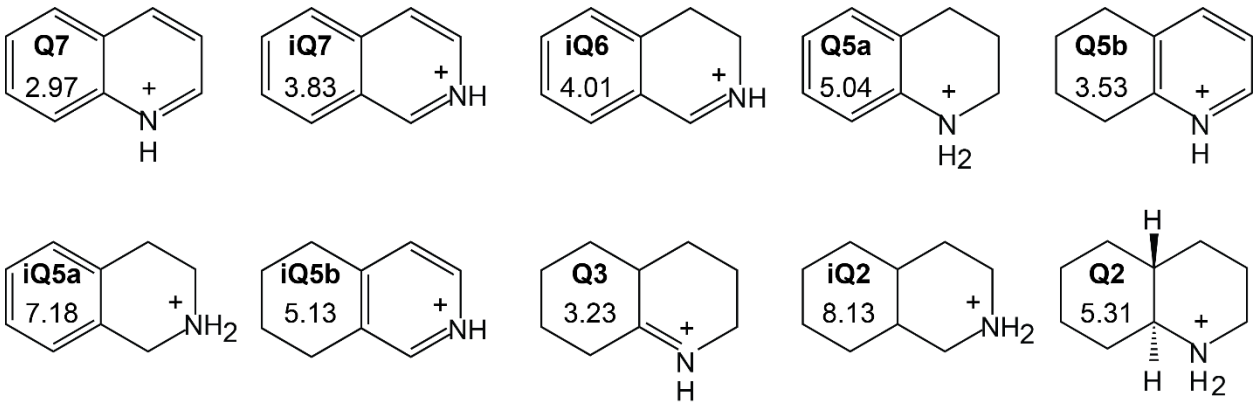

Figure 5.1. Abbreviations (in bold), dipole moments in Debye, and structures of protonated quinoline (Q7), isoquinoline (iQ7), 3,4-dihydroisoquinoline (iQ6), 1,2,3,4-tetrahydroquinoline (Q5a), 5,6,7,8-tetrahydroquinoline (Q5b), 1,2,3,4-tetrahydroisoquinoline (iQ5a), 5,6,7,8-tetrahydroisoquinoline (iQ5b), 2,3,4,4A,5,6,7,8-octahydroquinoline (Q3), perhydroisoquinoline (iQ2), and *trans*-decahydroquinoline (Q2). The number in the abbreviation is the number of double-bond equivalents in the structure.

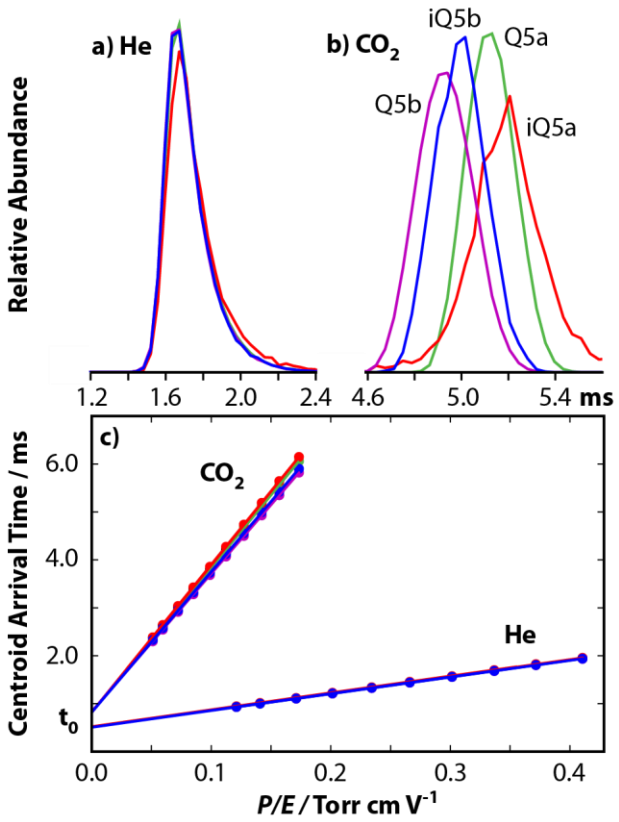

Figure 5.2. Arrival-time distributions of Q5a, iQ5a, Q5b, and iQ5b measured using (a) He and (b) CO_2 drift gases and a drift voltage of 127 V. (c) The centroid of the arrival-time distributions plotted as a function of pressure and inverse drift voltage.

The measured Ω_{He}, Ω_{Ar}, Ω_{N_2}, and Ω_{CO_2} values for all ions are reported in Table 5.2 and plotted as a function of *m*/*z* in Figure 5.3. The averages of the Ω_{He}, Ω_{Ar}, Ω_{N_2}, and Ω_{CO_2} values are 63.5, 118.7, 124.2, and 182.5 Å^2, respectively, and increase with drift gas polarizability. The squares of the correlation coefficients (r^2) between *m*/*z* and Ω_{He}, Ω_{Ar}, Ω_{N_2}, and Ω_{CO_2} are 0.98, 0.86, 0.69, and 0.35. That is, the Ω_{He} values are essentially linear with respect to *m*/*z* and scatter about the best-fit line is small (Figure 5.3a), whereas the Ω_{CO_2} are poorly correlated with *m*/*z* (Figure 5.3d).

Table 5.2. Experimental Ω in Å^2 with four different drift gases.

Abbrev.	$\boldsymbol{\Omega_{He}}$	$\boldsymbol{\Omega_{Ar}}$	$\boldsymbol{\Omega_{N_2}}$	$\boldsymbol{\Omega_{CO_2}}$
Q7	60.38	112.3	117.5	175.3
iQ7	59.76	113.3	119.3	176.9
iQ6	61.84	115.5	121.3	179.3
Q5a	63.52	120.1	126.3	187.1
iQ5a	63.51	121.0	128.4	191.6
Q5b	63.22	117.2	121.9	178.4
iQ5b	62.98	118.3	123.7	181.4
Q3	65.92	120.7	124.3	179.6
iQ2	67.16	125.8	131.1	190.1
Q2	66.66	123.1	128.3	185.7

5.4.2 Origin of Orthogonality. Differences in Ω values between different gases have been attributed to a range of factors, including the polarizability of the drift gas;[26,28] selectivity between different drift gases is most often attributed to the polarizability of the drift gas and/or the dipole moment of the ion.[28,40]

The dipole moment of each ion, however, is not correlated with Ω. For example, iQ5a has a smaller dipole moment (Figure 5.1) and Ω than iQ2 with He, Ar, and N_2, (Figures 5.3a-c, respectively), however, iQ5a has a larger Ω_{CO_2} than iQ2 despite its smaller dipole moment

(Figure 5.3d). Additionally, the identity of the least and most mobile ions depends on the gas used (Figure 5.4b). For instance, iQ7 and iQ2 are the most and least mobile ions in He while Q7 and iQ5a are the most and least mobile ions in CO_2. These, and other examples, show that the relative dipole moment of each ion does not predictively account for the relative differences in Ω.

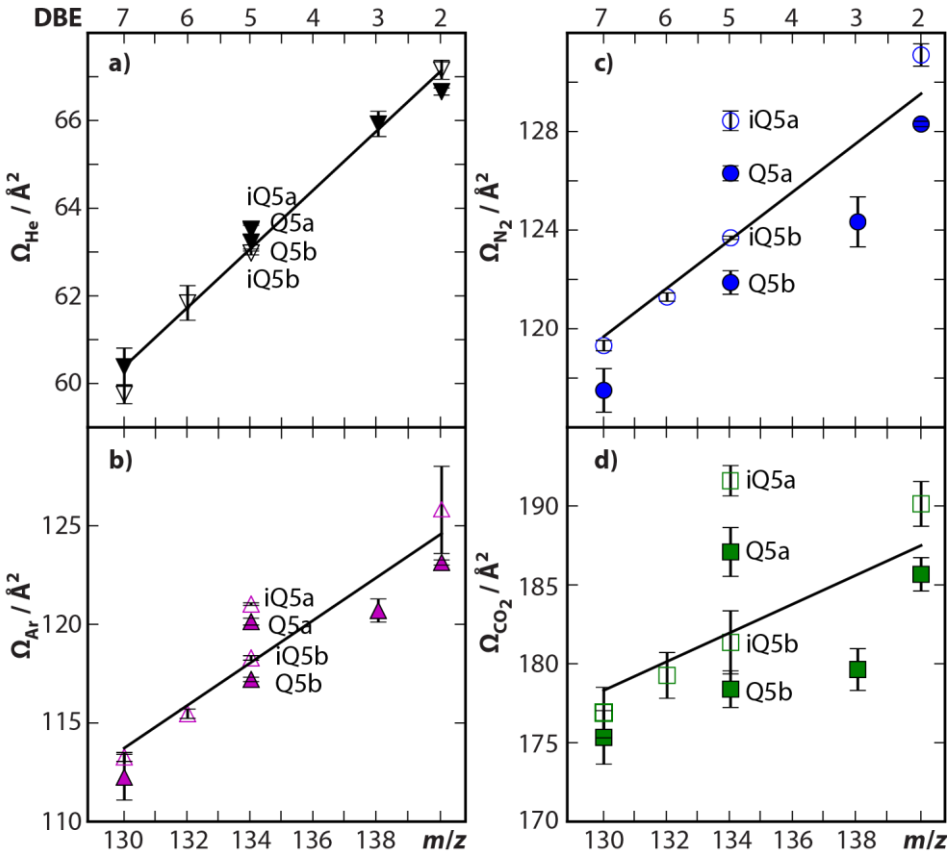

Figure 5.3. The Ω of 10 protonated compounds (Figure 5.1) as a function of *m*/*z* with (a) He, (b) Ar, (c) N_2, and (d) CO_2. Hollow markers identify iQ7 and its analogues while solid markers identify Q7 and its analogues. DBE values are shown on top x-axis. Bars span the 95% confidence interval determined from 3 technical replicates and t-statistics.

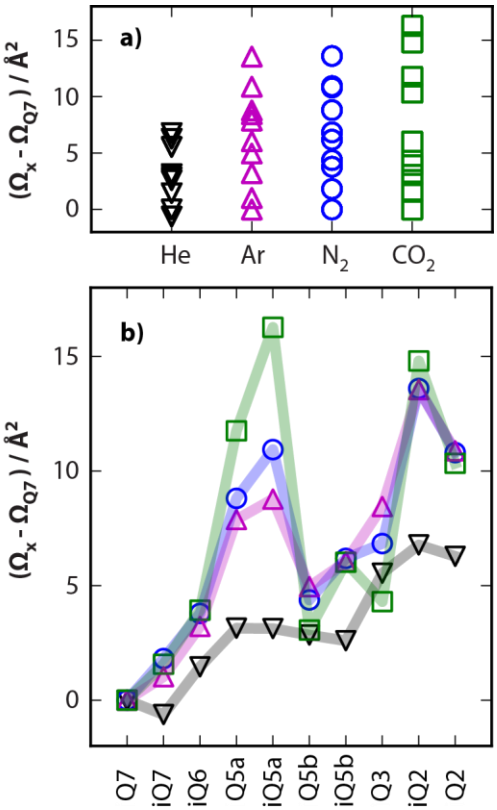

Figure 5.4. (a) The difference in Ω between each compound and Q7 for He (*black triangles*), Ar (*purple triangles*), N_2 (*blue circles*) and CO_2 (*green squares*). The range of Ω increases with polarizability of the gas (Table 5.1). (b) The difference in Ω between each compound and Q7 with each gas shown as a function of the compound.

If the Ω of an ion with a drift gas molecule is only due to hard sphere interactions, then Q5a, iQ5a, Q5b, and iQ5b should have similar Ω with a particular drift gas. However, their Ω begin to differ when the polarizability of the gas increases. Previously, Hill *et al.* measured the Ω of glycine polypeptides in He, Ar, N_2, and CO_2 and found that the radius of an ion increases linearly with drift gas polarizability.[26] Ω of iQ6, Q5a, iQ5a, Q5b, iQ5b, and Q3 were similarly converted to a radius (see Supplemental Information)[26] and plotted as a function of drift gas polarizability (Figure 5.5a). Figure 5.5 shows that the polarizability of a drift gas does not have an equal effect on each ion's Ω, regardless of the fact that these compounds are very similar in size and shape. This analysis is consistent with studies from Hill *et al.*, which determined that while the relationship between ion radius and polarizability is linear, drift gas polarizability does not affect all ions equally.[26,27] However, the differences between each ions' radius in this study and the best-fit lines have an obvious quadratic residual (Figure 5.5b), even when using the same drift gases as Hill *et al*. Therefore, a linear fit is too simplistic to describe the relationship between ion radius and the drift gas polarizability.

An alternate method to evaluate the effect of polarizability on ion mobility involves calculating collision cross sections (Ω_{Cal}) using different methods. Figure 5.6 shows Ω_{Cal} as a function of Ω_{Exp} using the projection approximation (PA),[32] the exact hard spheres scattering method (EHSS)[33,34] and the trajectory method (TM).[35,41] Ω_{He} were initially calculated using the PA in MOBCAL[41] with pre-defined atomic radii. The resulting Ω_{Cal} are larger than experimental results with a root-mean-square deviation (RMSD) of 3.41 (Table S5.3, Figure S5.1a). When the PA is scaled to 95%, however, Ω_{Cal} with He are more comparable to experiment with an RMSD of 0.51 (Table S5.3, Figure S5.1a). Therefore, the pre-defined effective atomic radii of H, C, N, and O are not appropriate for this set of molecules.

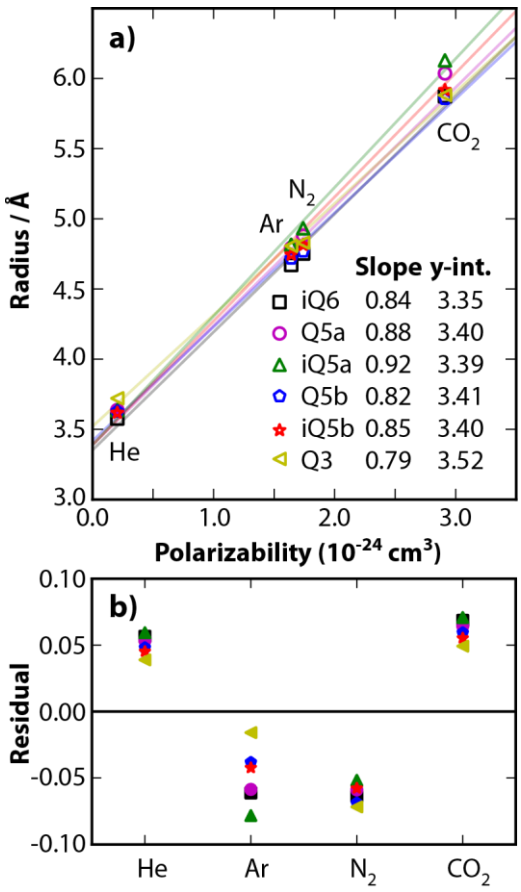

Figure 5.5. (a) Ω of iQ6 (*black squares*), Q5a (*purple circles*), iQ5a (*green triangles*), Q5b (*blue pentagons*), iQ5b (*red stars*), and Q3 (*yellow triangles*) plotted as a function of drift gas polarizability. Listed are the slopes and y-intercepts of each best-fit line. (b) Residual values for each compound with each drift gas (He, Ar, N_2, and CO_2).

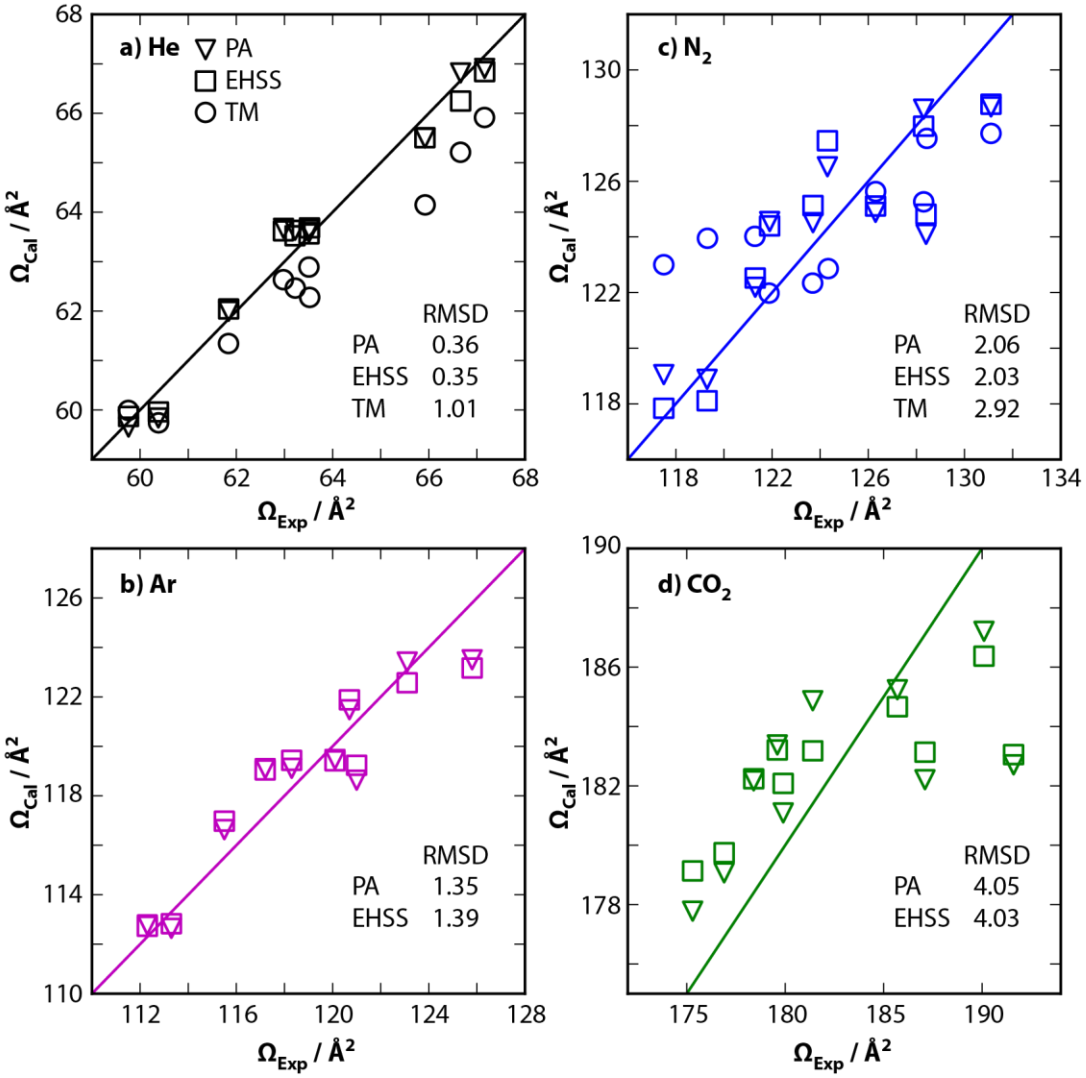

Figure 5.6. Calculated Ω (Ω_{Cal}) shown as a function of measured Ω (Ω_{Exp}) with (a) He, (b) Ar, (c) N_2, and (d) CO_2. The calculation methods include the projection approximation (PA),[32] the exact hard spheres scattering method (EHSS),[33,34] and the trajectory method (TM)[35,41] using natural population analysis (NPA) partial charges. Optimized radii (Table S5.4), determined using Ω_{Exp} and a basin-hopping algorithm, were used in the determination of Ω_{Cal} using the PA and EHSS methods.

To determine the appropriate effective radii for use with the PA for this set of molecules, the atomic radii of H, C, N, and O were optimized with each gas using a basin-hopping algorithm and are reported in Table S5.4. Using these optimized radii, the PA compared with experimental results has an RMSD of 0.36 with He, 1.35 with Ar, 2.06 with N_2 and 4.05 with CO_2 (Figure 5.6a-d, respectively). The same optimization method was used to determine the effective radii for use with the EHSS method. Using those optimized radii, the EHSS method compared with experimental results has an RMSD of 0.35 with He, 1.39 with Ar, 2.03 with N_2 and 4.03 with CO_2 (Figure 5.6a-d, respectively). The PA and EHSS methods, using optimized effective radii, are reasonable for estimating Ω_{He} and Ω_{Ar} for this set of molecules. Ω results for both methods with each gas are reported in Table S5.5.

Additionally, Ω_{He} were calculated using the trajectory method (TM) in MOBCAL (Table S5.3, Figure 5.6a).[35] The TM includes Lennard-Jones interactions between an ion and drift gas. When using the TM, it is important to include a partial charge for each atom in the molecule. For this study, three different methods were used to determine partial charges: Mulliken, Merz-Singh-Kollman (MK) constrained to reproduce the dipole moment (pop = (mk,dipole)), and Natural Population Analysis (NPA, pop = npa). Using the TM, the Mulliken, MK and NPA methods have similar RMSD values with He (1.03, 1.04, and 1.01, respectively) and partial charges using NPA are shown in Figure 5.6a. Residual values between Ω_{Cal} and Ω_{Exp} are shown in Figure S5.1a. Ω_{N_2} were also calculated using the TM and the same partial charge methods as He (Figure S5.1b). The MK method had the smallest RMSD with N_2 (2.76) followed by NPA (2.92) and Mulliken (9.93). TM results using NPA partial charges with N_2 are shown in Figure 5.6c and residual values are shown in Figure S5.1b.

Given the results from all three methods (PA with optimized radii, EHSS with optimized radii, and TM using NPA partial charges), the best methods for calculating Ω_{He}, Ω_{Ar} and Ω_{N_2} are the PA and EHSS with optimized radii. Ω_{CO_2} determined using the PA and EHSS methods are not comparable to experimental results and therefore other methods that include long range interactions should be used. The TM (which includes long-range interactions) with NPA partial charges is reasonable for calculating Ω_{He} and Ω_{N_2} but is not yet available for use with Ar and CO_2.

5.4.3 Peak Capacity. Peak capacity (P_c) was used to analyze the orthogonality and information content of each drift gas. P_c is defined as:

$$P_c = \frac{t_{max} - t_{min}}{0.5(w_{max} + w_{min})} \quad (5.5)$$

where t_{max} and t_{min} are the drift times of the least and most mobile ions and w_{max} and w_{min} are the width at base of those ions, respectively. P_c values determined from experiment in this study and using a drift voltage of 127 V are 1.34 (He), 2.06 (Ar), 1.84 (N_2), and 1.64 (CO_2) (Table 5.3). The instrument used here is not optimized for P_c and lower pressures were used for heavier gases in order to minimize fragmentation during ion injection, which both contribute to the small experimental P_c. Previously, we determined the maximum P_c possible on a high-performance instrument (Figure S5.2a, Table S5.6),[22] as a function of drift gas using amino acid (AA) ions as the data set and the previously derived equation for P_c, which includes contributions to peak widths from diffusion and gating.[42] Glycine and tryptophan were the most and least mobile ions, respectively, in each gas. The P_c possible for the AA are 11.7 (He), 13.1 (Ar), 10.8 (N_2), and 10.2 (CO_2) (Figure S5.3a), which are much greater than experimental P_c: 3.0 (He), 3.8 (Ar), 3.1 (N_2), and 2.4 (CO_2).[42] When the same method is applied to analogues of Q7, the resulting

maximum P_c are 2.37 (He), 4.28 (Ar), 3.92 (N_2), and 3.69 (CO_2) (Figure S5.2), which are approximately twice that of the experimental P_c (Table 5.3).

Table 5.3. Experimental P_c and those determined using parameters for a high-performance instrument (Table S5.6).[22]

	He	**Ar**	**N_2**	**CO_2**
This work	1.34	2.06	1.84	1.64
PNNL	2.37	4.28	3.92	3.69

The maximum P_c possible for analogues of Q7 are noticeably smaller than that for the AA; $P_{c,max}$ for DBE in He is approximately one-fifth that of the AA in He, and $P_{c,max}$ for DBE in Ar, N_2 and CO_2 are approximately one-third that of the AA in the same gases (Figure S5.2). Previously, we showed that the magnitude of P_c depends on factors contributing to the widths of peaks (Equation 5.4) and the range of Ω,[42] which for the amino acid ions is quite large compared with the range of Ω in this study. Figure 4a shows that the range of Ω for this set of compounds generally increases from 7.4 (He), 13.5 (Ar), 13.6 (N_2) to 16.3 Å^2 (CO_2). This is compared to the range of AA ion Ω, which decreases from 35.6 (He), 30.9 (Ar), 29.1 (N_2) to 22.1 Å^2 (CO_2).[42] In both sets of data, Ar is most effective at separating small molecules followed by He for AA ions and N_2 for DBE ions.

5.4.5 Orthogonality of IM and MS. The relationship between IM and MS measurements is linear with He (Figure 5.3a). However, as the drift gas polarizability increases there are significant differences in relative Ω among DBE 7, 5 and 2 (Figures 5.3b-d) indicating differences in selectivity of each gas. The selectivity of each gas was characterized using peak-to-peak resolution ($R_{p\text{-}p}$, Equation 5.3), which is a quantitative measurement of separation for two ions. The threshold for resolved ions was chosen as $R_{p\text{-}p} = 1.0$. The $R_{p\text{-}p}$ of pairs of DBE 5 ions were determined for each gas at a drift voltage of 127 V (Table 5.4). The $R_{p\text{-}p}$ is ≤ 0.05 for each

pair of DBE 5 with He and increases to 0.51 with CO_2 for iQ5a and Q5b. These pairs of compounds are not completely resolved due to the relatively low resolving power (R_p) of mobility separations in this study.

Table 5.4. $R_{p\text{-}p}$ values for each pair of DBE 5 ions at a drift voltage of 127 V.

Pair	He	Ar	N_2	CO_2
Q5a : iQ5a	0.03	0.05	0.14	0.14
Q5a : Q5b	0.02	0.12	0.29	0.43
Q5a : iQ5b	0.01	0.07	0.17	0.29
iQ5a : Q5b	0.05	0.17	0.40	0.51
iQ5a : iQ5b	0.05	0.12	0.30	0.39
Q5b : iQ5b	0.01	0.05	0.12	0.14

To assess the $R_{p\text{-}p}$ that would occur on a higher-performance instrument, values were estimated for a high-performance drift tube developed at PNNL (Table S5.6).[22] Using a previously derived equation for peak capacity (P_c),[42] experimental Ω, optimal drift voltage for each drift gas (Figure S5.3b, Table S5.7), and Equations 1 to 4, $R_{p\text{-}p}$ were estimated for a high-performance drift tube with each gas (Table S5.7). The high-performance instrument improves separations with every gas except He. $R_{p\text{-}p}$ in Ar increase by up to 87%, in N_2 by up to 88%, and in CO_2 by up to 94%. This analysis demonstrates the potential for greater information content using larger, more-polarizable drift gases on a high-performance instrument, specifically in regards to petroleum and crude oil separations.

In petroleomics, the separation of DBE can be vital for producing higher-quality oils. Here, we determine the resolving power required to separate DBE in each gas. R_p is defined as (see derivation in Supplemental Information):

$$R_p = \frac{1}{\delta}, \quad \delta = \sqrt{\frac{32 k_B T}{Vez}} \tag{5.6}$$

The R_p required to resolve Q7 and iQ2 is 9 in He and N_2, 8 in Ar, and 11 in CO_2 (Table S5.8). The least and most mobile ions can be separated in any gas, however, this may not be true for ions with the same DBE. Figure 5.7 shows the critical R_p required to separate each pair of DBE 5 ions with each gas. Each pair with He requires $R_p > 100$ to achieve separation ($R_p = 6352$ is needed to separate Q5a from iQ5a with He), showing that He is not suitable for separating compounds with the same DBE. Greater R_p are required with each gas to separate ions that differ only in the placement of the nitrogen atom (Q5a:iQ5a and Q5b:iQ5b). The other pairs of DBE 5, which differ in placement of the nitrogen atom and/or placement of double bonds can be easily separated using Ar, N_2 or CO_2. Therefore, heavier gases are recommended for use in petroleum and crude oil separation experiments.

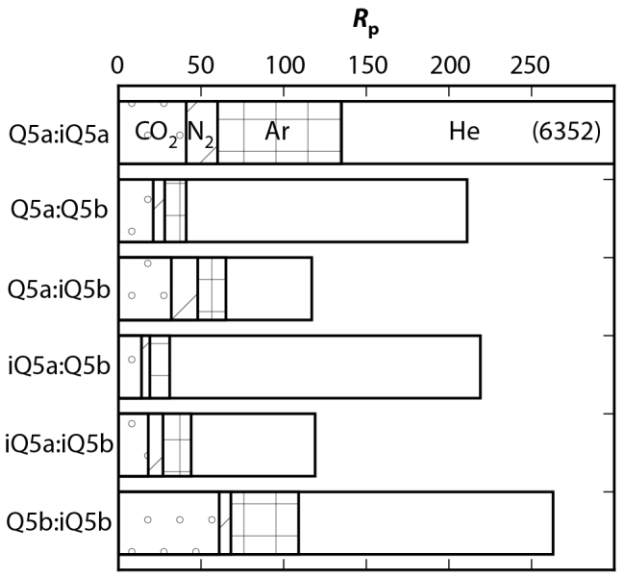

Figure 5.7. Critical resolving power (R_p, Equation 5.6) required to separate each pair of DBE 5 ions as a function of drift gas. CO_2 (*green*) requires the lowest R_p with each pair followed by N_2 (*blue*), Ar (*magenta*) and He (*gray*). The R_p needed to resolve Q5a from iQ5a in He was 6352, which is beyond the range of values considered here.

5.5 Conclusions

The Ω of ten petroleum-like ions with He, Ar, N_2 and CO_2 were measured on an rf-confining drift cell[37] at low pressures and ambient temperatures. The Ω increase with increasing polarizability of the gas, which was shown previously using amino acid ions.[42] The range of Ω also increases with polarizability of the gas, however, Ω of each ion do not increase uniformly. These results show that drift gases interact differently with ions of similar size and shape and therefore provide more information based on their orthogonality.

Ω were calculated using several methods in order to determine the origin of orthogonality between drift gases. Ω_{He}, Ω_{Ar} and Ω_{N_2} using the PA and EHSS methods and optimized atomic radii were comparable to experimental results with low RMSD. Ω_{CO_2} using the same methods were not accurate and the trajectory method (which includes long-range ion-neutral interactions) is currently only available for use with He and N_2.

The peak capacity (P_c, Figure S5.2) with each gas was evaluated for this rf-confining drift cell[43] and a high-performance drift tube (Table 5.3).[22] P_c is greatest in Ar followed by N_2, CO_2 and He. The selectivity of separations with each gas was determined using peak-to-peak resolution ($R_{p\text{-}p}$) for each pairwise combination of DBE 5 ions (Table 5.4). Overall, $R_{p\text{-}p}$ improved with polarizability of the drift gas. Additionally, we determined the minimum resolving power (R_p, Figure 5.7) needed to separate DBE 5 ions (Table S5.8). These results show that He is not an ideal drift gas for separating ions of similar size and shape but separations are possible with Ar, N_2 and CO_2. In general, this study shows that gases with greater polarizabilities increase the information content for petroleum-like molecules using IM-MS.

5.6 Acknowledgements. Acknowledgment is made to the Donors of the American Chemical Society Petroleum Research Fund for support of this research.

5.7 Supplemental Information. Discussion of equations, Tables S5.1 – S5.8, Figures S5.1 – S5.3.

5.8 References

(1) Marshall, A. G.; Rodgers, R. P. *Proc. Natl. Acad. Sci.* **2008**, *105* (47), 18090–18095.
(2) Ahmed, A.; Cho, Y. J.; No, M.; Koh, J.; Tomczyk, N.; Giles, K.; Yoo, J. S.; Kim, S. *Anal. Chem.* **2011**, *83* (1), 77–83.
(3) Ponthus, J.; Riches, E. *Int. J. Ion Mobil. Spectrom.* **2013**, *16* (2), 95–103.
(4) Fasciotti, M.; Lalli, P. M.; Klitzke, C. F.; Corilo, Y. E.; Pudenzi, M. A.; Pereira, R. C. L.; Bastos, W.; Daroda, R. J.; Eberlin, M. N. *Energy Fuels* **2013**, *27* (12), 7277–7286.
(5) Greene, D. L.; Hopson, J. L.; Li, J. *Energy Policy* **2006**, *34* (5), 515–531.
(6) Bae, E.; Na, J.-G.; Chung, S. H.; Kim, H. S.; Kim, S. *Energy Fuels* **2010**, *24* (4), 2563–2569.
(7) Wu, Z.; Rodgers, R. P.; Marshall, A. G. *Energy Fuels* **2004**, *18* (5), 1424–1428.
(8) Kim, S.; Rodgers, R. P.; Marshall, A. G. *Int. J. Mass Spectrom.* **2006**, *251* (2–3), 260–265.
(9) Qian, K.; Mennito, A. S.; Edwards, K. E.; Ferrughelli, D. T. *Rapid Commun. Mass Spectrom.* **2008**, *22* (14), 2153–2160.
(10) Fernandez-Lima, F. A.; Becker, C.; McKenna, A. M.; Rodgers, R. P.; Marshall, A. G.; Russell, D. H. *Anal. Chem.* **2009**, *81* (24), 9941–9947.
(11) Hur, M.; Yeo, I.; Park, E.; Kim, Y. H.; Yoo, J. S.; Kim, E.; No, M.; Koh, J.; Kim, S. *Anal. Chem.* **2010**, *82* (1), 211–218.
(12) Shi, Q.; Hou, D.; Chung, K. H.; Zhao, S.; Zhang, Y. *Energy Fuels* **2010**, *24* (4), 2545–2553.
(13) Zhang, L.; Zhang, Y.; Zhao, S.; Xu, C.; Chung, K. H.; Shi, Q. *Sci. China Chem.* **2013**, *56* (7), 874–882.
(14) McKenna, A. M.; Purcell, J. M.; Rodgers, R. P.; Marshall, A. G. *Energy Fuels* **2010**, *24* (5), 2929–2938.
(15) Siems, W. F.; Viehland, L. A.; Hill, H. H. *Analyst* **2016**, *141* (23), 6396–6407.
(16) Mason, E. A.; McDaniel, E. W. *Transport Properties of Ions in Gases*; Wiley: New York, 1988.
(17) Dodds, J. N.; May, J. C.; McLean, J. A. *Anal. Chem.* **2017**, *89* (1), 952–959.
(18) Revercomb, H. E.; Mason, E. A. *Anal. Chem.* **1975**, *47* (7), 970–983.
(19) Kanu, A. B.; Gribb, M. M.; Hill, H. H. *Anal. Chem.* **2008**, *80* (17), 6610–6619.
(20) Ibrahim, Y. M.; Garimella, S. V. B.; Tolmachev, A. V.; Baker, E. S.; Smith, R. D. *Anal. Chem.* **2014**, *86* (11), 5295–5299.
(21) Baker, E. S.; Clowers, B. H.; Li, F.; Tang, K.; Tolmachev, A. V.; Prior, D. C.; Belov, M. E.; Smith, R. D. *J. Am. Soc. Mass Spectrom.* **2007**, *18* (7), 1176–1187.
(22) Ibrahim, Y. M.; Baker, E. S.; Danielson, W. F.; Norheim, R. V.; Prior, D. C.; Anderson, G. A.; Belov, M. E.; Smith, R. D. *Int. J. Mass Spectrom.* **2015**, *377*, 655–662.
(23) May, J. C.; Russell, D. H. *J. Am. Soc. Mass Spectrom.* **2011**, *22* (7), 1134–1145.
(24) Ujma, J.; Giles, K.; Morris, M.; Barran, P. E. *Anal. Chem.* **2016**, *88* (19), 9469–9478.
(25) Deng, L.; Ibrahim, Y. M.; Hamid, A. M.; Garimella, S. V. B.; Webb, I. K.; Zheng, X.; Prost, S. A.; Sandoval, J. A.; Norheim, R. V.; Anderson, G. A.; Tolmachev, A. V.; Baker, E. S.; Smith, R. D. *Anal. Chem.* **2016**, *88* (18), 8957–8964.
(26) Beegle, L. W.; Kanik, I.; Matz, L.; Hill, H. H., Jr. *Int. J. Mass Spectrom.* **2002**, *216*, 257–268.
(27) Asbury, G. R.; Hill, H. H. *Anal. Chem.* **2000**, *72* (3), 580–584.

(28) Lalli, P. M.; Corilo, Y. E.; Fasciotti, M.; Riccio, M. F.; de Sa, G. F.; Daroda, R. J.; Souza, G. H. M. F.; McCullagh, M.; Bartberger, M. D.; Eberlin, M. N.; Campuzano, I. D. G. *J. Mass Spectrom.* **2013**, *48* (9), 989–997.
(29) Fernandez-Maestre, R.; Meza-Morelos, D.; Hill, H. H. *Int. J. Mass Spectrom.* **2015**, *380*, 21–25.
(30) Rawat, V. K.; Vidal-de-Miguel, G.; Hogan, C. J. *Analyst* **2015**, *140* (20), 6945–6954.
(31) Meyer, N. A.; Root, K.; Zenobi, R.; Vidal-de-Miguel, G. *Anal. Chem.* **2016**, *88* (4), 2033–2040.
(32) von Helden, G.; Hsu, M. T.; Gotts, N.; Bowers, M. T. *J. Phys. Chem.* **1993**, *97* (31), 8182–8192.
(33) Shvartsburg, A. A.; Jarrold, M. F. *Chem. Phys. Lett.* **1996**, *261*, 86–91.
(34) Shvartsburg, A. A.; Mashkevich, S. V.; Baker, E. S.; Smith, R. D. *J. Phys. Chem. A* **2007**, *111* (10), 2002–2010.
(35) Campuzano, I.; Bush, M. F.; Robinson, C. V.; Beaumont, C.; Richardson, K.; Kim, H.; Kim, H. I. *Anal. Chem.* **2012**, *84* (2), 1026–1033.
(36) Davidson, K. L.; Oberreit, D. R.; Hogan, C. J.; Bush, M. F. *Int. J. Mass Spectrom.* DOI: 10.1016/j.ijms.2016.09.013.
(37) Allen, S. J.; Giles, K.; Gilbert, T.; Bush, M. F. *Analyst* **2016**, *141* (3), 884–891.
(38) Bush, M. F.; Campuzano, I. D. G.; Robinson, C. V. *Anal. Chem.* **2012**, *84* (16), 7124–7130.
(39) Dennington, R.; Keith, T.; Millam, J. *GaussView, Version 5*; Semichem Inc.: Shawnee Mission KS, 2009.
(40) Boschmans, J.; Jacobs, S.; P. Williams, J.; Palmer, M.; Richardson, K.; Giles, K.; Lapthorn, C.; A. Herrebout, W.; Lemière, F.; Sobott, F. *Analyst* **2016**, *141* (13), 4044–4054.
(41) Mesleh, M. F.; Hunter, J. M.; Shvartsburg, A. A.; Schatz, G. C.; Jarrold, M. F. *J. Phys. Chem.* **1996**, *100* (40), 16082–16086.
(42) Davidson, K. L.; Bush, M. F. *Anal. Chem.* **2017**, *89* (3), 2017–2023.
(43) Allen, S. J.; Bush, M. F. *J. Am. Soc. Mass Spectrom.* **2016**, *27*, 2054–2063.
(44) Lide, D. R., Ed. *CRC Handbook of Chemistry and Physics*, 96th ed.; CRC Press: Boca Raton, FL, 2015.

Appendix A

Supplemental Information for Chapter 2

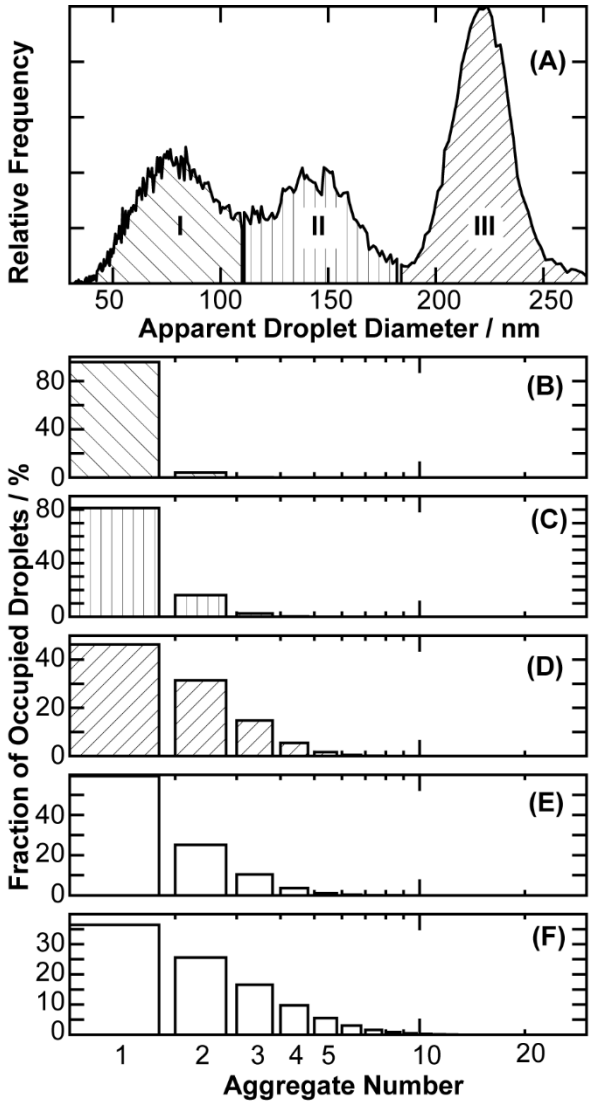

Figure S2.1. Droplet size distribution measured at 75 nA (A). The percent of occupied droplets as a function of aggregate number in log scale assuming a concentration of 400 nM analyte for subpopulation I (B), subpopulation II (C), subpopulation III (D), subpopulations I and III (E), and subpopulations I, II, and III (F).

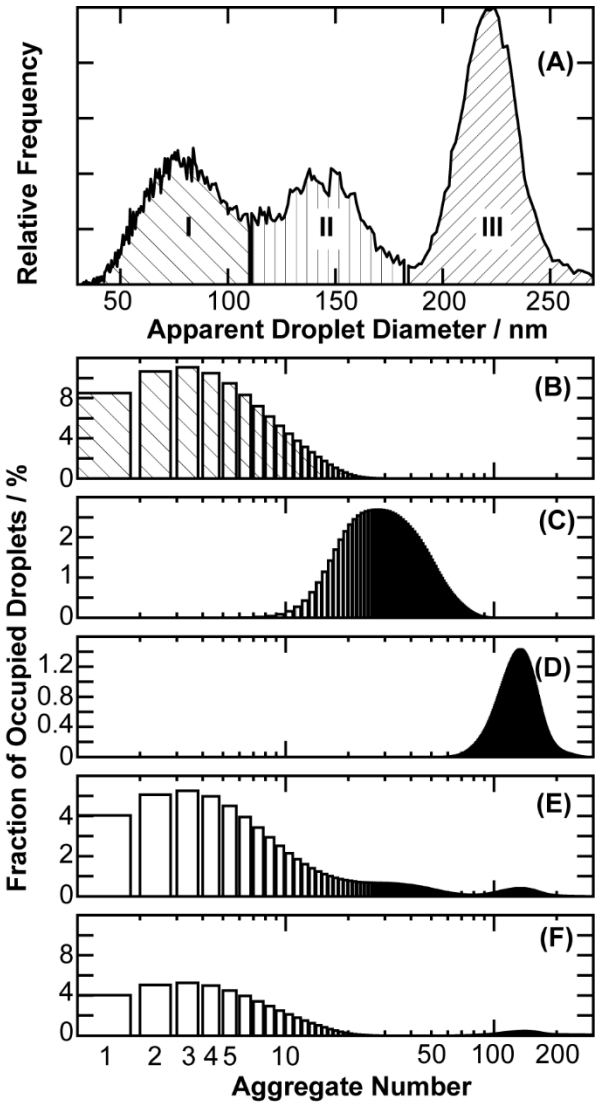

Figure S2.2. Droplet size distribution measured at 75 nA (A). The percent of occupied droplets as a function of aggregate number in log scale assuming a concentration of 40 µM analyte for subpopulation I (B), subpopulation II (C), subpopulation III (D), subpopulations I and III (E), and subpopulations I, II, and III (F).

Appendix B

Supplemental Information for Chapter 3

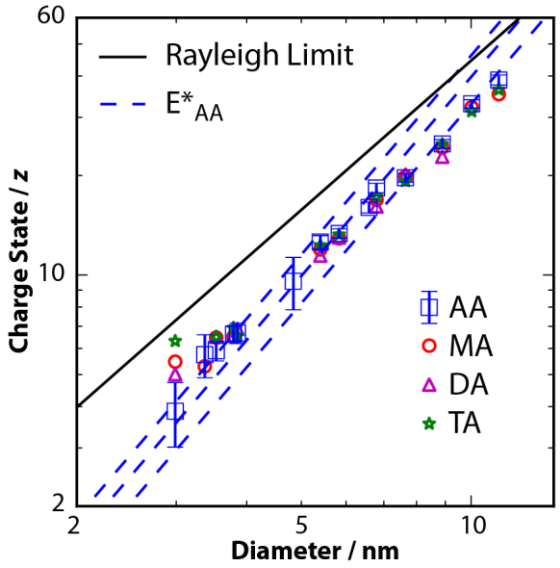

Figure S3.1. Average charge states of anionic proteins sprayed from four different buffers: ammonium acetate (AA, *blue squares*), methylammonium acetate (MA, *red circles*), dimethylammonium acetate (DA, *magenta triangles*), and trimethylammonium acetate (TA, *green stars*). E* values for AA in negative ion mode are 2.65, 2.29 and 1.89 V nm^{-1}.

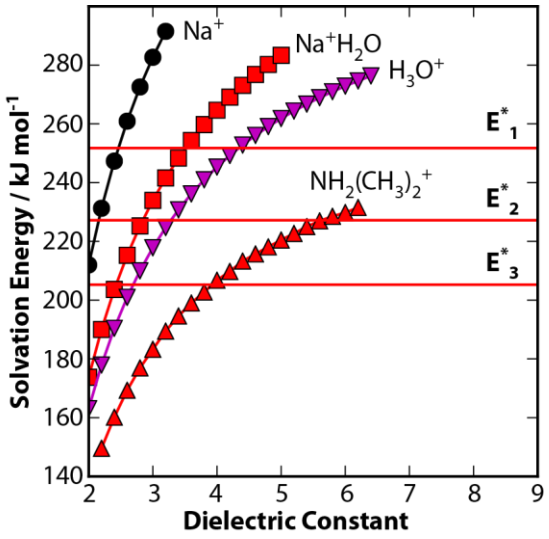

Figure S3.2. The solvation energies of possible charge carriers in methylammonium acetate buffer as a function of dielectric constant. Critical field strengths (E*, *horizontal lines*) are shown for reference.

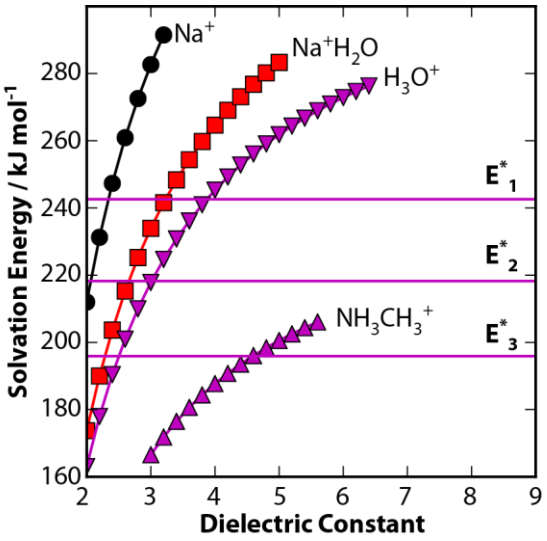

Figure S3.3. The solvation energies of possible charge carriers in dimethylammonium acetate buffer as a function of dielectric constant. Critical field strengths (E*, *horizontal lines*) are shown for reference.

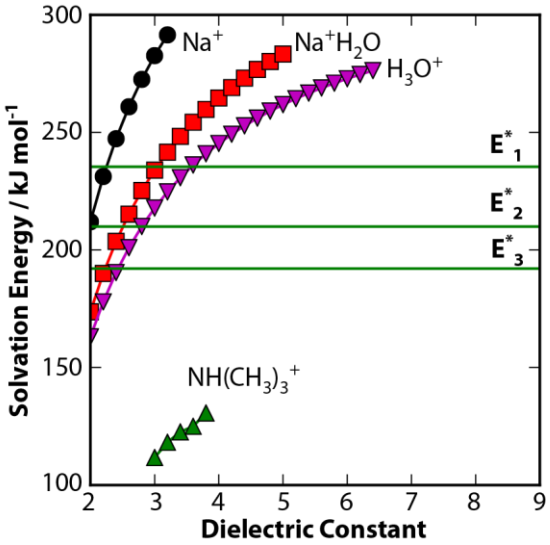

Figure S3.4. The solvation energies of possible charge carriers in trimethylammonium acetate buffer as a function of dielectric constant. Critical field strengths (E*, *horizontal lines*) are shown for reference.

Appendix C

Supplemental Information for Chapter 4

Derivations of Selected Equations

In this section, all equations used in the main body are numbered using the same Arabic numerals used in the main body. All additional equations are numbered using Roman numerals.

Equation **4.5** defines the peak capacity (P_c) in terms of the drift times (t_D) and widths (w) of the least and most mobile ions:

$$P_C = \frac{t_{D2} - t_{D1}}{0.5(w_2 + w_1)} \quad \textbf{(4.5)}^1$$

In order to develop an analytical expression for *Pc* based on the properties of the ions and the parameters used for the ion mobility separation, expressions were developed for t_D and w.

Equations **4.1** and **4.2** relate t_D, mobility (K), and collision cross section (Ω):[2]

$$t_D = \frac{L}{E}\frac{1}{K} = \frac{L^2}{V}\frac{1}{K} \quad \textbf{(4.1)}$$

$$\Omega = \frac{3ez}{16N}\sqrt{\frac{2\pi}{\mu k_B T}}\frac{1}{K} \quad \textbf{(4.2)}^2$$

where L is the length of the drift cell, V is the voltage change across the drift cell, e is the elementary charge, z is the charge state of the ion, N is the number density of the drift gas, μ is the reduced mass of the ion and neutral, k_B is the Boltzmann constant, and T is the drift-gas temperature. Solving Equation **4.2** for reciprocal mobility (K^{-1}) yields:

$$\frac{1}{K} = \frac{16N}{3ez}\sqrt{\frac{\mu k_B T}{2\pi}}\Omega \quad \textbf{(4.I)}$$

Substituting Equation **4.I** into Equation **4.1** yields Equation **4.II**, in which t_D depends on Ω, μ, and τ (defined in Equation **4.9**):

$$t_D = \frac{16N}{3ez}\sqrt{\frac{\mu k_B T}{2\pi}}\frac{L^2}{V}\Omega = \tau\sqrt{\mu}\Omega \quad \textbf{(4.II)}$$

$$\tau = \frac{16N}{3ez}\sqrt{\frac{k_B T}{2\pi}}\frac{L^2}{V} \quad \textbf{(4.9)}$$

For diffusion-limited ion mobility separations, the resolving power is:

$$\frac{t_D}{FWHM} = \sqrt{\frac{Vez}{16k_BTln2}} \quad \textbf{(4.III)}^3$$

Solving Equation **4.III** for FWHM yields Equation **4.IV**:

$$FWHM = \sqrt{\frac{16k_BTln2}{Vez}}\, t_D \quad \textbf{(4.IV)}$$

For a Gaussian peak, the width (4σ) is proportional to the FWHM ($2\sqrt{2ln2}\sigma$). Therefore, the width from diffusion (w_d) depends on Ω, μ, τ, and δ (defined in Equation **4.7**):

$$w_d = \frac{4}{2\sqrt{2ln2}}\sqrt{\frac{16k_BTln2}{Vez}}\, t_D = \sqrt{\frac{32k_BT}{Vez}}\, t_D = \delta t_D = \delta\tau\sqrt{\mu}\Omega \quad \textbf{(4.V)}$$

$$\delta = \sqrt{\frac{32k_BT}{Vez}} \quad \textbf{(4.7)}$$

For most ion mobility separations, the total width of peaks (w) will also have contributions from gating (w_g):

$$w^2 = {w_g}^2 + {w_d}^2 \quad \textbf{(4.4)}$$

Substituting Equation **4.V** into Equation **4.4** and solving for w yields Equation **4.VI**, in which w depends on w_g, δ, τ, μ, and Ω:

$$w = \sqrt{{w_g}^2 + \delta^2\tau^2\mu\Omega^2} \quad \textbf{(4.VI)}$$

Substituting the expressions for t_D (Equation **4.II**) and w (Equation **4.VI**) into Equation **4.5** yields Equation **4.8**:

$$P_C = \frac{2\tau(\sqrt{\mu_2}\Omega_2 - \sqrt{\mu_1}\Omega_1)}{\sqrt{{w_g}^2 + \delta^2\tau^2\mu_2{\Omega_2}^2} + \sqrt{{w_g}^2 + \delta^2\tau^2\mu_1{\Omega_1}^2}} \quad \textbf{(4.8)}$$

For diffusion-limited separations, $w_g = 0$, which yields:

$$P_C = \frac{2}{\delta}\frac{(\sqrt{\mu_2}\Omega_2 - \sqrt{\mu_1}\Omega_1)}{(\sqrt{\mu_2}\Omega_2 + \sqrt{\mu_1}\Omega_1)} \quad \textbf{(4.6)}$$

Table S4.1. Praxair gas cylinder product numbers

Gas	Praxair
He	5.0UH-T
Ar	5.0UH-T
N_2	4.8RS-K
CO_2	4.8RS-K
N_2O	4.8SP-K

Table S4.2. Parameters for mobility measurements using a rf-confining drift cell[4] at a drift voltage of 127 V and different drift gases.

Gases	He Cell Entrance (V)	He Cell Exit (V)	He Cell DC (V)	IMS Bias (V)
He, N_2	-20	-40	0	172
Ar, CO_2, N_2O	-5	-10	0	142

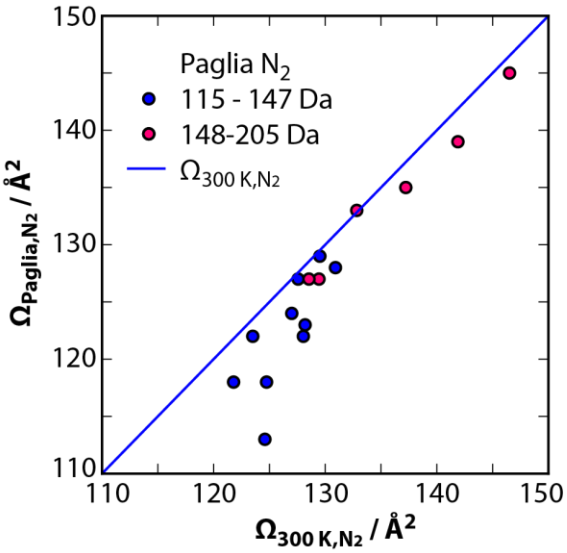

Figure S4.1. Ω_{N_2} of amino acid ions (using traveling-wave ion mobility)[5] as a function of $\Omega_{300\ K}$ with N_2.

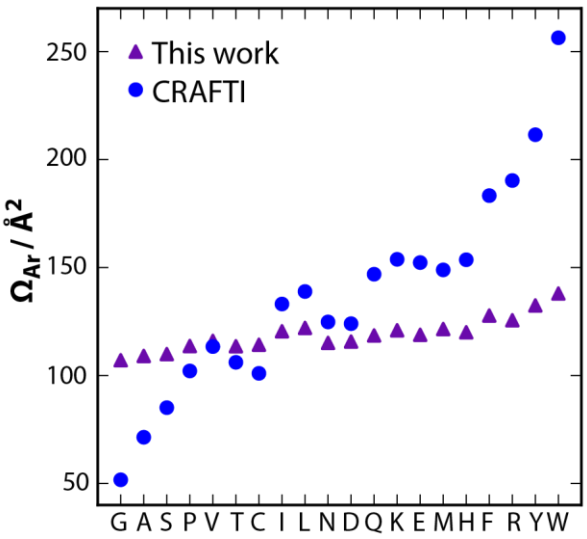

Figure S4.2. Ω of the protonated amino acids with Ar, in order of increasing amino acid mass, using an rf-confining drift cell (*purple triangles*) and CRAFTI (*blue circles*).[6]

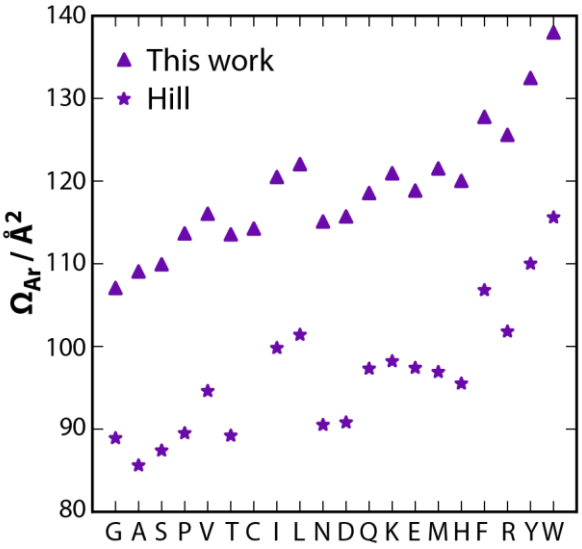

Figure S4.3. Ω of the protonated amino acids with Ar, in order of increasing amino acid mass, using an rf-confining drift cell (*purple triangles*) and drift-tube ion mobility (*purple stars*).[7]

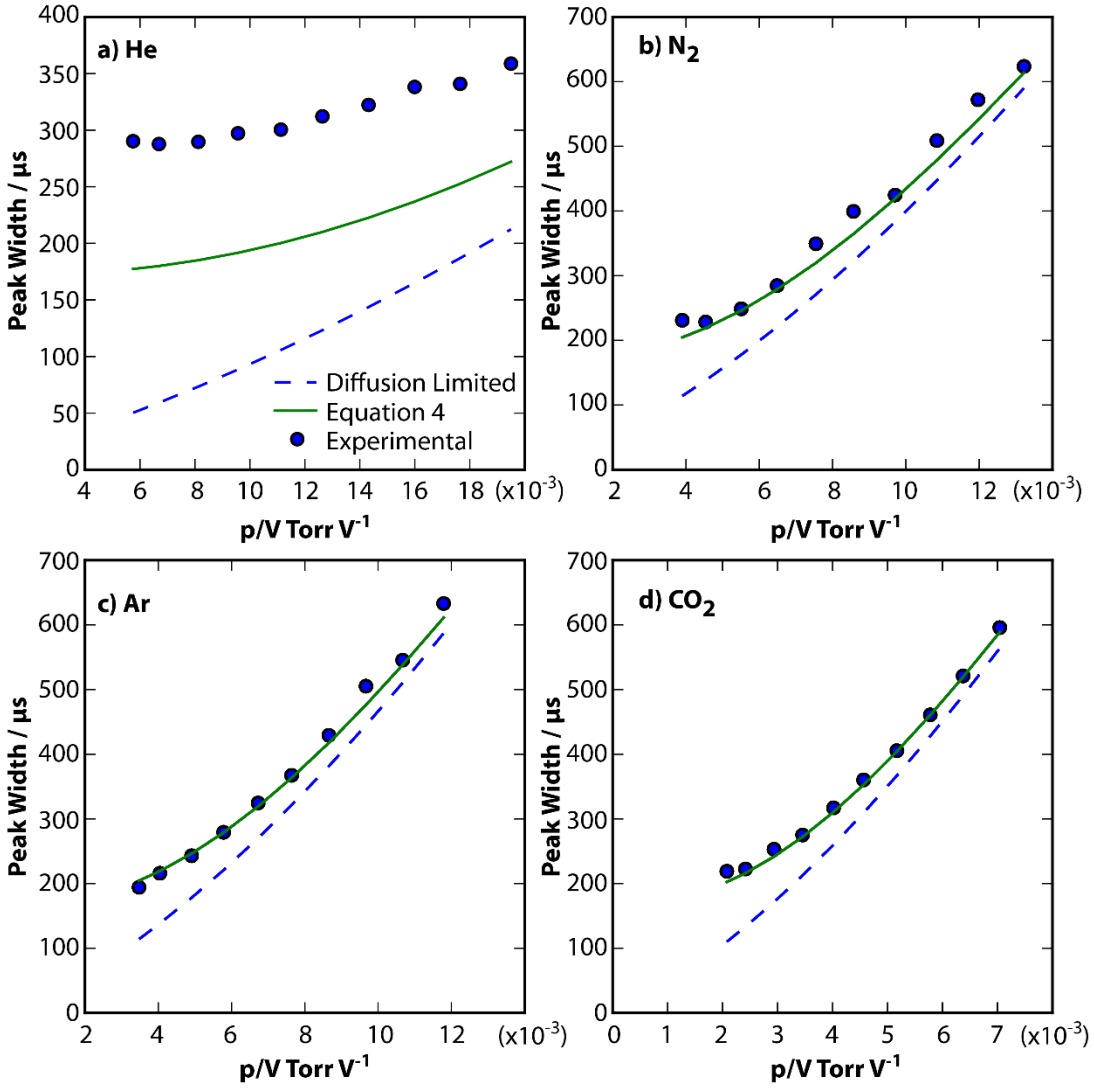

Figure S4.4. Experiment peak widths at base (4σ) compared with diffusion-limited peak widths (w_d) and peak widths calculated using Equation 4 with an initial ion pulse width of 170 µs for a) He, b) N_2, c) Ar, and d) CO_2. The peak widths determined from the experiments in He are broader than expected. Therefore, other factors may contribute to the width of peaks observed for the experiments in He, such as space-charge effects[4,8] or broadening during transport to the mass analyzer. Result for N_2O were similar to those for CO_2 and are not shown.

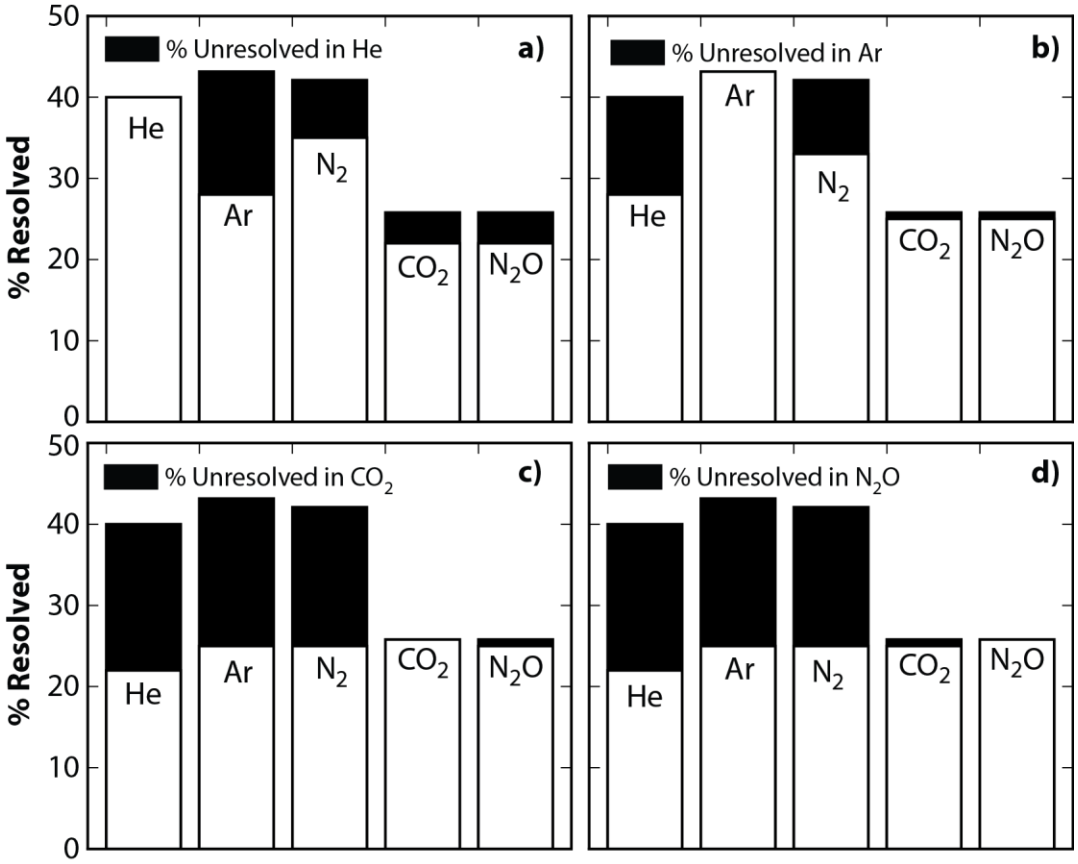

Figure S4.5. The fraction of resolved pairs of amino acids for each gas listed in order of increasing polarizability. Shaded regions indicate the fraction of complementary selectivity relative to a) He, b) Ar, c) CO_2 and d) N_2O.

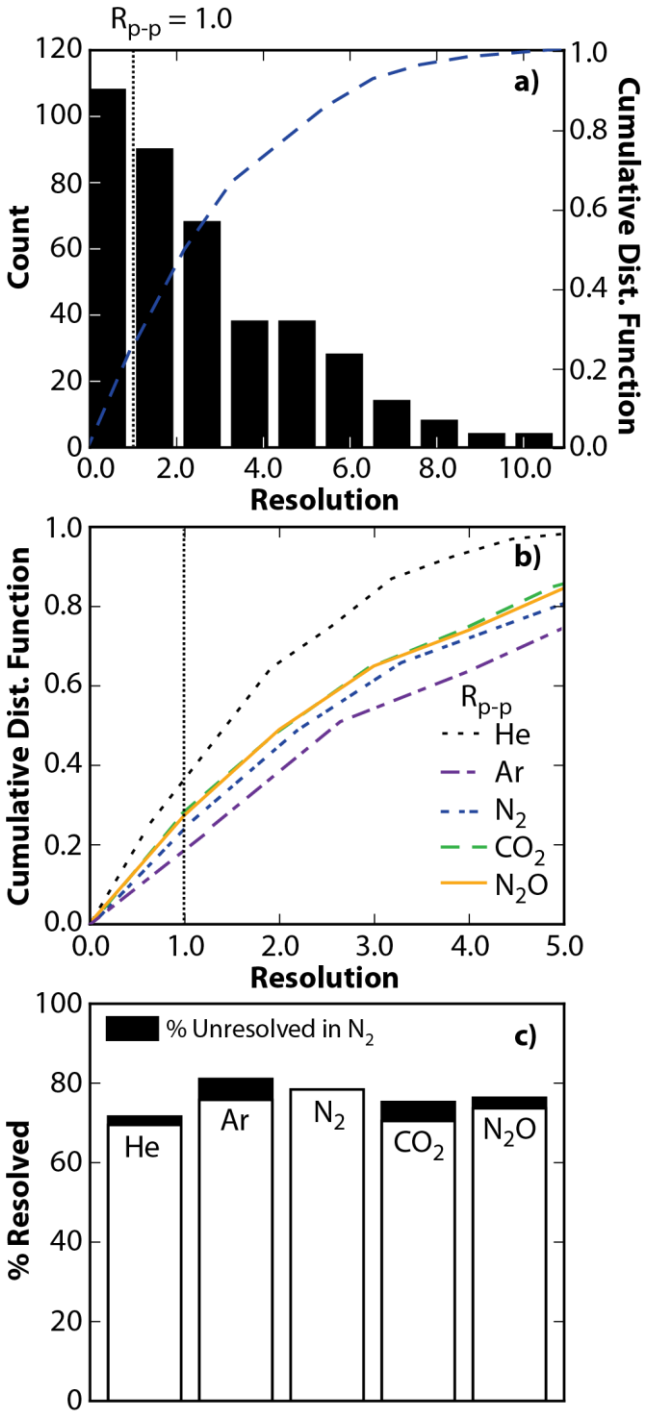

Figure S4.6. (a) A histogram representation of calculated $R_{p\text{-}p}$ (Equation 4.3) for every pair-wise combination of amino acids with N_2 estimated for a high-performance drift tube (Table 4.3).[9] The vertical dashed line indicates the threshold for resolved amino acids (≥ 1.0). (b) Cumulative distribution functions were calculated for peak-to-peak resolutions ($R_{p\text{-}p}$) with He (black), Ar (purple), N_2 (blue), CO_2 (green), and N_2O (yellow). (c) The fraction of resolved pairs of amino acids for each gas listed in order of increasing polarizability. Shaded regions indicate the fraction of complementary pairs identified relative to N_2.

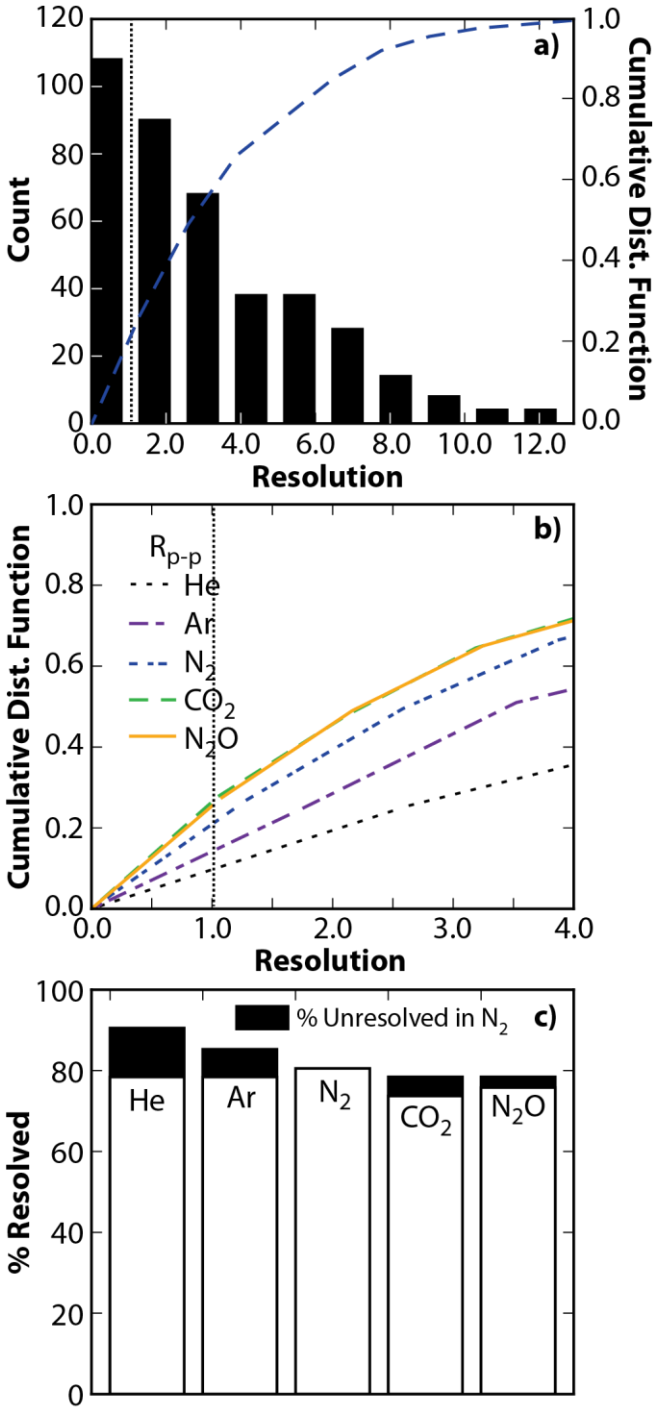

Figure S4.7. a) A histogram representation of calculated $R_{p\text{-}p}$ for every pair-wise combination of amino acids in N_2 estimated for a high-performance drift tube, without contributions from gating (Table 4.3).[9] The vertical dashed line indicates the threshold for resolved pairs of amino acids (≥ 1.0). b) Cumulative distribution functions were calculated for peak-to-peak resolutions ($R_{p\text{-}p}$) with He (black), Ar (purple), N_2 (blue), CO_2 (green), and N_2O (yellow). c) The fraction of resolved amino acids for each gas listed in order of increasing polarizability. Shaded regions indicate the fraction of complementary pairs identified relative to N_2.

References

(1) Ruotolo, B. T.; Gillig, K. J.; Stone, E. G.; Russell, D. H. *J. Chromatogr. B Analyt. Technol. Biomed. Life. Sci*. **2002**, *782*, 385–392.

(2) Mason, E. A.; McDaniel, E. W. *Transport Properties of Ions in Gases*; Wiley: New York, **1988**.

(3) Revercomb, H. E.; Mason, E. A. *Anal. Chem*. **1975**, *47*, 970–983.

(4) Allen, S. J.; Giles, K.; Gilbert, T.; Bush, M. F. *Analyst* **2016**, *141*, 884–891.

(5) Paglia, G.; Williams, J. P.; Menikarachchi, L.; Thompson, J. W.; Tyldesley-Worster, R.; Halldórsson, S.; Rolfsson, O.; Moseley, A.; Grant, D.; Langridge, J.; Palsson, B. O.; Astarita, G. *Anal. Chem.* **2014**, *86*, 3985–3993.

(6) Anupriya; Jones, C. A.; Dearden, D. V. *J. Am. Soc. Mass Spectrom*. **2016**, *27*, 1366–1375.

(7) Asbury, G. R.; Hill Jr., H. H. *J. Chromatogr. A* **2000**, *902*, 433–437.

(8) May, J. C.; Dodds, J. N.; Kurulugama, R. T.; Stafford, G. C.; Fjeldsted, J. C.; McLean, J. A. *Analyst* **2015**, *140*, 6824–6833.

(9) Ibrahim, Y. M.; Baker, E. S.; Danielson, W. F.; Norheim, R. V.; Prior, D. C.; Anderson, G. A.; Belov, M. E.; Smith, R. D. *Int. J. Mass Spectrom*. **2015**, *377*, 655–662.

Appendix D

Supplemental Information for Chapter 5

Discussion of Equations

Ω of iQ6, Q5a, iQ5a, Q5b, iQ5b, and Q3 were converted to a radius (r_{ion}):[1]

$$r_{ion} = \left(\frac{\Omega}{\pi}\right)^{1/2} - r_{gas} \quad \text{(I)}$$

where r_{gas} is the radius of the neutral. The radius of the neutral was estimated using a hard-sphere model:[1]

$$r_{gas}^2 = \frac{1}{4}\left(\frac{5}{16\pi^{1/2}}\right)\left(\frac{(MRT)^{1/2}}{N_A\eta}\right) \quad \text{(II)}$$

where M is the mass of the neutral, R is the gas constant, T is the temperature, N_A is Avogadro's constant and η is the viscosity of the gas.

R_p is defined as:

$$R_p = \frac{t_D}{w} \quad \text{(III)}$$

First, t_D is related to Ω using Equations 5.1 and 5.2:

$$t_D = \tau\sqrt{\mu}\Omega,\ \tau = \frac{16N}{3ez}\sqrt{\frac{k_BT}{2\pi}}\frac{L^2}{V} \quad \text{(IV)}$$

The diffusion-limited width is related to Ω using the following:

$$w_d = \delta\tau\sqrt{\mu}\Omega,\ \delta = \sqrt{\frac{32k_BT}{Vez}} \quad \text{(V)}$$

Using Equations 5.4 and IV, $R_{p\text{-}p}$ becomes:

$$R_{p-p} = \frac{\sqrt{\mu_2}\Omega_2 - \sqrt{\mu_1}\Omega_1}{0.5\delta(\sqrt{\mu_2}\Omega_2 + \sqrt{\mu_1}\Omega_1)} \quad \text{(VI)}$$

Using Equations III and IV, R_p becomes:

$$R_p = \frac{1}{\delta} \quad (5.6)$$

Table S5.1. Praxair gas cylinder product numbers.

Gas	Praxair
He	5.0UH-T
Ar	5.0UH-T
N_2	4.8RS-K
CO_2	4.8RS-K

Table S5.2. Parameters for mobility measurements using a rf-confining drift cell[2] at a drift voltage of 127 V and different drift gases.

Gases	He Cell Entrance (V)	He Cell Exit (V)	He Cell DC (V)	IMS Bias (V)
He, N_2	-20	-40	0	172
Ar, CO_2, N_2O	-5	-10	0	142

Table S5.3. Theoretical Ω in $Å^2$ with He and N_2 using MOBCAL and different methods.

	Ω_{He}					Ω_{N_2}		
Number	1.00 PA	0.95 PA	TM, Mulliken	TM, MK	TM, NPA	TM, Mulliken	TM, MK	TM, NPA
Q7	63.44	60.69	62.08	59.48	59.74	143.4	121.3	123.0
iQ7	63.43	60.69	60.62	59.70	59.99	128.4	122.0	124.0
iQ6	65.48	62.48	61.90	61.16	61.34	128.0	122.5	124.0
Q5a	66.93	63.77	64.12	62.23	62.28	136.9	124.5	125.6
iQ5a	66.48	63.57	62.76	62.83	62.89	124.9	125.7	127.5
Q5b	66.89	63.76	63.02	62.45	62.47	127.0	122.0	122.0
iQ5b	66.97	63.81	62.91	62.55	62.64	124.5	122.3	122.3
Q3	68.86	65.59	64.53	64.29	64.15	125.1	122.3	122.9
iQ2	70.29	66.84	65.72	65.72	65.91	126.2	126.4	127.7
Q2	70.09	66.65	65.23	65.29	65.21	124.9	124.6	125.3
RMSD	3.41	0.512	1.03	1.04	1.01	9.93	2.76	2.92

Table S5.4. Optimized effective radii (Å) for PA and EHSS methods with each gas.

	He		**Ar**		**N_2**		**CO_2**	
Atom	PA	EHSS	PA	EHSS	PA	EHSS	PA	EHSS
H	2.09	1.95	3.69	3.61	3.81	3.75	5.04	4.94
C	2.52	2.64	3.75	3.95	4.27	3.95	5.65	5.90
N, O	2.58	2.66	3.45	4.06	4.03	4.20	6.33	6.05

Table S5.5. Ω in Å^2 determined using optimized radii (Table S5.4) and the PA and EHSS methods with He, Ar, N_2 and CO_2.

	He		**Ar**		**N_2**		**CO_2**	
	PA	EHSS	PA	EHSS	PA	EHSS	PA	EHSS
Q7	59.8	60.0	112.8	112.7	119.1	117.8	177.8	179.1
iQ7	59.7	59.9	112.6	112.8	118.9	118.1	179.1	179.8
iQ6	62.0	62.0	116.6	117.0	122.2	122.5	181.1	182.1
Q5a	63.7	63.7	119.5	119.4	124.9	125.1	182.2	183.1
iQ5a	63.6	63.6	118.6	119.2	124.1	124.8	182.7	183.1
Q5b	63.6	63.5	119.1	119.0	124.6	124.4	182.2	182.2
iQ5b	63.7	63.6	119.1	119.4	124.5	125.1	184.9	183.2
Q3	65.5	65.5	121.5	121.9	126.5	127.5	183.4	183.2
iQ2	66.9	66.8	123.5	123.2	128.7	128.8	187.2	186.4
Q2	66.8	66.2	123.4	122.6	128.6	128.0	185.2	184.7

Table S5.6. Instrument parameters used in $R_{p\text{-}p}$ and P_c calculations.

	L cm	***w_g*** µs	***V*** V	***E*** V cm^{-1}	***P*** Torr
rf-confining drift cell[2]	25.2	170	127	6.79	Table 5.1
high-performance drift tube[3]	94	286	Table S5.7	17.0	4.0

Table S5.7. $R_{p\text{-}p}$ values for each pair of DBE 5 ions using parameters for a high-performance instrument (Table S5.6) and optimized voltages listed beneath the corresponding gas.

Pair	**He** (499 V)	**Ar** (1512 V)	**N_2** (1416 V)	**CO_2** (2063 V)
Q5a : iQ5a	$2.8\text{x}10^{-5}$	0.071	0.35	1.1
Q5a : Q5b	$9.3\text{x}10^{-3}$	0.77	1.5	3.9
Q5a : iQ5b	$3.1\text{x}10^{-2}$	0.30	0.53	1.7
iQ5a : Q5b	$8.3\text{x}10^{-3}$	1.3	3.3	9.0
iQ5a : iQ5b	$2.9\text{x}10^{-2}$	0.67	1.7	5.4
Q5b : iQ5b	$6.3\text{x}10^{-3}$	0.11	0.25	0.45

Table S5.8. Resolving power (R_p, Equation 5.6) needed for separation between pairs of DBE in each gas and for separation of DBE 7 and 2.

Pair	**He**	**Ar**	**N_2**	**CO_2**
Q7 : iQ7	95	110	65	112
Q5a : iQ5a	6352	135	60	41
Q5a : Q5b	211	41	28	21
Q5a : iQ5b	117	65	48	32
iQ5a : Q5b	219	31	19	14
iQ5a : iQ5b	119	44	27	18
Q5b : iQ5b	263	109	68	61
Q2 : iQ2	134	47	46	42
Q7:iQ2	9	8	9	11

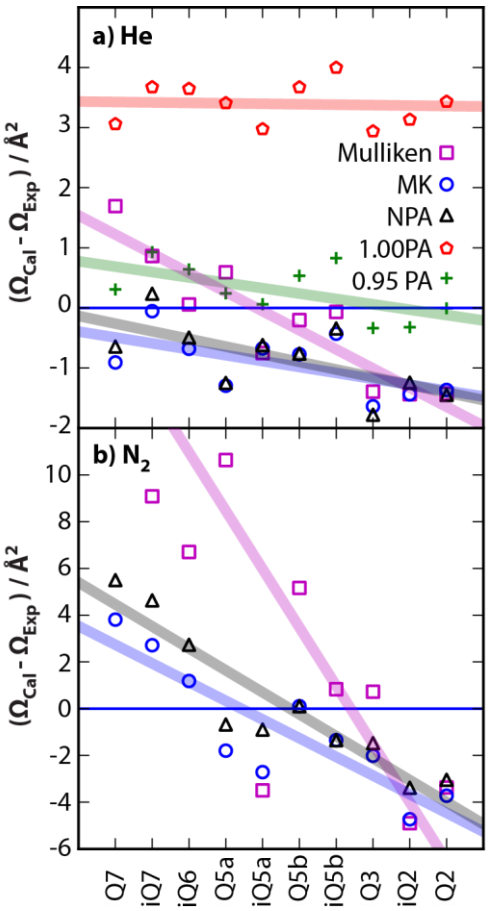

Figure S5.1. Differences between calculated Ω (Ω_{Cal}) and experimental Ω (Ω_{Exp}) with (a) He and (b) N_2 using the Trajectory Method (TM) in MOBCAL[4] with Mulliken (*purple squares*), Merz-Singh-Kollman (MK) (*blue circles*), and Natural Population Analysis (NPA) partial charges (*black triangles*) and the Projection Approximation[5] (PA) in MOBCAL without scaling (1.00 PA, *red pentagons*) and scaled to 95% (0.95 PA, *green plus signs*). The difference for Q7 using Mulliken partial charges with N_2 is 26, but for scaling purposes is not shown. The 95% confidence interval for TM MOBCAL calculations is, on average, 0.1 to 0.2 Å^2.

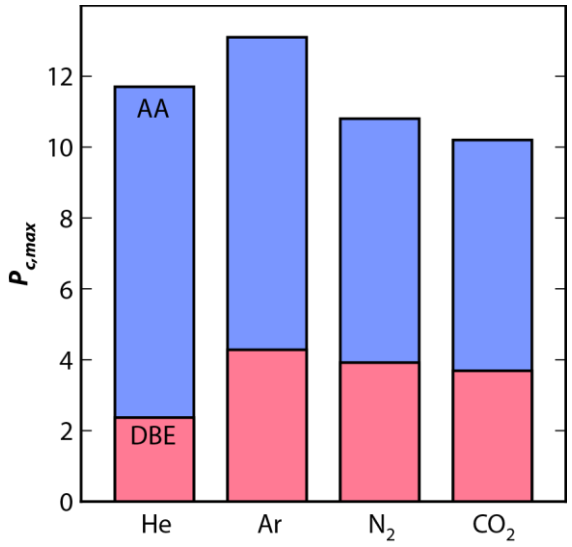

Figure S5.2. Maximum P_c ($P_{c,max}$) as a function of drift gas for amino acids (AA, *blue*)[6] and analogues of Q7 (DBE, *red*). $P_{c,max}$ was determined using a previously derived equation,[6] experimental Ω for the least and most mobile ions, optimal drift voltages (Figure S5.3), and parameters for a high-performance drift tube (Table S5.6).[3]

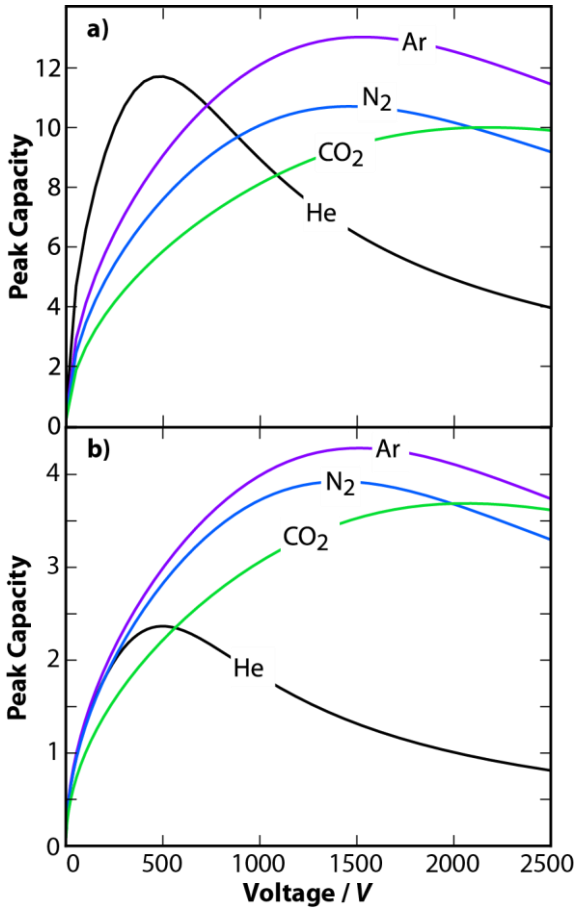

Figure S5.3. P_c as a function of drift voltage and gas using experimental Ω for the least and most mobile ions among a set of (a) amino acids and (b) analogues of Q7 (Figure 5.1). P_c values were determined using a previously derived equation,[6] and parameters for a high-performance drift tube (Table S5.6).[3]

References

(1) Beegle, L. W.; Kanik, I.; Matz, L.; Hill, H. H., Jr. *Int. J. Mass Spectrom.* **2002**, *216*, 257–268.
(2) Allen, S. J.; Giles, K.; Gilbert, T.; Bush, M. F. *Analyst* **2016**, *141* (3), 884–891.
(3) Ibrahim, Y. M.; Baker, E. S.; Danielson, W. F.; Norheim, R. V.; Prior, D. C.; Anderson, G. A.; Belov, M. E.; Smith, R. D. *Int. J. Mass Spectrom.* **2015**, *377*, 655–662.
(4) Mesleh, M. F.; Hunter, J. M.; Shvartsburg, A. A.; Schatz, G. C.; Jarrold, M. F. *J. Phys. Chem.* **1996**, *100* (40), 16082–16086.
(5) von Helden, G.; Hsu, M. T.; Gotts, N.; Bowers, M. T. *J. Phys. Chem.* **1993**, *97* (31), 8182–8192.
(6) Davidson, K. L.; Bush, M. F. *Anal. Chem.* **2017**, *89* (3), 2017–2023.